공학박사 학위논문

Fabrication of inherently helical silver nanofiber using electrospinning process

전기방사 공정을 통한 헬리컬 구조의 은나노 섬유의 제조

2020 년 8 월

서울대학교 대학원

재료공학부

윤 지 현

Fabrication of inherently helical silver nanofiber using electrospinning process

Advisor: Woong-Ryeol Yu

by

Jihyun Yoon

2020

Department of Materials Science and Engineering Graduated School Seoul National University

Fabrication of inherently helical silver nanofiber using electrospinning process

전기방사 공정을 통한 헬리컬 구조의 은나노섬유의 제조

지도 교수 유 웅 열

이 논문을 공학박사 학위논문으로 제출함

2020 년 6 월

서울대학교 대학원

재료공학부

윤 지 현

윤지현의 공학박사 학위논문을 인준함

2020 년 6 월

위 원 장 안 철 희 (인)

부 위 원 장 유 웅 열 (인)

위 원 이 명 규 (인)

위 원 조 대 환 (인)

위 원 이 병 선 (인)

Abstract

This study aimed to fabricate silver nanofibers using new process parameters of electrospinning and develop transparent and stretchable electrodes for stretchable electronics using them. A series of research was carried out to achieve goals as follows.

A multi-physics model for the simulation of gas-assisted melt-electrospinning (GAME) process was developed to understand the roles of process parameters. By numerically calculating the stresses acting on the jet during a single-nozzle GAME process, the shear viscous stress was identified as the main factor of jet stretch. The jet stretch ratio increased sharply when shear viscous stress reached the level at which jet sharpening occurred, leading to stable jet formation. This stress was defined as the critical shear viscous stress to determine stable spinnability. In addition, a multi-nozzle GAME was simulated, proposing a spinnability diagram for stable spinning.

A new process was designed to fabricate helical fibers. Here, the effect of solidification behavior of the jet on the formation of intrinsic curvature and on the final morphology of electrospun fibers was investigated. Fiber morphology during electrospinning was observed to dramatically change from straight to helical due to rapid solidification of the jet. Investigation of the resulting jet morphologies revealed that fiber structure changed from straight to helical as the vapor pressure increased. A similar effect was observed with conductive solutions prepared by adding large

amounts of metal ion to the polymer solution. Simulations revealed that the jet near the nozzle tip was subject to a strong electrical field due to increased charge density. The thickness of the emerging fiber was rapidly reduced with fast and simultaneous solidification, resulting in helical nanofibers. A mechanism was suggested that can describe the formation of helical fibers.

Transparent and stretchable electrodes (TSEs) was fabricated using electrospun silver nanofibers. Here, a composite comprising shape memory polymer–TSE (SMP–TSE) using crosslinked polycyclooctene as a substrate was fabricated, which showed wrinkle-free deformation and switchable optical transparency. Because of its considerable elongation without residual strain and the shape memory behavior of polycyclooctene, in-plane buckled nanofibers were formed effectively. Due to these in-plane buckled nanofibers, the electrode maintained its resistance during 3,000 cycles of a bending test and 900 cycles of a tensile test. Furthermore, SMP–TSE was able to electrically control its temperature, optical transparency, elastic modulus, and shape memory behavior. Finally, SMP–TSE was demonstrated for a smart electrode that could control its optical and mechanical properties.

Keywords: Electrospinning, Numerical simulation, Process parameters, Silver nanofibers, Transparent and stretchable electrode

Student number: 2014-22539

Contents

List of figures

polycyclooctene (PCO) at room temperature, and crosslinked PCO above its transition temperature (80°C). The breaking strains were 195% (PDMS), 280% (crosslinked PCO, room temperature), and 550% (crosslinked PCO, 80°C).

Figure A-3 Illustration of the fiber morphologies according to solidification position of electrospun jet.

List of tables

Chapter 1. Introduction

1.1. Electrospinning

1.1.1. Introduction of electrospinning

Electrospinning has been used as a simple and efficient process to manufacture nanofibers from various polymers since its development in the early 20th century.[1] This process has numerous advantages over other fiber manufacturing processes, which include cost-effectiveness, simplicity, efficiency and ease of control of the fiber structure and diameter (nm to μm).[2] Interest in nanomaterials in various fields has increased since the 1990s, and electrospinning processes have developed as a consequence.[3] There are many reports related to improvements in the spinning process parameters.[4-9]

Nano or sub-micro fibers with various internal structures have been introduced due to development of electrospinning techniques and theoretical studies about process parameters. Pore size, pore distribution, surface area, and arrangement of material can be controlled for proper applications such as biomedical, electrochemical and environmental applications. However, the macroscopic structure of those fibers has remained straight, which has little resistance to mechanical deformation. Therefore, fabrication of inherently deformable structure, such as wavy, buckled, and helical fibers is demanded to advanced applications. To fabricate flexible, foldable and stretchable nanofibers, the basic principle, techniques and process parameters of electrospinning were reviewed. In this section, newly emerging parameters for

electrospinning were searched to control the structure of the electrospun fibers. Over the last decade, parameters such as electric field distribution, nozzle geometry, vapor pressure of the solvent and electrical properties of solution have been figured out as important factors that determine electrospinnability and fiber structure. Roles of those parameters were investigated through this thesis.

Most electrospinning processes use needles (nozzles) as spinnerets and monocharged electrodes from a power supply. Once a voltage is applied to the needle, electric charges accumulate on the free surface of the solution inside the needle. Electrical repulsion occurs once the solution reaches the same polarity charge. When the electrical repulsive force exceeds the surface tension of the droplet formed on the needle tip, a Taylor cone forms, and the jet is ejected. The entanglements among polymer chains can maintain continuity of the ejected jet and fiber. Once ejected, the fiber then passes through the straight jet and whipping cone stages where bending instability occurs. The jet stretches due to Coulombic forces with simultaneous evaporation of the solvent until it reaches the grounded collector. The collected solidified fibers can form as a non-woven fabric because of the whipping phenomena.[10] A schematic description of electrospinning is provided in **Figure 1-1**.

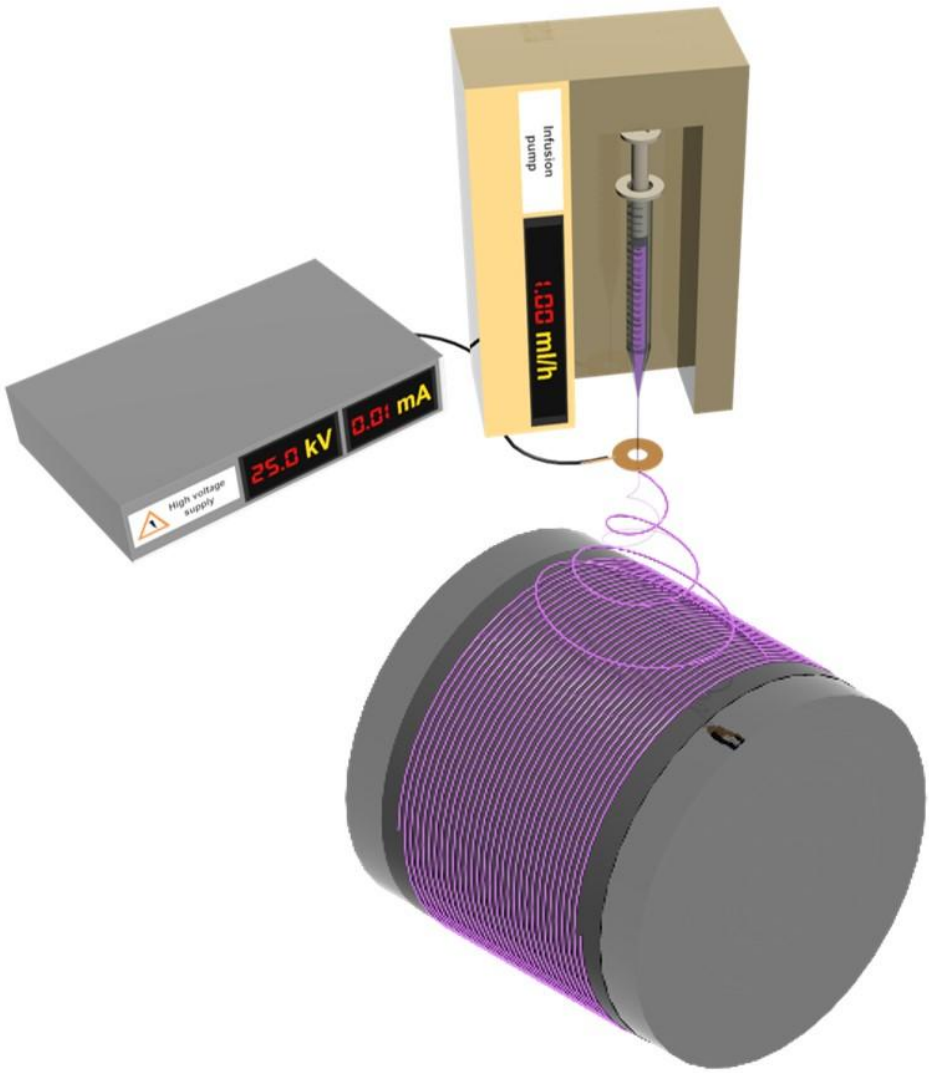

Figure 1-1 Schematic diagram of the electrospinning process.

1.1.2. Types of electrospinning

There are various types of electrospinning process. Those can be classified according to state of liquid (solution, polymer melt, immersion) and arrangement of

apparatus (coaxial, side-by-side, and multi-axial).

Solution and melt electrospinning

Both processes use liquid state, but solution electrospinning uses polymer solution and melt electrospinning uses polymer melt. There are entanglements between the dissolved or melt polymer chains which increases the viscosity of liquid resulting maintaining their fibrous structure during spinning. In solution electrospinning, number of the entanglements are determined by the concentration of polymer.[11, 12] Certain degree of entanglement is required for stable electrospinning, if the number is small, electrospraying occurs on the other hand, if the number is large, beads or clogging occurs.[13] Also, the electrical characteristics of both processes are quite different. Solvent in polymer solution generally has much higher electrical conductivity than that of dissolved polymer or polymer melt.[14] Therefore, the electrical stress developed during process in solution electrospinning is much larger, resulting great reduction of fiber diameters. Furthermore, due to quenching and solidification of polymer melt due to cooling, the fiber diameter of melt electrospinning is in micrometer scale. When the jet is solidified, the charges at the surface of inside jet are also trapped for melt electrospinning. On the other hand, in solution electrospinning process, due to remaining solvent the charges remained in electrospun fibers. Those are called residual charges.[15] Because of the differences in mechanism and final products between two techniques the applications of the electrospun fibers are also different. Even though the diameter of the melt electrospun fibers are much thicker, the productivity is much larger than solution

electrospinning due to lack of solvent. Also, there is no need to remove the residual toxic solvent, melt electrospinning has been widely used in biomedical applications. [16]

Coaxial and multi-layered electrospinning

The coaxial electrospinning process, first introduced in 2002,[17] enabled the fabrication of nanofibers with more diverse morphologies and applications from two or more types of polymer solutions.[18, 19] Importantly, non-polymeric materials without filament-forming properties (such as ceramics, metal oxides and semiconducting materials) can be processed into nanofibers with electrospun core–shell nanofibers as templates; however, using a second polymeric liquid greatly increased the complexity of the process because of the greater number of parameters to be controlled, which included those related to interfacial properties such as miscibility and compatibility, and shell-to-core fluid flow rate and their ratios. Nevertheless, achieving control of the interfacial behavior between two adjacent polymeric liquids has enabled modifications of coaxial electrospinning systems to provide increased number of layers (e.g., triple [20, 21] or quadruple layers [22]) or multi-channeled structures.[23] As the selection of materials has become more diverse and various structures have been fabricated, coaxial electrospinning applications have expanded to the biomedical (antibacterial, drug delivery), [24-26] electrochemical (batteries, supercapacitors, energy harvesting)[27-29] and environmental (oil filters, molecular filters) fields.[30] Thus, it is important to identify those process parameters that will enable the realization of specific and

useful one-dimensional (1D) nanostructures for various applications.

1.1.3. Parameters in electrospinning

Electrospinning is governed by various groups of parameters, i.e., process, solution and environmental parameters. Process parameters include the applied voltage, tip-to-collector distance (TCD), collector rotational speed and type of collector.[2] Solution parameters include viscosity, surface tension, concentration, conductivity and the dielectric constants of the solvent and polymer. Additionally, environmental parameters, which are not readily controlled, include humidity and temperature.[31] The collection of electrospinning process parameters affects the surface tension, viscous stress and electrostatic forces; the morphologies of the nanofibers are governed by the interactions of these forces. Several reviews have discussed polymer/solvent/processing condition relationships and their impact on the produced electrospun fibers.[6, 7, 19] In this section, those parameters that lead to successful electrospinning were described.

Unlike the conventional electrospinning, compatibility of the solutions is very important in coaxial or multiaxial electrospinning. The solutions should be immiscible or semi-miscible to form a stable Taylor cone at the nozzle tip. If the solutions are incompatible, precipitation, solidification and mixing of solutions occur when they are in contact. The presence of a core–shell interface and a liquid–gas interface are distinctive features of coaxial electrospinning. A shear force consisting of viscous dragging and contact friction is generated at the interface of the

core and shell solutions during the process.[32] Stable core–shell fibers can be obtained when the shear stress due to the viscosity of the shell solution overcomes the interfacial surface tension between the core and shell solutions. Thus, in the traditional coaxial processes, the viscosity of the shell solution should be higher than that of the core solution. Additionally, the flow rate of the shell needs to be higher to entrain the core solution completely.[33, 34]

The viscous shear stress of the shell solution enables the core solution to be entrained in the compound jet. Thus, the core solution need not be electrospinnable. However, if the shell solution is unelectrospinnable and the inner solution is electrospinnable, the inner solution can also drive electrospinning. The driving solution should have sufficient electrical conductivity to provide enough Coulombic repulsion during jet stretching. It should also have sufficient viscosity, which stems from the entanglement of polymer chains, so that it maintains continuity of the jet and fiber. Although experimental and theoretical studies have improved our understanding of the process and parameters, the concrete mechanisms of compound jet formation and propagation in coaxial electrospinning remain unknown.

The single-fluid electrospinning process can be described by jet instability theory. In particular, 1D and three-dimensional (3D) modeling have been carried out by Reneker *et al*.[35] Rayleigh instability, which is determined by the surface tension, is a factor related to both the shape of the jet and the uniformity of the fiber structure.[36] Instability theory can describe coaxial electrospinning phenomena because coaxial and single-fluid electrospinning processes use similar process

parameters and fiber formation mechanisms. Many theoretical and experimental studies on the effects of coaxial electrospinning process parameters have been based on single-fluid electrospinning research.[37-40] The following sections describe the process parameters that have emerged over the past decade of research especially on coaxial electrospinning.

Nozzle geometry and electrical field distribution

Generally, the fluid is ejected through nozzle in electrospinning. Therefore, the size and length of the orifice determined the diameter of the electrospun fibers.[41] However, Zhou et al., introduced flat spinneret that replaced single-needle electrospinning.[42] They found that spinnability window was similar with single-needle system. However, when increase the number of spinnerets, the spinnability of the needleless cases were much larger resulting higher productivity.[43-45]

The shape of the electrospinning nozzle is important because of the need to control the flow rate, miscibility, and compatibility of the solutions. The morphologies of the electrospun fibers depend on the diameters of the nozzles (inner/outer nozzle diameter ratio) and their geometry (length of the core nozzle, separation distance between the core and shell nozzles). [46-48]

Traditionally, coaxial electrospinning processes have used concentric cylindrical nozzles with appropriate inner and outer nozzle diameters. However, it is difficult to form multilayered structures simply by using the conventional method of controlling the nozzle diameter ratio. Lee *et al.*[47] introduced a core-cut nozzle in which the exit of the core nozzle was removed. Using the core-cut nozzles, they fabricated two-,

three- and four-layered (tube-in-tube) carbon nanofibers, and they analyzed the jet instability reduction effects of the new core-cut nozzle configuration using the finite-element method (FEM). According to the FEM analysis, as the exit end of the core nozzle becomes shorter, thinning of the core solution occurs earlier and formation of the envelope is delayed. Additionally, the surface charges become more concentrated at the nozzle tip, facilitating electrospinning. Moreover, the core-cut nozzle prevents polarization of the core solution compared with the general nozzle geometry, thereby reducing unnecessary electric forces applied to the interface. This results in reduced jet instability.

Another study explored changing the geometry of the inner nozzle. Rahimi *et al.*[46] changed the protrusion height of the inner nozzle tip from the shell nozzle. The protrusion height was varied from a slightly protruded shape to an indented shape. They used hexadecane (HD), which is a non-conductive low-viscosity material, as the core solution and polyurethane (PU) as the shell solution. Because most studies concerning nozzle geometry have focused on conductive solutions, this study was valuable in expanding material selection. The group showed that when the core solution had low viscosity and was non-conducting, protrusion of the nozzle was beneficial for manufacturing core–shell nanofibers, while others reported that stable coaxial electrospinning of a conducting polymer was possible with a core-cut nozzle.[47] There was an optimal length of the protrusion that enabled stable fabrication of the core–shell structure. As the height of the protrusion increased, the reduced stability of the Taylor cone resulted in solution mixing. The appropriate geometry of the nozzle when using conducting solutions has been studied both

experimentally and theoretically.[49, 50] These studies indicated that the protrusion of the core nozzle should be tens-of-percent of the diameter of the shell nozzle due to higher viscous entrainment. Moreover, in sufficiently strong electric fields, the optimal protrusion length for stable manufacture of a core–shell structure was identified as half the radius of the outer nozzle.[50] Kaerkitcha *et al.* fabricated hollow carbon nanofibers using core–shell nozzles of different geometries, e.g., indented (inward), normal and protruded (outward). The results showed the effects of the nozzle geometry on the pore size, fiber diameter, wall thickness and conductivity. Nozzle geometry has become a crucial process parameter.[51]

The effect of the nozzle diameter on the morphology of core–shell structures has been investigated.[52]Changing the nozzle diameter affected the electric field distribution. The electric field envelope increased with increasing diameter of both nozzles (core and shell) and increased the jet-whipping angle. The increased whipping angle enabled stable production of helical core–shell nanofibers. Smaller-diameter core and shell needles resulted in fibers with unclear solution boundaries. The effect of the position of the core nozzle on the core–shell structure has also been studied. Wu *et al.*[53] conducted numerical and experimental studies into the effect of changing the position of the core nozzle in three situations: eccentric, coaxial and side-by-side. In the eccentric case, an asymmetric electric field was generated, while the side-by-side case gave the lowest electric field.[53]

The asymmetric electric field generated by the eccentric nozzle enhanced interactions (viscous dragging) at the core–shell interface, thereby promoting

formation of a helical nanofiber. Especially in jets stretched by an electric field, molecular interactions such as hydrogen bonding enhance viscous dragging and thus promote the formation of helical nanofibers. These factors, i.e., control of nozzle geometry, nozzle alignment and changes in the electric field distribution, have also become essential for successful electrospinning.

Viscosity ratio of the solutions

The importance of the viscosity of solutions in coaxial electrospinning was noted in the previous section. Because the viscosity, η, of a polymer solution is generally determined by polymer chain entanglement, it increases with increasing concentration, C. The viscosity can be predicted as follows: $\eta \approx C^{1.25}$ and $\eta \approx C^{4.25\text{-}4.5}$ for semi-dilute, untangled and entangled regimes, respectively.[11-13] In addition to the relative molar mass and the polymer chain shape, the solvent power also affects the viscosity of a polymer solution. In general, polymer solutions can be electrospun when the concentration exceeds the entanglement concentration, C_e. [13]

In coaxial electrospinning, each of the solutions must fulfill the viscosity criterion, but also satisfy the viscosity ratio (η_{core}/η_{shell}) threshold.[12] Tiwari *et al.* investigated the effect of the viscosity ratio on electrospinnability. When η_{core}/η_{shell} exceeded 1.7, coaxial electrospinning was unsuccessful due to rapid drying of the shell solution. Additionally, when η_{core}/η_{shell} was less than 0.55, the core solution frequently broke, even though both solutions satisfied the viscosity criterion, because the viscous drag of the shell solution was insufficient, or too much, to stretch the core solution continuously. Kaerkitcha *et al.*[54] also studied the viscosity ratio in

coaxial electrospinning. They found that the viscosity ratio affected not only the formation of a stable Taylor cone and the electrospinnability but also the morphology of the electrospun fibers, e.g., the wall thickness increased with an increasing viscosity ratio. As increasing the viscosity ratio, the core diameter decreased because the amount of the core material flow decreased, and the wall thickness increased because the elongation by the electrostatic repulsion was harder for high viscous shell. The total diameter also increased with increasing the viscosity ratio. For the same viscosity ratio but different absolute viscosity, the total diameter can be changed, maintaining the same morphologies. Moreover, twisted cores were observed at lower viscosity ratios because the viscosity of the shell solution was insufficient to stabilize the core–shell morphology. Hence, the authors suggested that the viscosity ratios should be in the range of 1.22–2.82. The viscosity ratio has become an important factor in the coaxial electrospinning process for controlling fiber morphology.

Evaporation rate of the solvent

Evaporation of the solvent affects the formation of a stable Taylor cone and jet propagation and elongation. If the evaporation rate is too high, the solution dries at the end of the nozzle tip before forming a Taylor cone, whereas large drops or wet fibers are observed due to an excess amount of solvent when there is too little evaporation. When the evaporation rate of the shell solution is much higher than that of the core solution, the core solution (and the skin layer formed by the shell solution)

cannot withstand the atmospheric pressure, resulting in buckling and fiber collapse. A high evaporation rate of the core solution can also result in buckling and a collapsed fiber shape due to the pressure difference between the voids in the core and the atmosphere.[55, 56]

Considering the effect of the solvent evaporation rate on the coaxial electrospinning, a new process was developed, e.g., pure solvent was used as the shell material while polymer solution was provided into core.[57] Shell solvent with low evaporation rate produced nanofibers with higher quality (surface smoothness, structural uniformity, uniform distribution of the electrospun fibers) than that of nanofibers produced from the same polymer by single-fluid electrospinning because the evaporation of the core solvent was retarded by the shell solvent.[58] Due to the slow evaporation of the core solvent, the solution went through more electrical drawing over a longer period in the instability region, resulting in thinner nanofibers. Various solvents such as *N,N*-dimethylformamide (DMF),[59] mixtures of acetone, *N,N*-dimethylacetamide (DMAc) and ethanol,[60] stearic acid (SA) in chloroform solution[61] and zein in aqueous ethanol solution [62] in the shell were used for this purpose. On the other hand, other additives such as surfactants,[63] sodium thiocyanate salt,[63] LiCl[64] and silver nitrate [65] were added to the shell solution. The surfactants in the shell affected the dynamic evaporation rate of the core solvent, causing the core fluid to have longer exposure to the electrical drawing process.

Evaporative cooling can occur when a volatile solvent evaporates. As the system temperature drops below its upper critical solution temperature, the solvent-rich and solvent-poor phases can separate, resulting in the formation of pores.[66, 67] Hence,

the evaporation rate of solutions has become an important factor for controlling the morphology, quality and electrospinnability of nanofibers.

Electrical properties of solutions

The electrical properties of solutions affect the instability of the coaxial jet because instability results from disturbed surface charges or an electric field. In particular, different electrical properties of core and shell solution, e.g., both are conductive (or dielectric) or only one of them is conductive, determine the final shape of coaxially electrospun fibers because equipotential (or non-equipotential) interface constrain the movement of all free charge.[68] The electrical properties of core and shell solutions are indispensable to core–shell jet and core–shell nanofiber instability research. However, it is difficult to study the instability according to the electrical properties via experimental approaches, and so theoretical approaches have typically been used.[39] These are valuable for understanding the underlying mechanism and predicting results for unusual material combinations.[31]

Li *et al*. conducted a theoretical study to investigate the effects of the electrical properties of coaxial fluids on jet instability.[40] The axial electric field was assumed to be uniform. The combinations of fluids were as follows: 1) inner: dielectric, outer: conductor; 2) inner: conductor, outer: dielectric; 3) inner: conductor, outer: conductor; 4) inner: dielectric, outer: dielectric. When only one of them was conductive, para-varicose (cosine shape) and para-sinuous (sine shape) modes were observed in nanofiber shape, respectively.[68, 69] For the non-equipotential case, the dielectric constant of the shell liquid (driving solution) had a greater effect on jet

instability than the permittivity and conductivity of the core liquid. In contrast, when both were conductive (or dielectric), the transitional mode was amplified by the axial electric field because the axial electric field strongly influenced the outer surface of the conducting solution.[68] It was suggested that the equipotential case was more advantageous to the core-driving case than the non-equipotential case. On the other hand, a moderate electric field was recommended for the generation of a coaxial jet. Reznik *et al.*[50] experimentally validated these theoretical findings. Although low-conductivity solutions were used, the shell acted as the driving medium due to the rapid migration of free charges from both solutions and the interface to the outer surface of the shell. Lastly, when the shell and the core were treated as a leaky dielectric and a dielectric, respectively, the axial electric field and the surface charge had significant effects on the stabilizing and destabilizing modes, respectively.[38, 70]

Instability analysis was investigated to determine the effect of a radial electric field as a function of the driving medium in coaxial jets.[70] Generally, the axial electric field stabilizes, whereas the radial one destabilizes a jet.[69] Considering the perturbation of electric stress due to the radial electric field in both equipotential and non-equipotential cases, the radial electric field destabilized the para-varicose mode for the shell-driving case and stabilized it in the core-driving case. When the intensity of radial electric field became sufficiently strong, the non-axisymmetric modes were activated, leading stable electrospinning, and those modes grew faster in the equipotential case.

It has been established that coaxial electrospinning requires a shell solution with high or intermediate conductivity. The theoretical and experimental results indicate that the conductivity of solutions can be controlled by adding salts, without critically affecting their physical properties. This greatly expands the choice of materials for coaxial electrospinning.

1.1.4. Structures of electrospun nanofibers

The materials for solid nanofibers are consist of elastomer,[71] phase change polymer,[72] conductive polymer,[73] and precursor of carbon nanofibers.[73, 74] Those nanofibers had higher strength and rigidity due to size effect, and the diameter of some electrospun nanofibers can be reduced under 20nm.[75, 76]

Not only for the solid fibers the surface area and their distribution can be controlled. Porous nanofibers having macro, meso and nanopores can be fabricated.[77] Surface area to volume ratio can be further enhanced due to the pores in nanofibers. By controlling those distribution and size of pores the nanofibers have been applied to drug delivery that control burst or sustain release of the drugs,[78] and energy storage device such as lithium battery and lithium-sulfur battery.[79, 80]

One of the advantages of the electrospinning process versus other fiber fabrication processes is the facile control of the structure of nanofibers, which can be not only straight nanofibers but hollow,[55, 66, 81-89] fiber-in-tube,[90] tube-in-tube[90, 91] and multichanneled.[22, 23] These various nanostructures are important in

nanoscience and have been developed for various nanoscience applications.[92]

Hollow fibers

Hollow fibers have the advantages of large surface-to-volume ratios and the ability to isolate materials placed within them.[93, 94] Coaxial electrospinning is one of the simplest methods to rapidly fabricate high-aspect-ratio hollow micro/nanofibers. The diameters of the fabricated hollow fibers can be up to several microns and the shell thickness can be controlled from several tens-of-nanometers to several microns.[95, 96]

Generally, coaxially electrospun hollow fibers can be obtained after electrospinning in one of two ways, i.e., by core extraction[88] and by core decomposition.[97] The former approach uses solvents to selectively dissolve only the core materials, preserving the shell part.[88] The decomposition method uses heat to remove the core material. Each of these methods has advantages and disadvantages. The core extraction method is simple, but the core and shell polymers are limited by the choice of solvents. During extraction, the shell must withstand the capillary forces, which requires a rigid wall.[32, 98] Decomposing the core materials by a sequential heat treatment after fabricating the core–shell fibers can also limit the choice of polymers.[99] For this method, the shell material should maintain its structural stability during the decomposition of the core because pressure drops in the core capillary can cause shell collapse.[55] The decomposition method has been used to control the internal structure of hollow carbon nanofibers with high reproducibility

in terms of uniformity of pore size and shell thickness. In some cases, liquids such as ethanol and mineral oil are used as the core material, which can be eliminated by evaporation and heat decomposition, respectively.[88, 97] **Table 1-1** details the polymers, solvents, features of the fabricated hollow fibers and possible applications of the different types of hollow fibers.

Table 1-1 The polymers, solvents, features of the fabricated hollow fibers and possible applications of the different types of hollow fibers.

Method /approach	Materials core/shell	Solvents core/shell	Features	Application	Core removal	Ref.
Protrusion core nozzle	HD /PU	DMF/ DMF,THF	Expanding the range of electrospinnable solutions	Protective clothing	Extraction (hexane)	[46]
Using less volatile solvent	PVP /PVDF-HFP	H_2O, ethanol /THF,DMF	Alleviating the buckling of the structure		Extraction (water)	[55]
Coaxial electrospinning	PLLA /PEG	DCM,DMF /H_2O	Aligned and tightly packed hollow fiber arrays	Nerve tissue, vascular structure	Extraction (water)	[100]
New material composition	SAN /PAN	DMF /DMF	Preventing shell shrinking due to stainability of core material		Decomposition	[82]
Challenging material	PEO/chitosan	Aqueous acetic acid/aqueous acetic acid	Cationic and high molecular weight biopolymer chitosan as shell	Biomedical, wound dressing	Extraction (water)	[84]
In situ encapsulation	Glycerol /PU	H_2O /DMAc	Enhancing reaction rate and efficiency of bi-enzyme system	Bi-enzyme system	Evaporation	[101]
Highly aligned membranes	PEO /PC	H_2O /THF	Membrane with high alignment (97%)	Vascular scaffolds, biomedical devices	Extraction (water)	[87]

Triaxial electrospinning	Ethanol /lignin /glycerin	Ethanol /ethanol /ethanol	Stable formation of hollow nanofibers	Hollow carbon fiber	Decomposition	[97]
Colloid template	Mineral oil /PVP, PS colloids	Mineral oil/H_2O	Electrospun macroporous semiconductor metal oxide nanostructures	Hydrogen sensing	Decomposition	[102]

Tetrahydrofuran (THF), poly(vinylidenefluoride-co-hexafluoropropylene) (PVDF-HFP), poly(L-lactic acid) (PLLA), poly(ethylene glycol) (PEG), dichloromethane (DCM), styrene-co-acrylonitrile (SAN), poly(acrylonitrile) (PAN), poly(ethylene oxide) (PEO), polycarbonate (PC), polystyrene (PS)

Hollow nanofibers can also impart outstanding properties related to adsorption, reactivity and transportation. These are some reasons for the broad applications of hollow structures.[50, 103] Their potential can be increased by functionalization and surface modification of either the inner or the outer surface of the wall. For functionalizing the inner surface of the shell, there are three options.[90, 102] By simply adding functional materials in the core, the functional materials stick to the inner surface as the core binding materials are decomposed or washed away.[47] In contrast, by adding functional materials in the shell, both inner and outer surfaces of the shell can be functionalized by taking advantage of their phase separation and diffusion.[90] Additionally, hollow nanofibers can be functionalized by encapsulating different kinds of functional materials (e.g., active materials, enzymes) in the inner and outer walls simultaneously.[90] It should be cautious that the viscosity and conductivity of solutions can also be changed by adding functional materials, altering the interaction of the core and shell solutions at their interface. For example, hydrogen bonding or ionic exchange interactions formed by functional materials can lead to unwanted surface pores.[104] This kind of side-effect can be

mitigated by careful choice of the concentration of the functional materials. These functionalized hollow micro/nanofibers have a wide variety of applications; these will be discussed in **1.1.5**.

Porosity can be imparted to hollow fibers. The immiscibility and phase separation of two solutions provided porous hollow fibers.[89] Kurban *et al*. reported that semi-miscible core–shell solutions increased the surface porosity of the fibers.[31] Images of highly porous hollow fibers are shown in **Figure 1-2**.

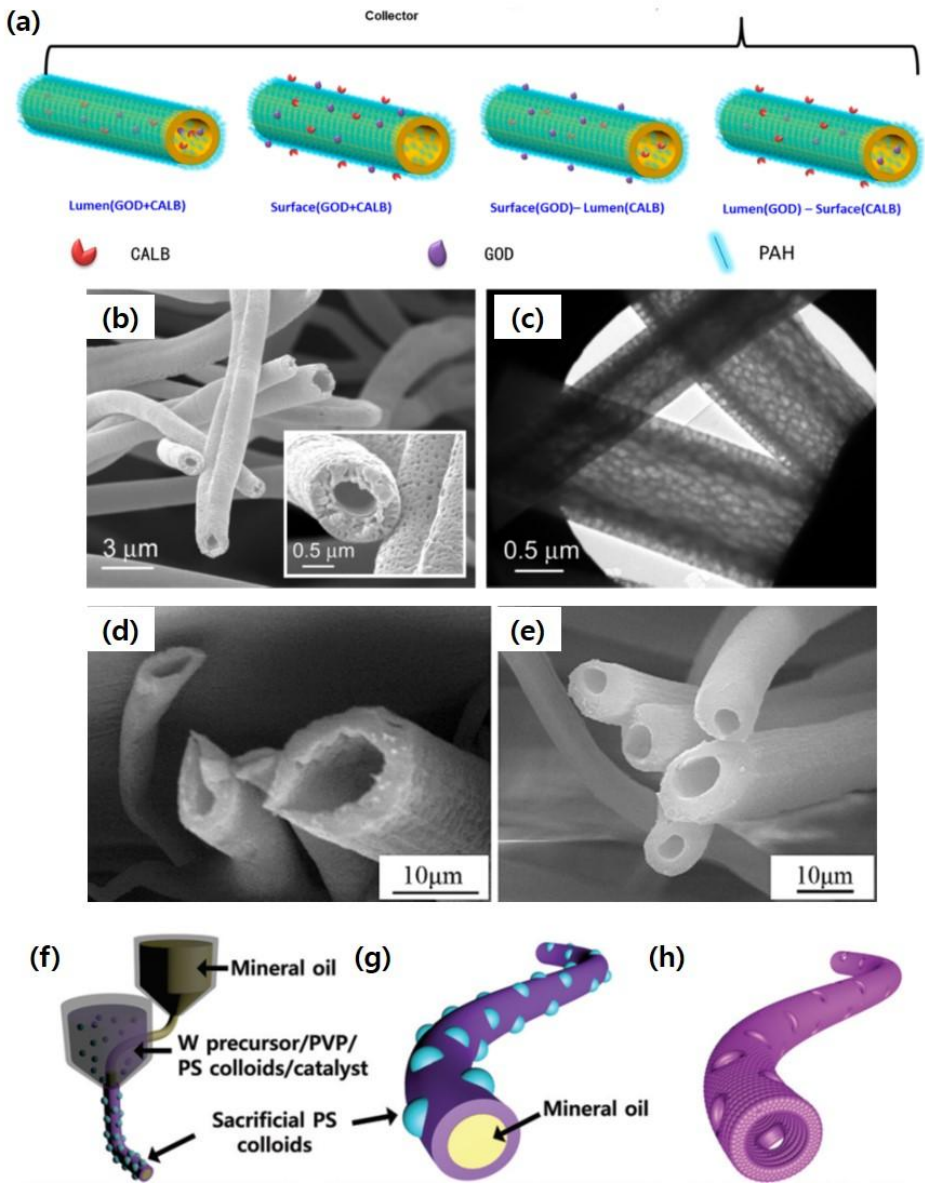

Figure 1-2 (a) Possible combination of functionalization of the inner/outer surface of hollow fibers.[86] Reproduced with permission. Copyright 2014, American Chemical Society. (b) Scanning electron microscopy (SEM) image of ammonia borane (AB)-polystyrene (PS) fibers. (c) TEM image of AB-PS fibers.[31] Reproduced with permission. Copyright 2010, American Chemical Society. (d) SEM images of poly(vinylidenefluoride)/poly(vinyl alcohol) (PVDF/PVA) microtubules after soaking in H_2O for 30 min and (e) then in cold H_2O for 2 h.[83] Reproduced

with permission. Copyright 2012, Elsevier. Schematic illustrations of (f) co-axial electrospinning using a mineral oil-composite solution as the core-shell, (g) as-spun tungsten (W) precursor/poly(vinylpyrrolidone) (PVP) composite nanotubes (NTs) decorated with polystyrene colloid templates and apoferritin-encapsulated nanocatalysts, and (h) catalyst-loaded macroporous WO_3 NTs with multiple pores after calcination.[102] Reproduced with permission. Copyright 2016, Royal Society of Chemistry.

When the two solutions made contact at the nozzle tip, the fiber structure transformed via a phase separation mechanism.[105] The formation of solvent-rich and -poor regions affected the fiber morphology because the continuous evaporation of solvent resulted in pores.[66, 67] The formation of pores could be controlled by the solvent evaporation rate.[83] In the core elimination stage, cold water smoothed the fiber surface and reduced fiber fracture (**Figure 1-2** (d–e)). Another method for imparting porosity to hollow fibers is to mix sacrificial materials in the shell solution and then perform coaxial electrospinning. Choi *et al*. made WO_3 nanotubes using mineral oil as the core and a mixture of tungsten (W) precursor, PVP and colloidal polystyrene (PS) particles as the shell, followed by sequential calcination (**Figure 1-2**(f–h)).[102] A wide range of applications were suggested from this research because of the ability to tailor the pore size, utilize functionalization and control the core diameter of the nanofibers.

Core–shell fibers

Coaxial electrospinning has been used to create a wide range of core–shell nanofiber morphologies. Core–shell fibers have been widely studied because of their

ability to isolate and release substances, and to enhance mechanical properties.[106] The formed structures include simple core–shell nanofibers,[84] hierarchically-branched and dumbbell-shaped nanofibers, [107] fibers with beads,[107] and spring-like structures.[108] Interestingly, core–shell nanofibers with stacked toroid and helical morphologies were fabricated using their selected block copolymer due to its self-assembly properties.[109, 110] Monte Carlo simulations predicted that confined core materials could form stacked toroids or helices, suggesting further sophisticated structure can be developed using simulation.[111, 112]

Functionalization of the core–shell fiber by embedding or coating with functional substances and the modification of surfaces and interfaces has led to a wide range of applications.[113] Much core–shell fiber research has focused on functionalization;[114-116] Embedding ceramic, metallic, metal oxides and carbon materials into fibers has been investigated for electrochemical applications.[90, 95, 116] Other studies have focused on controlling the porosity of the shell and core–shell interfaces. Using the immiscibility of two kinds of solutions enabled the pores to be distributed radially and longitudinally throughout the fibers. A highly conducting core and a sufficiently low surface tension between the core and shell led to interface instability, which was leveraged to create high porosity in a controlled manner in the fibers.[31] This approach has also been used to tune the microstructures for uniform distribution of drugs and nanoparticles,[117] to provide stimuli-sensitive surfaces for drug delivery [110] and as a form of interfacial engineering for energy materials.[118, 119] These advanced approaches broaden the opportunities for coaxial electrospinning.

Triple/quadruple-layered, multichanneled fibers

Multi-axial electrospinning was developed to fabricate multilayered, multichanneled nanofibers with tailored layers having different properties. The properties of individual layers can be varied from hydrophilic or hydrophobic[91] to electrically conductive or insulating and electrochemically active or inactive.[90, 91] Such modifications can improve biocompatibility, mechanical properties,[120] filament-forming ability and functional properties.[121]

Multilayered, multichanneled structures are highly complex and challenging task. A multi-layered structure such as a fiber-in-tube structure can be manufactured by eliminating the intermediate layer. The intermediate layer can remain as a void[21] or be filled with functional materials.[90] **Figure 1-3** shows examples of fiber-in-tube and tube-in-tube structures. Lee *et al*. fabricated quadruple-layered carbon nanofibers (tube-in-tube) (**Figure 1-3**(e–f)).[22, 23]

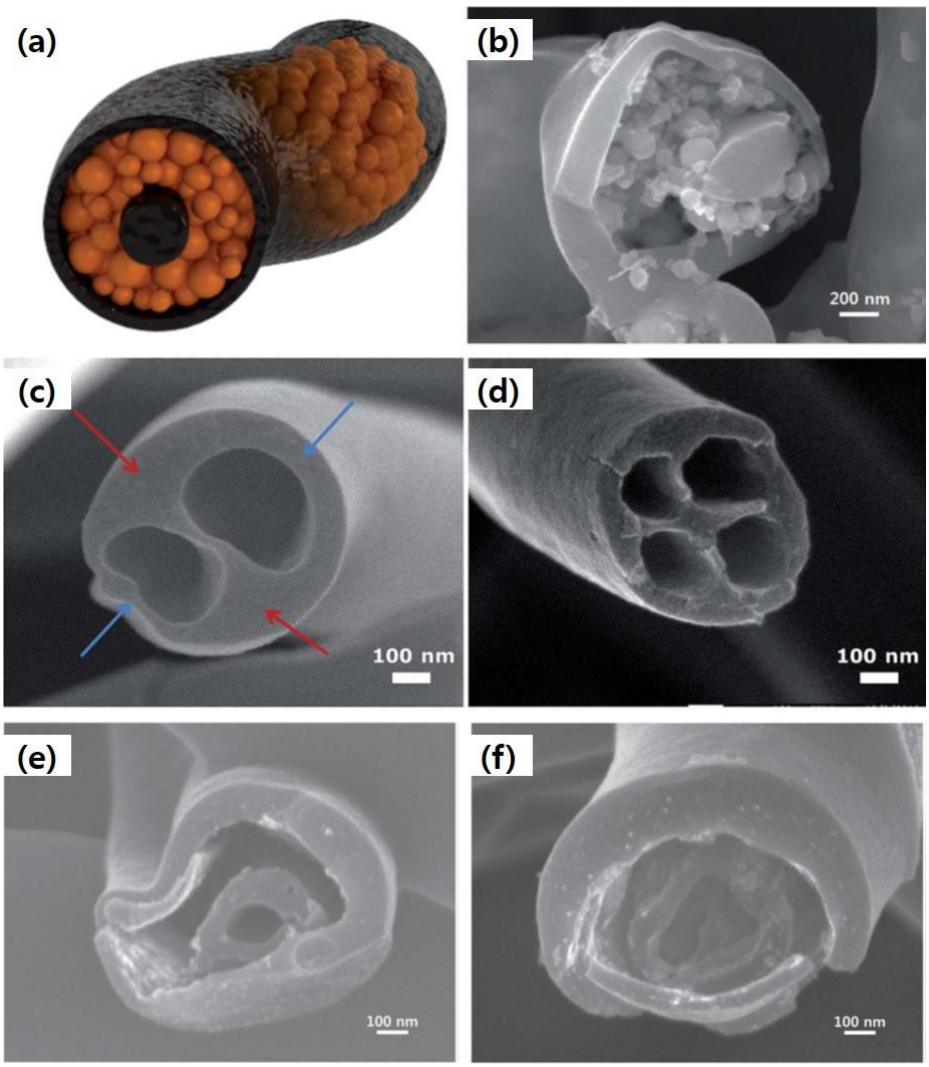

Figure 1-3 Morphology and microstructure of well-prepared trilayered carbon/Si/carbon nanofiber: (a) schematic diagram of the target structure; (b) highly magnified cross-sectional field-emission scanning electron microscopy (FE-SEM) image;[101] Reproduced with permission. Copyright 2014, Royal Society of Chemistry. Morphological characterizations of multi-channeled, hollow carbon nanofibers (HCNFs). FE-SEM images of (c) a two-channel HCNF and (d) a four-channel HCNF at high and low resolution.[122] Reproduced with permission. Copyright 2014, Royal Society of Chemistry. FE-SEM images of alumina nanoparticles incorporated into double-tubular CNFs. (e) and (f) Arbitrarily selected images of nanofibers manufactured under identical electrospinning conditions.[22] Reproduced with permission. Copyright 2014, IOP Publishing.

Multichanneled structure can be fabricated by eliminating only multicores introduced in nanofibers. Zhao *et al.* made two to five channeled nanofibers, while Yang *et al.* synthesized two and four channeled nanofibers via multiple-fluid electrospinning, whose channels were filled with functional materials.[23, 123] The range of potential applications of these fibers could be markedly expanded if diverse active and functional materials could be sectionalized within each layer or channel of the nanofiber.

The few research groups studying multilayered, multichanneled nanofiber manufacturing are using various material combinations with the aim of developing integrated devices having individual functional parts. For example, an active material layer, current collector, conducting path and electrode could be manufactured by multiple-fluid electrospinning. This kind of research is in its early stages and one-step fabrication of these devices should be possible in the future based on the combined use of coaxial, side-by-side and other electrospinning processes. [124]

1.1.5. Application of electrospun nanofibers

Electrospun nanofibers have been engineered with specific compositions for advanced applications.[125] Carbon nanofibers can be derived through heat treatment from carbon precursor fibers. It mainly consists of stabilization and carbonization step. The nanofibers are stabilized in air around 300^{o}C and carbonized at 400^{o}C-1800^{o}C at inert atmosphere.[126] The typical precursor for carbon nanofiber is polyacrylonitrile (PAN), however also includes polyvinyl alcohol (PVA),

polyvinylpyrrolidone (PVP), cellulose, and polymers including pitch.[125, 127-129] Those have been applied to electrodes for energy storage and harvesting devices. Using the benefit of short diffusion distance,[130] those have been applied to solar cells, rechargeable batteries, and supercapacitors.[131, 132] Also, metallic nanofibers can be derived from reduction of metal oxides. Copper, platinum and silver nanofibers/wires have been fabricated for electronic applications. [133-135]

Due to high surface area to volume ratio and high porosity, electrospun nanofibers can be used for a filtration membrane for environmental applications. Those includes air filtration of PMs and ozone,[136] water filtration which demands high adsorption capacity.[137] Electrospun nanofiber is effective even for PMs small as 300 nm size.[138]

Electrospun biopolymer nanofibers have been most actively used for biomedical applications. Due to the biodegradable and biocompatible characteristics of electrospun nanofibers, large amount of research has been reported. Those includes drug delivery, tissue regeneration, and wound healing.[139-141]

Those are only part of applications for electrospun nanofibers. There has been a large amount of fine reviews about the application of electrospun nanofibers in each fields.[142-146] Recently, for advanced application, co-axial and multi-layered electrospinning techniques have been actively researched.

The flexibility of the coaxial electrospinning process has encouraged advanced research into various fields and applications. Four approaches have mainly been

taken: i) combining the properties of diverse materials, ii) extending the windows of applicability of materials by electrospinning non- or poorly-electrospinnable polymers,[147-150] iii) fabricating desirable structures capable of overcoming specific limitations[102, 151] and iv) a mix of these approaches. As for materials, various polymers and functional materials have been coaxially electrospun and are listed in **Table 1-2** focusing on main properties and applications for the following discussion.

Table 1-2 Properties and applications of coaxially-electrospun nanofibers

Properties	Specific characteristics	Polymers	Functional materials	Applications
Mechanical	Mechanical enhancement	PU,[90] sulfonated polysulfone,[152] poly(NIPAAm-co-NMA)[153] PBS[153]		
	Structural sustainability	PEO,[85, 87] SAN,[82] PVA,[83] PCL[150]	PS colloids[102]	Vascular structure, tissue-engineering scaffold
	Self-healing ability		Self-healing agent[154a)]	Self-healing composite
Surface, interface	Surface, interface modification	PMMA,[89, 105] PVDF[155]		Electrocatalysis
	Hydrophobicity	Teflon® AF[149, 156]	Silica NPs[157]	Li-air battery separator
Electrochemical	Electrochemical enhancement		TiO_2,[147, 158-162] MgO,[158] Si,[90, 116] Pt,[163] Co,[163] Pd,[163] ZnO,[164] In_2O_3,[164, 165] ammonia borane,[31] P3HT:PCBM[150, 166]	Li-ion battery, gas sensing, photocatalysis, organic solar cells

	Electrical conductivity	PAN,[90, 163] PEDOT:PSS,[153]	TiO_2,[159] SnO_2,[165] Au,[165] MWNTs[167]	Gas sensor, Li-ion battery
	Photoluminescence		$Eu(BA)_3phen+Dy(BA)_3phen$[168]	Optics
	Fluorescence		$Tb(BA)_3phen$[169]	Optics
Piezoelectric	Piezoelectricity	PVDF[83]		Mechano-electrical coupling
Dielectric	Dielectric permittivity		$BaTiO_3$[118, 119, 170]	Dielectric capacitors
Magnetic	Super-paramagneticity		Magnetite NPs[110]	
Thermal	Thermostability	Natural silk fibroin, silk sericin[104]		
	Thermochromicity		CVL:BPA[171]	Thermochromism
	Thermoresponsivity	poly(NIPAAm-co-NMA),[153] PEG[171]		Thermal energy storage
Biodegradability or biocompatibility	Biodegradability or biocompatibility	PCL,[85, 88, 172] PEG,[100] chitosan,[84, 173, 174] CA,[88, 113] gelatin,[172] PLLA[175]		Tissue engineering, drug-delivery system, nerve tissue

Poly(N-isopropylacrylamide-co-N-methylolacrylamide) (poly(NIPAAm-co-NMA), poly(butyl acrylate-co-styrene) (PBS), poly(vinyl alcohol) (PVA), poly(caprolactone) (PCL), poly(methyl methacrylate) (PMMA), poly(vinylidene fluoride) (PVDF), Teflon® amorphous fluoropolymer (Teflon® AF), poly(3-hexylthiophene):phenyl-C61-butyric acid methyl ester (P3HT:PCBM), poly(3,4-ethylenedioxythiophene) polystyrene sulfonate (PEDOT:PSS), multiwalled carbon nanotubes (MWNTs), benzoic acid (BA), phenanthroline (phen), Crystal violet lactone:bisphenol A (CVL:BPA), cellulose acetate (CA), nanoparticles (NPs)

[a)] Dimethylvinyl-terminated dimethyl siloxane (resin monomer), methyl hydrogen dimethyl siloxane (curing agent)

Electrical/electrochemical applications

Coaxial electrospinning has been widely used in electrical/electrochemical applications including dye-sensitized solar cells (DSSCs),[147, 158, 162] organic

solar cells,[150, 166] gas sensing,[102, 160, 164, 165] lithium-ion (Li-ion) batteries[90, 116, 159, 167, 176] and Li-air batteries.[163] Recent developments are highlighted in **Table 1-3** according to the applications, material compositions, structures and characteristic features.

Table 1-3 Electrical/electrochemical applications of coaxially electrospun nanofibers

Application	Materials (Core/shell)	Solvents (core/shell)	Structures	Features	Ref.
DSSCs	TiO_2 precursor /Nb_2O_5 precursor	DMF /DMF	Core–shell nanofiber	Reducing charge recombination by structure and material	[147]
	TiO_2 precursor /ZnO precursor	DMF, acetic acid /DMF	Core–shell nanofiber	Surfactant-assisted synthesis of nanofibers	[162]
	PVAc,TiO_2 precursor /PVP, MgO precursor,	Acetic acid /DMF	Solid nanofiber	Fabrication of metal oxide core–shell nanofibers	[158]
Organic solar cells	P3HT:PCBM /PCL	Chloroform /chloroform, DMF	Solid nanofiber	Using unelectrospinnable P3HT:PCBM blends	[150]
	P3HT:PCBM /PVP	Chloroform /chloroform, ethanol	Solid nanofiber	Providing unperturbed percolation pathways for efficient charge transport	[166]
Gas sensing	Mineral oil /PVP, PS colloids	Mineral oil /H_2O	Hollow nanofiber	Macroporous semiconductor metal oxide nanostructures	[102]
	Mineral oil /titanium isopropoxide, PVP	Mineral oil /acetic acid, ethanol	Hollow nanofiber	Increasing surface-to-volume ratio for CO sensing	[160]
	Zinc nitrate hexahydrate, PVA	H_2O	Solid nanofiber	Outstanding selectivity to ethanol vapor	[164]

	/indium nitrate hydrate, PVP	/DMF, ethanol			
	$SnCl_2$,PVP /PVP, $HAuCl_4 \cdot 4H_2O$	DMF, ethanol /DMF	Core–shell nanofiber	High response and good selectivity due to core–shell structure and Au doping	[165]
Displays	Fe_3O_4, PMMA /$Eu(BA)_3$phen + $Dy(BA)_3$phen, PANI, PMMA	DMF, chloroform /DMF, chloroform	Core–shell nanoribbon	Trifunctionality (fluorescent color, electricity, magnetism)	[168]
	Fe_3O_4 NPs /$Tb(BA)_3$phen, PVP	DMF /ethanol, acetic acid	Core–shell nanofiber	High fluorescent and magnetic properties	[169]
Magnetic nanofibers	PAN-grafted Fe_3O_4@SiO_2@ PAN NPs /PAN	DMF /DMF		Combining surface-initiated reversible addition-fragmentation chain transfer (RAFT) polymerization and coaxial electrospinning	[177]
Microelectronics	PVP, $Ti(OBu)_4$ sol /paraffin oil /PVP, $Ti(OBu)_4$ sol	Ethanol, acetic acid/paraffin oil/ethanol, acetic acid	Tube-in-wire nanofiber	Multiple-fluid coaxial electrospinning	[151]
Li-ion batteries	PAN /SAN, silicon /PAN	DMF /DMF /DMF	Tube-in-tube nanofiber	Enhancing battery performance via a conductive carbon-core conducting path	[90]
	PAN, PS, silicon /PAN	DMF /DMF	Honeycomb-like nanofiber	Internal honeycomb-like structure as a conductive framework	[116]
	SAN, silicon, MWNTs /PAN	DMF /DMF		Enhancing battery performance using a conductive carbon-core conducting path	[167]
Li-air batteries	PAN /PVP, $Pt(AcAc)_2$	DMF /DMF	Solid nanofiber	Carbon nanofibers with metal (Pt, Co or Pd) nanoparticles on their surfaces	[163]

Li-air battery membrane separators	Teflon® AF-PVDF /PVDF-Teflon® AF	Perfluoro compound FC-75[a] /perfluoro compound FC-75	Core–shell nanofiber	Electrospun Teflon® fibers from coaxial electrospinning	[149]
Hydrogen storage	Ammonia borane/PS	DMSO or DMF /DMF	Hollow nanofiber	Electrospun conducting core material	[31]

Polyvinyl acetate (PVAc), polyaniline (PANI), acetylacetonate (AcAc), dimethyl sulfoxide (DMSO)
[a] IUPAC name: 2,2,3,3,4,4,5-heptafluoro-5-(1,1,2,2,3,3,4,4,4-nonafluorobutyl)-tetrahydrofuran)

Conducting and semiconducting polymers were unelectrospinnable, but they have become usable because of technique development and the ability to control new parameters.[150, 153, 166, 171] Coaxially-electrospun conducting polymers have excellent performance and are suitable as key materials for various electrical applications. For example, Lin *et al.* reported the flexible, bendable, thermoresponsive and conductive (29.4 S cm^{-1}) polymer nanofibers (PEDOT:PSS/(PBS) or poly(NIPAAm-co-NMA) core-shell fibers).[153] Ameri *et al.* and Kim *et al.* fabricated P3HT:PCBM/ PVP[166] and (poly(caprolactone) (PCL)[150] core-shell nanofibers for field-effect transistor, photodiode and photovoltaic device applications.[162] These semiconducting fibers helped to balance ambipolar charge transport, which resulted in enhanced photo response and higher power conversion efficiency compared with thin-film photoactive materials. PANI (core)/PVDF (shell) was coaxially electrospun for an energy-harvesting application.[178] The fabricated core–shell fibers were located between an anode and a cathode and were used in a microrobot for energy harvesting from a human artery. On the other hand, highly conductive materials, which can capture hydrogen but was unelectrospinnable (e.g., ammonia borane (NH_3BH_3)), was successfully

fabricated into core material in coaxial electrospun nanofibers, demonstrating a potential application of a stable and lightweight material for hydrogen storage field.[31]

One of the critical challenges in DSSCs is to reduce charge recombination. This can be accomplished by constructing energy barriers and reducing recombination sites.[147] Electrospun TiO_2/MgO core–shell nanofibers were cut into nanorods (short nanofibers) via an ultrasonication process and were used as a photoanode in a flexible DSSC.[158] The MgO provided an energy barrier between the TiO_2 and the electrolyte, which resulted in suppressed recombination and, furthermore, the fiber form reduced the number of electron trapping sites compared with the nanoparticle form. This resulted in improved high electron collection efficiency. A fabricated flexible nanorod-containing textile has applications in new energy and environmental technologies, but additional end-uses could be found simply by changing the materials. For example, TiO_2/Nb_2O_5[147] and TiO_2/ZnO[162] core–shell nanofibers fabricated for DSSCs showed 28 and 30%, respectively, improved conversion efficiencies. Future work should clarify the effects of shell thickness and average fiber diameter on the performance of DSSCs.

Coaxially-electrospun composite nanofibers have been intensively studied in connection with Li-ion batteries (specifically, as anode materials) to solve key issues of conventional anode materials, i.e., the low specific capacity of carbon, large volume expansion of newer anode materials (Si, Sn and SnO_x) and the low conductivity of Si.[23, 90, 179] These limitations have been overcome using core–shell nanofibers. High specific capacity and good capacity retention were achieved

by locating Sn or Si in the empty core and forming a carbon shell using a carbon precursor polymer.[27, 122] Lee *et al*. attempted to overcome Si's limitations via tri-axial electrospinning in this manner. The trilayered nanofibers were designed as carbon/Si and void /carbon. Direct contact between the electrolyte and active material was prohibited simultaneously, restraining continuous SEI formation. More Si could participate in electrochemical reactions with Li ions by which the carbon core additionally provided an electrical path. The electrical conductivity further increased by embedding of carbon nanotubes.[167] Zhang *et al*.[116] fabricated a honeycomb-like conductive carbon network using porous carbon and embedded silicon nanoparticles as the material for the core and a compact carbon shell. The resulting structure was used as an anode for lithium ion batteries, and exhibited higher cyclic performance than pure silicon nanoparticles. However, more attempts such as increasing initial efficiency and optimizing structure design are necessary for practical applications.

Biomedical applications

Electrospinning has been widely used in biomedical applications such as nanofibrous cellular scaffolds for tissue engineering and drug-delivery systems. The process can be readily adjusted to control the diameters, pores and structures of nanofibers having high surface-area-to-volume ratios from various biocompatible and biodegradable polymers.[180-184] These properties can enhance cell attachment and drug loading, and can mimic the structure of the extracellular matrix.[180, 182,

185] The main contribution of electrospun nanofibers is that of providing flexibility in material selection and the ability to use fibers having different compositions and structures.[181] The coaxial electrospinning process has widened the selection of biocompatible materials and provided enhanced structures for biomedical applications, e.g., drug-delivery systems.[24, 185-188] Furthermore, the process is an innovative approach because two or more materials can be combined in a single fiber, leading to the developments of new applications.[91, 185]

The combination of challenging biocompatible polymers via coaxial electrospinning has been reported, including high-molecular-weight chitosan,[24] silk-elastin-like protein polymer[189] and self-immolative polymer.[190] Chitosan fibers, which are non-toxic and have excellent mechanical strength, are difficult to electrospin because of their polycationic character and high molecular weight.[84, 191] High-molecular-weight (690,000 g mol^{-1}) chitosan nanofibers have been fabricated using coaxial electrospinning.[24] The shell chitosan solution was successfully electrospun by leveraging the excellent electrospinnability of the core solution such as polylactic acid (PLA),[24] PEO,[84] and PCL.[173] PCL was chosen to compensate the decrease in the mechanical properties of chitosan due to biodegradation, while chitosan provided hydrophilicity to the composite. These complementary strategies have been used to improve mechanical or surface properties.[121, 175, 192] PLA is biodegradable material but a weak and hydrophobic. Combining it with PVA as the core by coaxial electrospinning improved the hydrophilicity and mechanical properties.[175] On the other hand, silk fibroin[104] and gliadin,[33] which are promising biopolymer candidates, could be

coaxially electrospun into fibers.[193, 194] **Table 1-4** summarizes recent research on the fabrication of nanofibers using coaxial electrospinning for biomedical applications. These approaches have encouraged research in the biomedical field, but difficulties in identifying the optimal solution and process parameters remain as limitations.

Table 1-4 Biocompatible/biodegradable polymer fibers made by coaxial electrospinning

Materials (core/shell)	Solvents (core/shell)	Structures	Features	Ref.
PLA/chitosan	TFA/acetic acid, TFA	Core–shell nanofiber	Electrospun chitosan assisted by good electrospinnability of PLA	[24]
Gliadin/solvent	HFIP/HFIP	Solid nanofiber	Electrospun using traditional and modified coaxial electrospinning	[33]
CA/solvent	Acetone, DMAc/DMAc	Solid nanofiber	High-quality (smooth surface and structurally uniform) nanofibers	[58]
PEG/PLLA	H_2O/DCM,DMF	Hollow nanofiber	Epitaxial-like packed monolayered hollow fibrous membranes	[100]
PEO/chitosan	Aqueous acetic acid,H_2O/aqueous acetic acid	Hollow nanofiber	Electrospun challenging material chitosan with aqueous solution	[84]
PEO/PCL	Aqueous acetic acid,H_2O /aqueous acetic acid	Hollow nanofiber	Closer to the size of the axons to mimic	[85]
Oil/CA	Chloroform, methanol/acetone, dioxane	Hollow nanofiber	Hollow structure after washing core material	[88]
Natural silk fibroin/silk sericin	H_2O/H_2O	Core–shell nanofiber	Mimicking silkworm silk	[104]

PCL/gelatin	TFE/TFE, glacial acetic acid	Core–shell nanofiber	Electrospun functionalized gelatin	[172]
PCL/chitosan	Chloroform, methanol/TFA	Core–shell nanofiber	Fabricating 3D scaffolds	[173]
PEO/thermoplastic CMC[a)]	Chloroform, methanol/DMF	Core–shell nanofiber	Electrospun grafting copolymer with aid of PEO	[120]
PVP/PAN,SIP	DMF/DMF	Core–shell nanofiber	First electrospun self-immolative polymer nanofiber	[192]

Polylacticacid (PLA), trifluoroacetic acid (TFA), 1,1,1,3,3,3-hexafluoro-2-propanol (HFIP), 2,2,2-trifluoroethanol (TFE), carboxymethyl cellulose (CMC), self-immolative polymer (SIP)
[a)] Grafting methyl acrylate (MA) onto sodium carboxymethyl cellulose (NaCMC)[120]

Coaxial electrospinning is particularly attractive for drug delivery systems; **Table 1-5** summarizes recent advances. Various nanofibers fabricated *via* coaxial electrospinning have been shown to have controlled drug-release profiles.[181, 195] These were attained by several approaches including physical (wall thickness and pore), structural (trilayered) and functional (hydrophilicity and hydrophobicity, stimuli-response) modifications.

Table 1-5 Drug delivery system produced by coaxial electrospinning

Materials (core/shell)	Solvents (core/shell)	Model drugs	Features	Ref.
PEG/PLA	DCM, DMAc /DCM, DMAc	Salicylic acid (shell)	Porous and non-porous surface controlled by feed rate of core	[25]

Gliadin/solvent	HFIP /HFIP	Ibuprofen	Uniform distribution of drugs aid of modified coaxial electrospinning	[33]
Hypromellose, PEG/solvent	Ethanol, dichloromethane /ethanol	Ferulic acid	Electrospun hydrophilic composites	[34]
Zein/solvent	Ethanol,H_2O /DMF	Ibuprofen	Sustained drug-release profiles	[59]
CA/solvent	Acetone, DMAc, ethanol /acetone, DMAc, ethanol	Ketoprofen	High-quality (uniform structure and smooth surface)	[58]
PVP, sodium hydroxide/PVP, citric acid	Ethanol, H_2O /ethanol	Quercetin	Containing acid–base pairs, to improve solid dispersions	[196]
PVP/PVP, SDS, sucralose	DMAc, ethanol /ethanol, H_2O	Acyclovir	Solid dispersion for poorly water-soluble drugs	[117]
Ferulic acid/CA/solvent	Acetone, ethanol, DMAc/acetone, ethanol, DMAc/acetone, ethanol, DMAc	Ferulic acid	Electrospun by modified triaxial electrospinning process	[197]
Solvent/PEO	DMF/H_2O, NaCl	Cisplatin (core and shell)	Nanofiber with repeating beads structure	[107]
Solvent/CA	DMF /acetone, DMAc	Cisplatin (core and shell)	Nanofiber with beads structure	[107]
Acetic acid/CA-gelatin	Acetic acid/Tween® 40	Amoxicillin	Hollow nanofiber	[198]
PCL/gelatin	TFE/TFE, H_2O	Metronidazole	Effective for alleviating initial burst release	[18]
PVP/PVP, SDS	DMAc, ethanol/ethanol aqueous solvent	Quercetin	Fast-dissolving delivery systems (FDDS)	[199]

Ethyl cellulose/PVP	Ethanol/DMAc, ethanol	Ketoprofen (core and shell)	Biphasic release: immediate and sustained release characteristics	[199]
EL 100/ES 100 or EL 100/ES 100[a)]	Ethanol, DMAc/ethanol, DMAc	KAB dye (core)/KAU dye (shell)	pH-sensitive layer for target delivery	[91]
PVP/PCL/PCL	H_2O/chloroform, TFE/TFE	KAB dye (core)/KAU dye (shell)	Enhanced efficiency by trilayered structure	[91]
PVP/PCL/CA	TFE/TFE/TFE	Nisin	Long-term antimicrobial activity combined with a hygroscopic outer layer	[187]
PVP/PAN,SIP	DMF/DMF	KAB	Alteration of drug release profile when triggered	[192]

cis-Diammineplatinum(II) dichloride (cisplatin), sodium dodecyl sulfate (SDS), Keyacid Blue (KAB), Keyacid Uranine (KAU)

[a)] Eudragit® L 100 (EL 100), Eudragit® S 100 (ES 100)

Controlled drug-release profiles were obtained by changing diffusion rate via wall thickness control of PCL/gelatin core–shell nanofibers[18] and controlling the pore size and distribution of salicylic acid (SA)-loaded PEG/PLA core–shell fibers.[25] The wall thickness was successfully controlled by adjusting the concentration or feed rate of the shell solution, while the porosity was controlled by the feed rate of the core solution; increasing feed rate decreased the pore density.

Han *et al.* reported a possibility of a dual-drug delivery system consisting of a PVP/PCL/PCL trilayered structure using multicoaxial electrospinning.[91] The burst release was observed from the shell while the core showed sustained release due to the barrier effect of the intermediate layer.[91] This concept was further employed to produce nisin-loaded trilayered electrospun fibers by providing additional functionalities in the intermediate layer. The fabricated fiber displayed better long-

term antimicrobial activity compared with other electrospun fibers made by single and coaxial electrospinning techniques. This was attributed primarily to the role of the intermediate layer that prevented interference between the core and shell layers.[187]

To effective delivery of drugs, hydrophilicity and hydrophobicity or acidity was utilized actively in nanofibers, depending on the properties of drugs. For example, when a drug was poorly water-soluble, hypromellose containing amphiphilic group (with hydrophobic and hydrophilic groups) was effective for the delivery of this drug because it was combined with the drug in the core and electrospun into fibers with the help of solvent in the shell.[34] When a drug was acidic (e.g., quercetin), materials containing acid-base pairs (e.g., PVP) were effective for drug delivery, which was demonstrated by coaxial electrospining of PVP, hydroxide and quercetin (as model drug) in the core solution and citric acid and PVP in the shell solution.[196] A drug (e.g., ketoprofen) was incorporated into both core (ethyl cellulose (EC)) and shell part (PVP). Due to the hydrophobicity and hydrophilicity of core and shell materials, biphasic release was observed, i.e., immediate drug release followed by a constant release due to the characteristics of each layer.[199]

Programmed and targeted release was achieved by developing pH-responsive core–shell nanofibers. The core–shell fiber membrane consisted of different Eudragit® polymers that dissolve in different pH ranges.[200] In this way, targeted release in a desired pH environment can be achieved; this may provide improved therapeutic efficacy and safety of drug-delivery systems.[181] Stimuli-responsive and smart fibers are another novel area of electrospinning research;[18, 91, 186] stimuli include

immune[201] and enzymes,[202] and subsequent (responsive) reaction can be self-immolative depolymerization.[192]

Numerous concepts and approaches have been attempted to overcome challenges in the biomedical field. Some studies have focused on the effect of microstructural dispersion of drugs in polymer matrices on the drug-release profiles.[117, 197] Yang *et al.* prepared ferulic acid-loaded nanofibers via different electrospinning processes and compared their microstructures. Core-shell and trilayered nanofibers showed homogenous and heterogeneous distributions of drugs, respectively.[197] Accordingly, different release behaviors were observed. On the other hand, coaxial nanofibers have been applied to enzyme system.[90, 203] Ji *et al.* fabricated hollow nanofibers for a bienzyme system and a cascade reaction at the oil/water interface; glycerol was used as the core and PU as the shell material, and two different catalysts were incorporated into core or shell.[90] They engaged the flexibility of the coaxial electrospinning process in material selection to modify the nanofiber structure (core–shell, hollow) and to encapsulate various functional materials in desirable locations.[185, 188] The formed nanofibers displayed a significant improvement (about 100 fold) in biocatalytic efficiency compared with free enzyme system.

Environmental applications

Coaxially-electrospun fibers are widely used in environmental applications that require fibrous structures having high specific surface area, an interconnected pore structure and robust mechanical properties.[204, 205] These applications include oil collection or oil/water separation and waste water treatment.[94, 206]

The most important factor for an oil collector is its oil absorption capacity. Other required properties include robust mechanical properties for reusability, and selectivity toward a target pollutant. Lin *et al*. fabricated and examined the oil absorption capacity of a 3D mat of PU/PS core–shell fibers.[207] Intra-pores and inter-fiber void were generated due to the interface between the core and shell solutions. They found that the oil absorption capability depended largely on the inter-fiber voids rather than on the intra-fiber pores because the oil was predominantly and physically trapped in the inter-fiber voids. The 3D mats were reusable after squeezing at high pressure and showed no critical decline in absorption capacity; this was attributed to the combined effect of the strength and elasticity of PU with the hydrophobicity/oleophilicity of PS.

For water filtration, zein nanoribbons/cellulose acetate (CA)[208] and a poly(2-aminothiazole) (PAT)/cellulose acetate[209] core-shell fiber membrane were fabricated to remove Pb(II) and Hg(II) ions from polluted water. These nanofibers showed a maximum removal of Pb(II) of 89.36 mg g^{-1} and Hg(II) of 177 mg g^{-1}. Notably, Wen *et al*. used a sodium lauryl sulfate solution to overcome protein–metal interactions in coaxial electrospinning.[208] Zou *et al.* compared the removal ability of a core–shell fiber membrane and nanoparticles based on PAT and CA. The core-shell nanofibers had much higher adsorption capacity due to the high specific surface area. Additionally, hollow microfibers have been used to create an ultrafiltration membrane for filtering water using various shell polymers including PVDF-HFP, poly(etherimide) and polysulfone.[55] These are developing applications of the

coaxial electrospinning process and further improvements are expected. A logical extension of the research would relate to gas purification applications.

Other applications

Core–shell fibers containing thermoelectric,[210] thermochromic,[171] thermoresponsive[153] and thermoregulating[46] materials have been produced using coaxial electrospinning. Rahimi *et al.* fabricated a HD/PU fiber mat for a thermoregulating protective clothing application capable of maintaining a constant temperature or to cool-off via a phase change of the HD.[46] Shape-stabilized phase change materials (PCMs) have also been used to produce thermally-intelligent core–shell nanofibers.[211] PEG was used as a PCM in PEG-CA fibers. Differential scanning calorimetry studies of thermal cycling tests showed that the thermal stability of the core–shell fibers was better than that of the pure PEG fibers because, upon heating, the molten PCM was confined to the fibers due to the shielding effect of the shell. The thermal properties of core–shell fibers can be enhanced by controlling the composition of the core and shell solutions, and the structures of the fiber interior. These fibers are expected to find use in thermal energy storage systems and temperature-regulating garments.[211]

1.1.6. Limitation and perspective of electrospinning

Newly developed process: Needleless electrospinning

The advantage of the traditional needle-based electrospinning process is its capability with regard to fabricating delicate structures. However, the low productivity of coaxial electrospinning presents a serious limitation to widespread applications of this technique.[2, 184, 212, 213] Needleless electrospinning has been developed to address this disadvantage. The different methods include surface,[43] cylindrical-electrode,[44] free-surface,[45] dual-wire emulsion,[56] spiral,[214, 215] and slit-surface electrospinning processes.[215] **Figure 1-4** shows representative equipment and **Table 1-6** presents the main approaches or methods, their characteristic features and the advantages and disadvantages of needleless electrospinning.

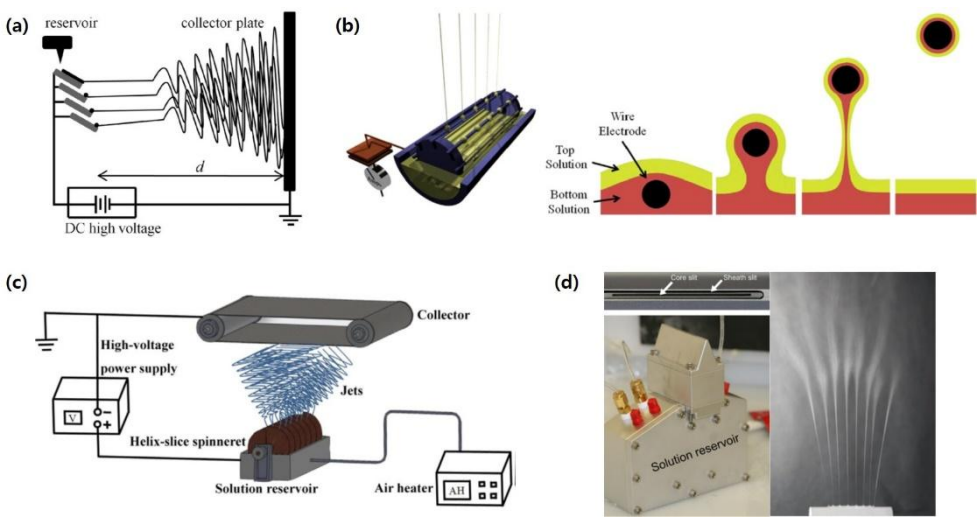

Figure 1-4 Illustrations and images of needle-less electrospinning processes; (a) surface-based electrospinning.[43] Reproduced with permission. Copyright 2010, Elsevier. (b) Free surface electrospinning from wire electrodes. [45] Reproduced with permission. Copyright 2013, Elsevier. (c) Spiral electrospinning.[215] Reproduced with permission. Copyright 2015, Elsevier. (d) Slit-surface electrospinning.[45]

Table 1-6 Comparison of various needleless electrospinning processes and their characteristic features.

Electrospinning process	Approach/method	Advantages	Disadvantages	Ref.
Surface-based (**Figure 13**(a))	A plate used as a voltage substrate	High-throughput (0.27 g h^{-1}), almost 10-times greater than needle-based electrospinning	Single-phase electrospinning process	[43]
Cylindrical-electrode	Single-edged cylindrical electrode	High-throughput (5.2 g h^{-1}), almost 260-times greater than needle-based electrospinning	Single-phase electrospinning process	[44]
Free-surface (**Figure 13**(b))	Wire electrode instead of needle	Fabrication of core–shell nanofibers	Only effective with immiscible solutions	[45]
Dual-wire emulsion	Dual-wire electrodes instead of needles	Fabrication of core–shell nanofibers	Effective with immiscible or less miscible solutions	[56]
Spiral (**Figure 13**(c))	Helical slice-spinneret electrode	High-productivity (40–400 g h^{-1}), thousands of times greater than needle-based electrospinning	Effective with immiscible solutions	[214] [215]
Slit-surface (**Figure 13**(d))	Co-localize two solutions along a slit surface	High-productivity (1 L h^{-1}), greater than needle-based electrospinning	High operating voltage (70–90 kV)	[215]

The needleless processes have demonstrated high productivity, from tens to thousands of times greater than traditional needle-based electrospinning processes.[43-45, 56, 214, 215] The free-surface,[45] dual-wire emulsion[56] and slit-surface electrospinning processes[215] can be used to make core–shell fibers. However, each process has its limitations. For example, immiscible or poorly

miscible solutions can only be used to fabricate core–shell fibers. This narrow selection of polymers that can be selected hinders application development. Nevertheless, further research is warranted because the approach can potentially produce fibers with delicate structures in mass production. As an example, the diameters of core–shell fibers are controllable from 144 to 3400 nm using the dual-wire emulsion electrospinning process.[56] Although the productivity of this process is still somewhat lower than other emerging processes, it could be improved by modifying the method of droplet attachment. The mechanisms of cone-jet formation are unclear, and the interrelationships of the process parameters should be investigated; careful study will lead to optimization of this promising technique.

1.2. Research objectives

In this thesis, the objectives are fabricating inherently helical silver nanofibers using electrospinning process and apply the electrospun silver nanofibers as a transparent and stretchable. For those purpose experimental and theoretical approaches were conducted to understand basic physics involved in electrospinning process and to design proper process to fabricate helical silver nanofibers.

In chapter 2. a numerical model for simulating the electrospinning and gas-assisted melt electrospinning process were developed to figure out the roles of process parameters and to understand physical phenomenon involved. Also, expansion of process was conducted for a mass productive multi-nozzle system. Firstly, a multi-physics model for single-nozzle system was developed. Process parameters

including applied voltage and hot air flow rate were investigated. Then to expand the model for multi-nozzle system, electric field distribution according to multi-nozzle array was calculated depending on number of nozzles, distance between nozzles and applied voltage. Finally, by applying the calculated electric field as potential boundary condition for single-nozzle model, a multi-nozzle system was simulated.

In chapter 3, an electrospinning process designed by focusing on solvent vapor pressure, electric field distribution, nozzle geometry, and electrical properties of solution. Previous research about electrospun helical fibers reported about formation of intrinsic curvature or initial twisting at the early stage of electrospinning, suggesting that the position of solidification of the jet can be considered as one of the crucial factor to fabricate helical structure. Therefore, solidification behavior of an electrospun jet was investigated. Two sets of experiments and simulation were conducted. First, dielectric polymer solution with different composition of solvents to vary the vapor pressure was prepared and structure of electrospun fiber according to solvent vapor pressure was investigated. Then, conductive polymer solution which contained a large amount of silver ions was prepared to control the thickness of the jet and the solidification position. Numerical models were developed to simulate the jet behavior of the jet near the nozzle tip. Through this study basic principle for formation of helical fiber was proposed, and helical silver nanofiber was fabricated.

In chapter 4, transparent and stretchable electrode was fabricated using electrospun silver nanofiber and shape memory polymer as elastomeric substrate as an application. To fabricated transparent electrode, the metallic fibers of thin diameter

and low areal fraction is necessary. Therefore, a free-standing and continuous silver nanofiber network was prepared by electrospinning and following ultraviolet reduction. Then, fabricated silver nanofibers were transferred on prestrained substrate. Prestrained substrate has been used to modify the structure of nanofibers on it, however, the residual strain and resulting wrinkling has bad effects on repetitive stretching. Therefore, crosslinked polycyclooctene(PCO) was used as substrate which shows shape memory behavior and great mechanical characteristics. Due to the recovery behavior of the crosslinked PCO transparent and stretchable electrode was efficiently fabricated. Shape memory polymer – transparent and stretchable electrode was demonstrated which was bendable and recoverable when applying electrical stimuli.

For those purpose experimental and theoretical approaches were conducted to understand basic physics involved in electrospinning process and effect of newly emerging parameters on behavior of electrified jet. Those parameters were nozzle geometry, electric field distribution, solidification position of jet, and electrical properties of spinning solution. Considering effects of those parameters on the structure of electrospun fibers we designed process to synthesize helical silver nanofibers.

Chapter 2. Numerical simulation of gas-assisted melt electrospinning

2.1. Needs for modeling of gas-assisted melt electrospinning

Nano- or sub-micro polymeric fibers are one of the most notable nanomaterials due to their unique physical and chemical properties,[216] which include a high aspect ratio, high surface area-to-volume ratio, and porosity.[217] In addition, the mechanical properties of nanofibers differ from those of bulk materials due to the alignment or drawing effect that occurs during the spinning process.[218, 219] Accordingly, nanofibers are extensively used in various functional materials,[220] which range from structural composites such as carbon nanofibers to those used in optical devices, chemical sensors, electrodes, and biomedicines.[165, 221-227] The inherently flexible features of nanofibers are beneficial for use in wearable devices and e-skins, an emerging research field in recent years.[220]

There are several thin-fiber fabrication methods, among which electrospinning has been regarded as a simple and efficient technique since its introduction at the beginning of the 20th century.[228, 229] In electrospinning, a polymer melt or polymer solution is used. With respect to solution spinning, a solution is ejected in the form of a jet by electric force generated by application of high voltage to the solution-loaded nozzle tip. The electric force can be classified into body and surface forces due to electrical polarization of the solution and surface charges that accumulate at the external interface, respectively.[230, 231] If the forces acting on

the solution exceed the critical strength, the jet is ejected from the solution pendent by overcoming the surface tension and inertia forces;[232] the ejected jet maintains its fibrous structure due to moderate viscosity resulted from entanglements between polymer chains.[228, 230] Concurrently, the jet undergoes bending and whipping behavior due to the evolution of axisymmetric and non-axisymmetric instabilities generated by many factors, such as surface charge perturbations by evaporation of the solvent and surface effects from air drag.[36, 233] As a result, the fiber diameter decreases to the nanoscale level.[39, 234] In this context, an appropriate level of conductivity is required for solution electrospinning, thereby limiting polymer and solvent selection; this constraint lowers productivity to a few grams per day.[220, 235]

Electrospinning using a polymer melt has a similar mechanism; however, the difference has to do with the conductivity of the liquid. Generally, the conductivity of a polymer melt is low (10^{-9}–10^{-10} S/m), which limits movement of the surface charge to the external interface.[14] In addition, a relatively low electric force is applied, as there is no solvent to enhance conductivity. Because of the rapid solidification of the ejected jet, the surface charges at the interface are easily trapped; therefore, the jet does not enter the whipping stage where most stretching occurs.[236-238] Polymer melt electrospinning generally enables efficient microfiber fabrication, due to the absence of solvent evaporation for additional shrinkage.[239-242] Increased productivity is an important factor in industry;[243] thus, electrospinning using air flow has been introduced to utilize solution and polymer-melt electrospinning processes.[217, 244] Zhmayev et al. proposed a gas-

assisted melt-electrospinning (GAME) process to improve nanofiber productivity for a wide range of materials, using conventional melt-blown spinning and electrospinning methods.[245] In GAME process, hot air is ejected along with the polymer melt to maintain the temperature to prevent quenching or solidification of the melt. As a result, polymer jet gets electrical force for longer time due to inhibition of charge trapping by immobilization. Also, as air flow drags the polymer melts, the jet stretches more and thereby forms thinner fibers. Thus, GAME process enhances the productivity and quality of fibers. However, there have been lack of theoretical analysis and experiments about GAME process. Therefore, we first tried to figure out the crucial factors of successful fabrication of fibers by analyzing the forces acting in GAME process. Based on prior analysis, we attempted to provide processing conditions of multi-nozzle system for massive production using GAME process.

In this study, we developed a numerical model for simulating the GAME process to analyze forces acting on jet formation; we also introduced a criterion of shear viscous stress for predicting spinnability. The force for forming the jet was calculated, then used to predict change in jet radius by analyzing the shear viscous stress according to the processing parameters (air flow and applied voltage). We also proposed a criterion for the electric field strength, which is applicable to large-scale multi-nozzle systems.

2.2. Methods

2.2.1. Gas-assisted melt-electrospinning process

The apparatus configuration of the GAME process is similar to the co-axial electrospinning process with a concentric nozzle system **(Figure 2-1)**. The polymer melt is loaded into the core and hot air flows throughout the surrounding shell to facilitate spinning, similar to the melt-blown process; however, an electric potential is applied to the nozzle. Detailed descriptions of GAME can be found in [245]. As a model material, polypropylene (MF-650X, Polymirae, Korea) was chosen. The viscosity of the polypropylene was measured using a rotational rheometer (Discovery HR-1, TA Instruments, New Castle, DE, USA) at a frequency of 1 Hz, a heating rate of 5°C/min, and a measuring gap of 1.0 mm for the simulation results shown in **Figure 2-2(a)**. We assumed polypropylene melt as Newtonian fluid at given process condition because the shear rate at the process is in range of Newtonian plateau (**Figure 2-2(b)**).[246]

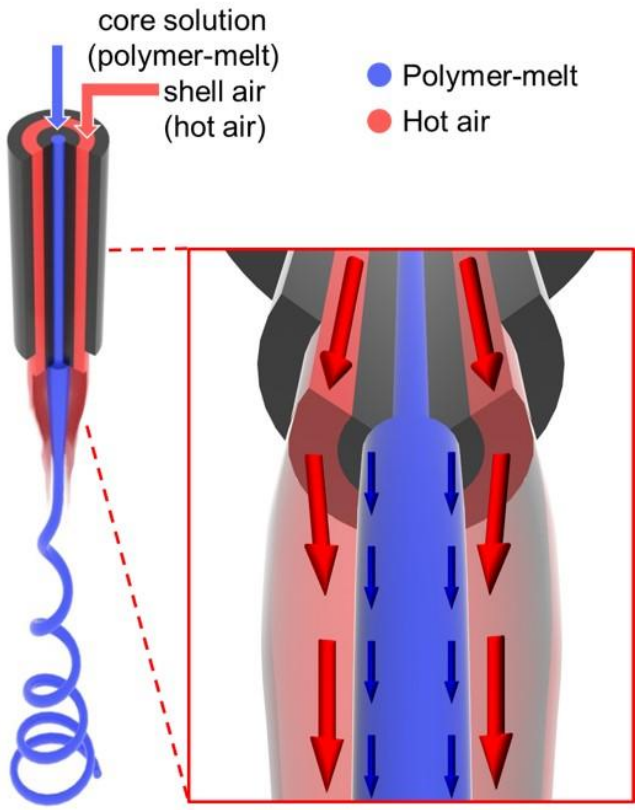

Figure 2-1 Schematic illustration of the gas-assisted melt-electrospinning (GAME) process. The polymer melt resides in the core of the nozzle, which is surrounded by a shell containing hot air. An electric field is applied to the end of the nozzle.

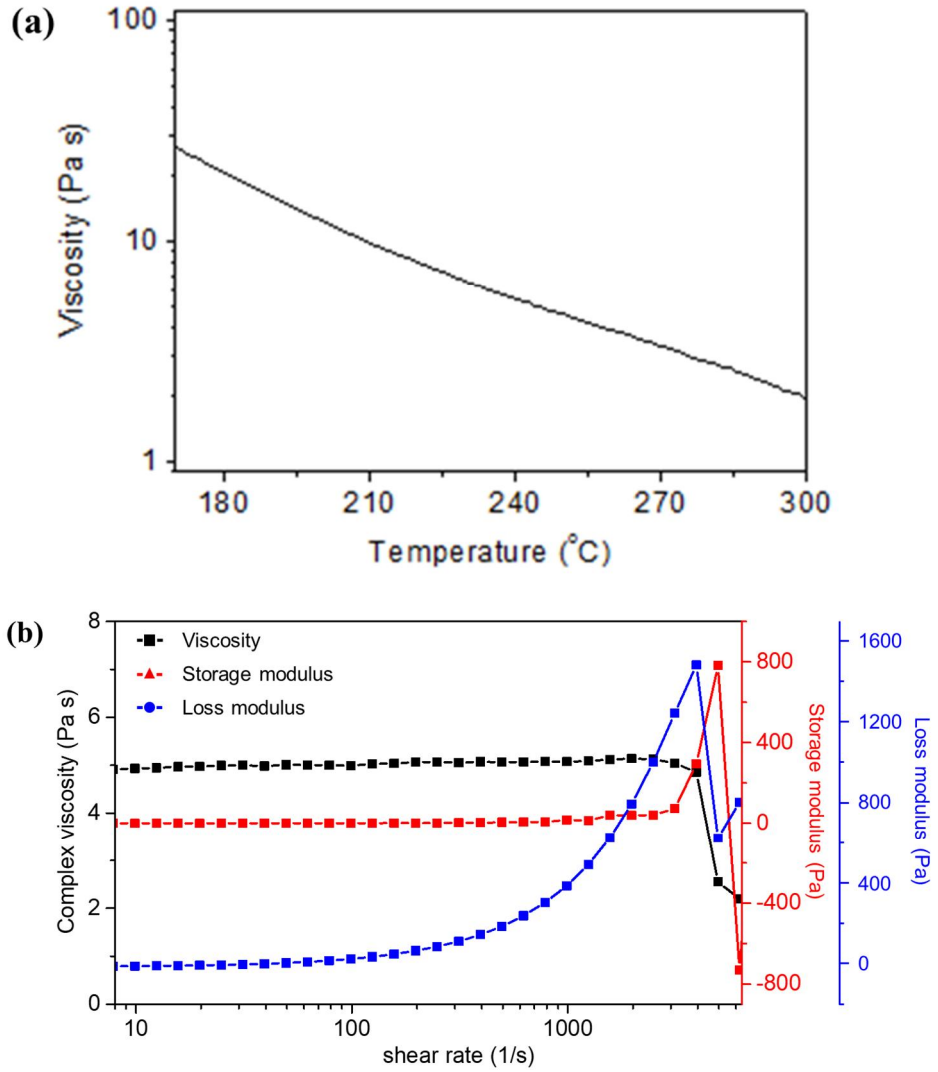

Figure 2-2 (a) Viscosity of polypropylene (PP) according to temperature (frequency: 1 Hz; heating rate: 5°C/min; measuring gap: 1.0 mm). (b) Complex viscosity, storage, and loss modulus of PP at 250°C.

2.2.2. Numerical simulation of single-nozzle GAME process

Numerical simulations were conducted using a commercial program (COMSOL Multiphysics®, version 5.2); the simulations were based on a level-set, laminar two-phase flow model and an electrostatics module.[247] In order to observe the phenomenon of jet formation from the droplet, the deformation process of polymer melt, including such conditions as heating to high temperature (250 ^{o}C) and moving at low speed, was simulated. Therefore, we assumed that the polymer melt exhibits like a Newtonian fluid. The geometry of the simulation model for the single-nozzle GAME process is shown in **Figure 2-3(a)**. Detailed boundary conditions can be found in Appendix. First, the electric field in a single-nozzle GAME model (a crucial factor regarding fiber electrospinnability) was calculated for each process condition (tip-to-tip distance and applied voltage).[248-250] To reduce computational time, this study used a two-dimensional axisymmetric geometry from our previous work involving co-axial electrospinning simulations.[247] Notably, the core nozzle containing the polymer melt was extruded by 2 mm from the shell nozzle tip.

(a)

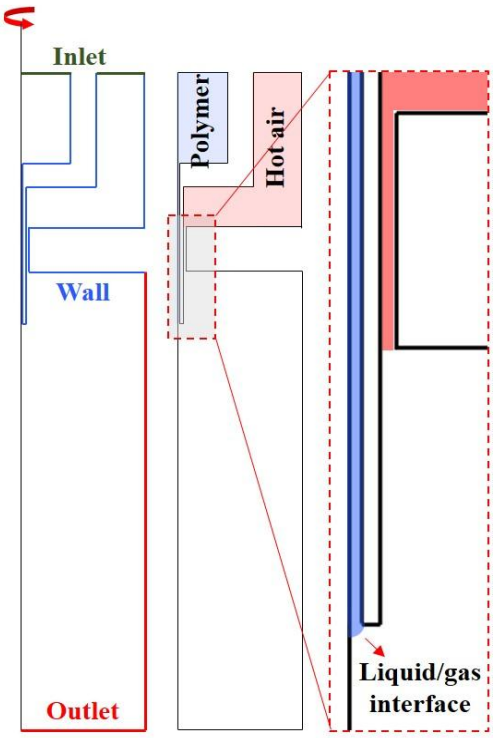
Inlet
Polymer
Hot air
Wall
Outlet
Liquid/gas
interface

(b)

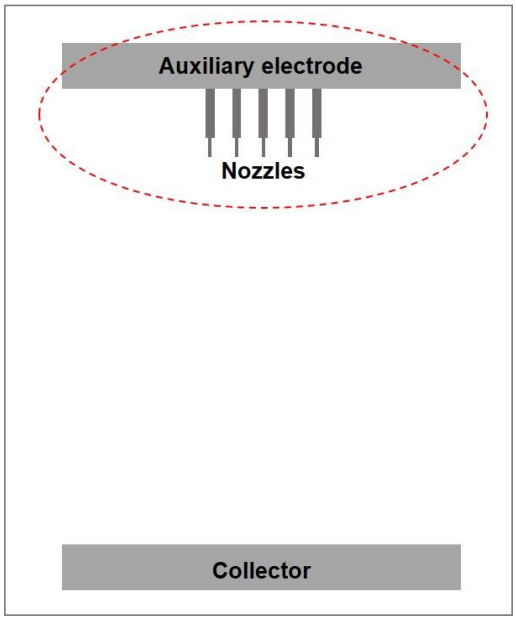
Auxiliary electrode
Nozzles
Collector

(c)

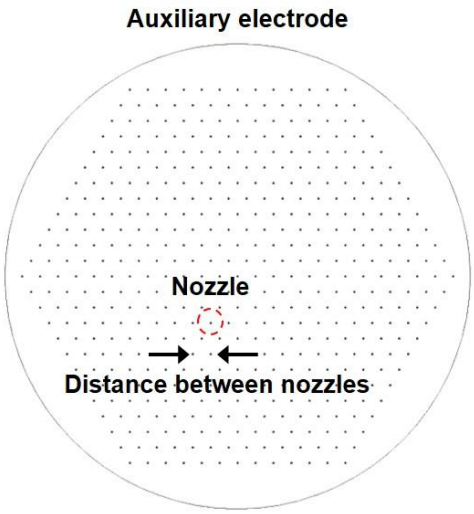

Figure 2-3 Geometry of the simulation model for the GAME process: (a) a single-nozzle model, (b) a three-dimensional multi-nozzle model, and (c) a multi-nozzle array model.

The governing equations for the multi-physics model included the Navier–Stokes equation for fluid dynamics, Maxwell stress for electric force, charge conservation, and Gauss's law for an electric field.[247, 251, 252] Since our work focused on the ejection of the jet, the capillary force was not considered in this study as it becomes less critical after the fluid ejected from nozzle. Detailed information regarding these equations can be found in **Appendix**. A parametric study was conducted regarding the processing parameters, hot air flow rate (0, 18, 36, 54, 72, and 108 L/h), and applied voltage (15, 18, 20, 22.5, and 25 kV); the effects of these parameters on jet

formation and propagation behavior were analyzed. The material properties and process parameters used in the simulation are listed in **Table 2-1** and **Table 2-2**.

Table 2-1 Material parameters for Gas-assisted melt-electrospinning (GAME) simulation

	Polymer	**Air**
Density (ρ, g cm^{-3})	9.10 x 10^{-1}	6.71 x 10^{-4}
Dynamic viscosity (μ, Pa s)	4.6	2.81 x 10^{-5}
Electric permittivity (ε, F m^{-1})	2.04 x 10^{-11}	8.85 x 10^{-12}

Table 2-2 Process parameters for GAME simulation

Nozzle diameter (mm)	Core	0.2
	Shell	0.635
Tip-to-collector distance (cm)		20
Polymer flow rate (ml hr^{-1})		1.2
Surface tension coefficient (N/m)		2.0 x 10^{-2}
Parameter controlling interface thickness (m)		5.0 x 10^{-5}
Temperature (K)		523

The morphological changes of a straight jet in the stable jet region were simulated without considering elastic die swelling or whipping phenomenon, under the assumption of a constant temperature due to the hot air, and the assumption that there was no enhanced quenching effect at a given distance.[253] The viscous shear force was defined to calculate the force applied to the melt to form a jet by sharpening the

droplet. Viscous shear force was calculated by integrating the force acting on the polymer melt surface in the region of 0.5 mm from the nozzle tip. The thickness of the jet was evaluated by observing the outermost streamline of the core nozzle. Finally, the relationship between jet thickness and shear stress was investigated to determine the critical stress criterion for good spinnability.

2.2.3. Calculation of electric field in multi-nozzle configuration

For single-nozzle electrospinning, the electric potential is generally applied directly to the spinneret (free electrode).[14] Given that it can be difficult to use this approach with a multi-nozzle system due to increased numerical instability,[254] a plate electrode (auxiliary electrode) was introduced, as this electrode is considered beneficial for stabilizing the process.[240] Thus, a plate geometry was used for calculating the electric field in the multi-nozzle system, as shown in **Figure 2-3(b)**. The tip-to-collector distance corresponded to the distance used in an actual electrospinning process. The differences between free and auxiliary electrode systems are shown in **Figure 2-4**. The purpose of simulating multi-nozzle GAME system is to predict the jet behavior and electrospinnability according to process parameters in multi-nozzle system for massive production, because one of the crucial limitations for solution, melt, and other electrospinning technique is productivity.[220, 235] Thus, since electric field distribution is known as one of the crucial factors in electrospinning,[255, 256] we calculated electric field distribution according to process parameters.

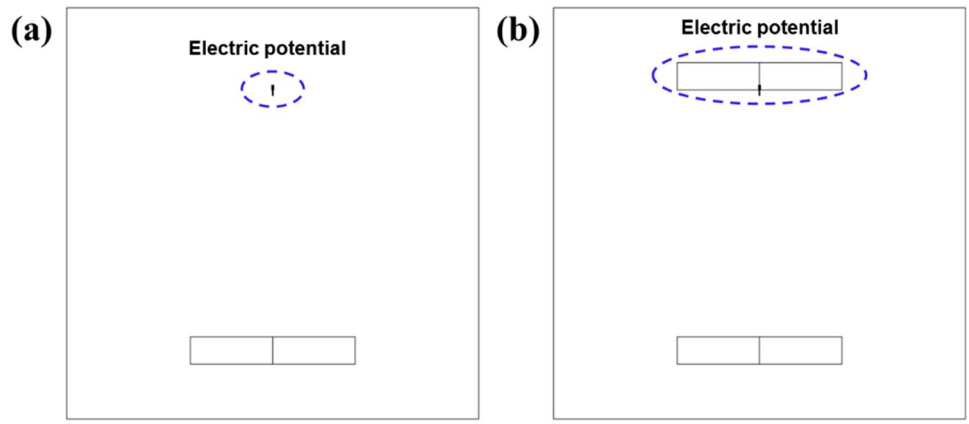

Figure 2-4 Model geometry of the GAME process with (a) a free electrode and (b) an auxiliary electrode.

The nozzles in the multi-nozzle system were assumed to be arranged in a hexagonal array to maintain a constant tip-to-tip distance; additionally, a uniform electric field was applied [**Figure 2-3(c)**]. The electric field distribution was calculated by varying the number of nozzles (1, 7, 19, 31, and 469), the tip-to-tip distance (5 to 40 mm), and the applied voltage (15 to 75 kV).

2.2.4. Numerical simulation of multi-nozzle GAME process

The multi-nozzle GAME process was simulated by applying the electric field calculated in Section 2.2.3 as the potential boundary of the simulation model described in Section 2.2.2 (see **Figure 2-5**). This simulation was also used to calculate the shear viscous stress on the jet by varying the processing conditions (voltage: 30 and 45 kV; tip-to-tip distance: 5 mm; number of nozzles: 1, 7, 19, 31,

and 469).

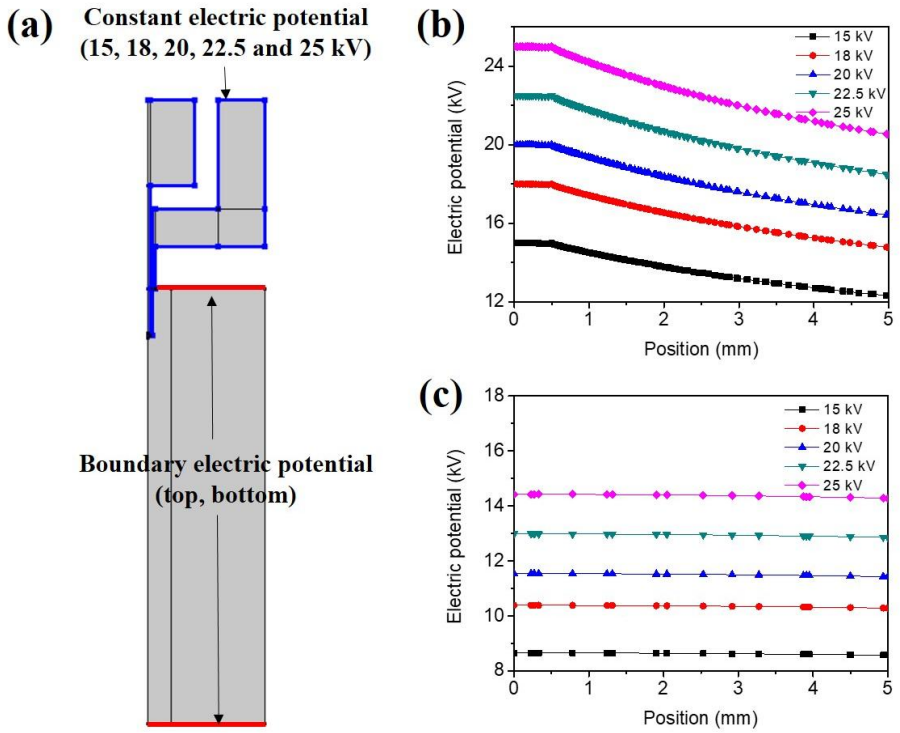

Figure 2-5 (a) Geometry and boundary conditions for multi-nozzle simulation. Electric field boundaries imposed at (b) the top and (c) bottom for simulation of a multi-nozzle array.

2.3. Results and discussion

2.3.1. Simulation of single-nozzle GAME process

The GAME process was simulated using the single-nozzle model shown in **Figure 2-3**(a) with the specified air flow and applied voltage. **Figure 2-6** shows the volume fraction and streamline of the air when a stable jet formed. Here, the stable jet indicates the straight jet ejected by the electrical force after sharpening of the liquid

pendent. The thickness of the jet affected by the process parameters. In Figure 2-6, jet became thinner as the air flow rate and applied voltage became stronger. In our simulation, the air from the nozzle had a convergent profile because the flow rate of air from the nozzle was in subsonic range. The streamline was recorded at the outermost point of core and shell nozzles. In level-set laminar flow physics, the interface between the fluid and gas is described by a level-set parameter, which is dependent on the mesh size.[257] In order to analyze the properties within the interfacial area, we used the level-set method because it was known as efficient method for simulating two phase flow.[258] We set interface parameter to 100 μm to define the interface between melt and air. To observe changes in the jet thickness of sub-micron size, a smaller mesh size is necessary; however, it is impractical to select a very small mesh, due to computational costs and the small sizes of the nozzle and jet (millimeter and micrometer scales, respectively).[240] To resolve this problem, we estimated the shape of the ejected jet using the streamline defined by the moving fluids. In this study, the jet thickness was defined as the thickness of the streamline at 5 mm from the nozzle tip, which is 25-fold greater than the diameter of the core nozzle; at this distance, stable jet formation without whipping was assumed.[14] A thinner jet thickness formed when a higher voltage and air flow was applied. In this case, the stability of the jet was evaluated by analyzing the stress acting on the jet.

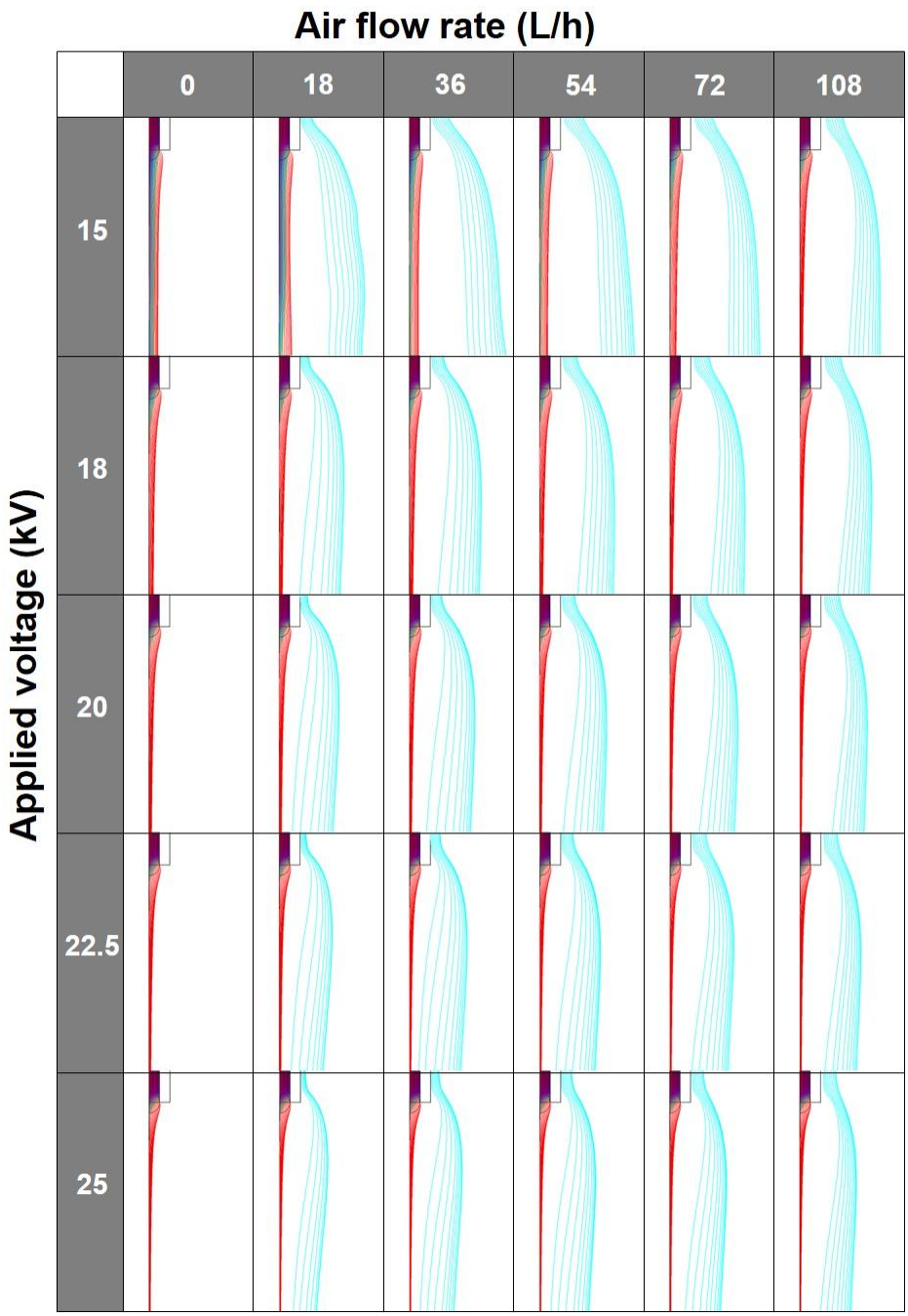

Figure 2-6 Volume fractions and streamlines of fluids after forming a stable jet according to the applied voltage (vertical) and air flow rate (horizontal). Inner (red) and outer (light blue) lines correspond to polymer melt and hot air flow, respectively.

Shear viscous stress is regarded as the force that acts tangentially on the surface of the fluid, causing jet sharpening. Moreover, shear viscous stress is defined as the force acting on the melt up to a region 0.5 mm away from the nozzle tip divided by the interfacial area of the melt. Using the viscous stress tensor ($\boldsymbol{\sigma}$) and the interface normal vector (**n**), the shear viscous stress, σ_s, is given by

$$\boldsymbol{\sigma}_s = \boldsymbol{\sigma} \cdot \mathbf{n} - \mathbf{n}\left(\mathbf{n} \cdot \left(\boldsymbol{\sigma} \cdot \mathbf{n}\right)\right) \qquad (1)$$

The magnitude of shear viscous stress shows different behaviors as the jet forms and begins to propagate (see **Figure 2-7** for the time-dependent shear viscous stress calculated at the end of Taylor cone). In the jet formation stage, the stress increases to a critical level to form a Taylor cone due to accumulation of charges at the interface between polymer melt and air.[231] Subsequently, the stress is released due to sharpening of the polymer melt by electric stress and drag force. In the propagation stage, the thin jet is stably ejected from the Taylor cone, and the magnitude of shear viscous stress is maintained. This tendency was observed for all process conditions employed in this study. Here, we presumed that a stable jet formed where the magnitude of viscous stress was maintained. The time required for stable jet formation decreased as the applied voltage increased, due to large electric stress. A schematic diagram of jet formation and propagation is shown in **Figure 2-8**. The sharpening of the fluids indicates the jet formation while the ejection of thinner fluid flow indicates the jet propagation. Up to 0.8 second at given condition the sharpening of the jet occurred due to accumulation of electric charges at the interface. After sharpening, thin jet continuously propagated.

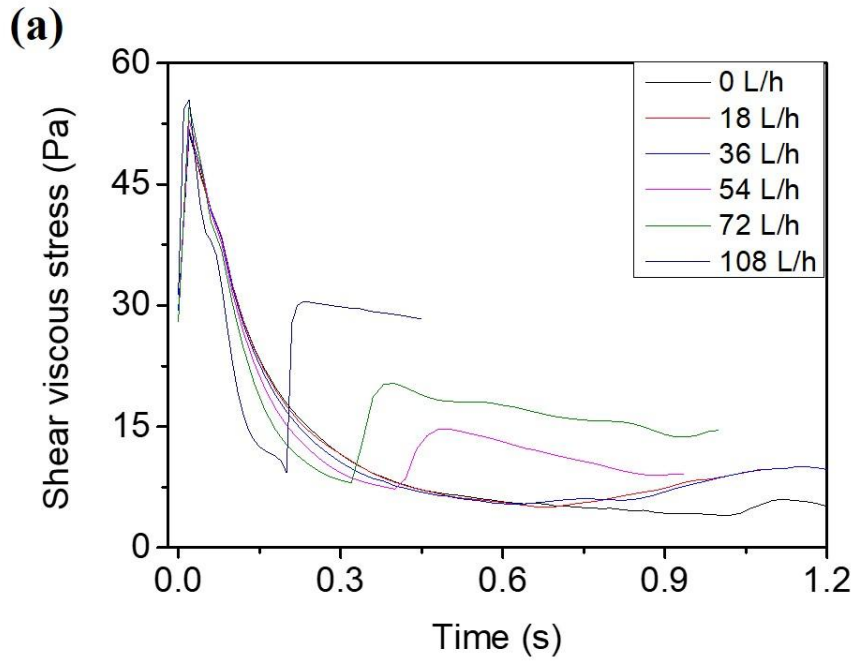
(a)
Shear viscous stress (Pa)
Time (s)
0 L/h
18 L/h
36 L/h
54 L/h
72 L/h
108 L/h
0
15
30
45
60
0.0
0.3
0.6
0.9
1.2

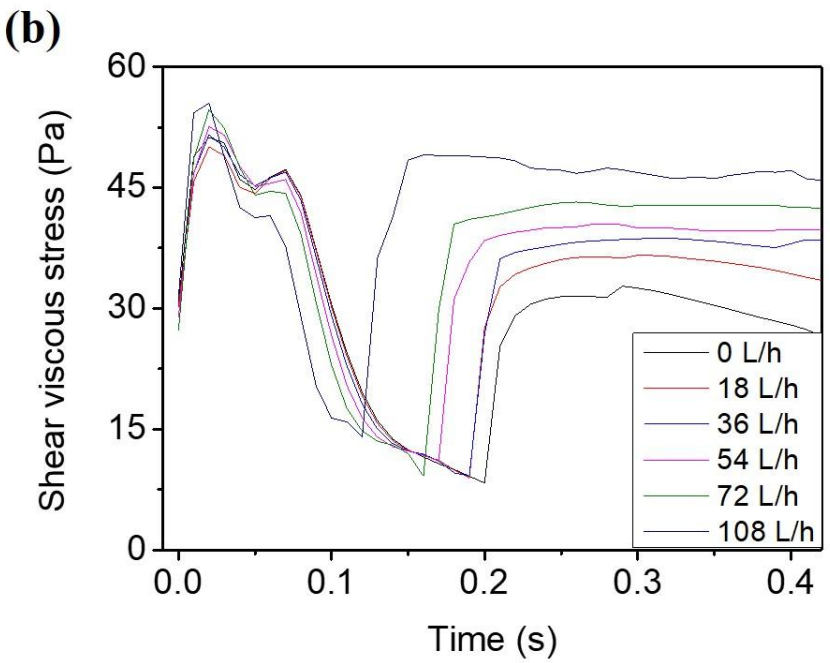
(b)
Shear viscous stress (Pa)
Time (s)
0 L/h
18 L/h
36 L/h
54 L/h
72 L/h
108 L/h
0
15
30
45
60
0.0
0.1
0.2
0.3
0.4

(c)

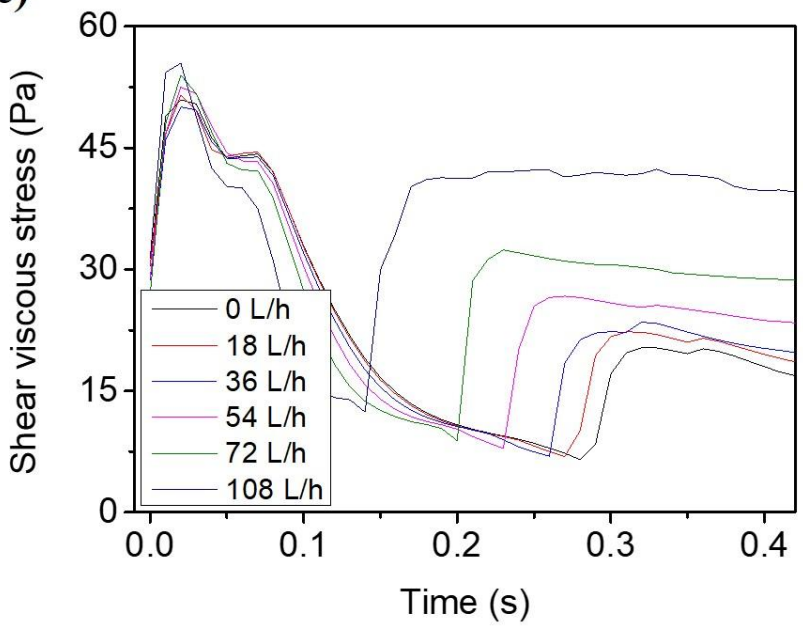
Shear viscous stress (Pa)
60
45
30
15
0
0.0
0.1
0.2
0.3
0.4
Time (s)
0 L/h
18 L/h
36 L/h
54 L/h
72 L/h
108 L/h

(d)

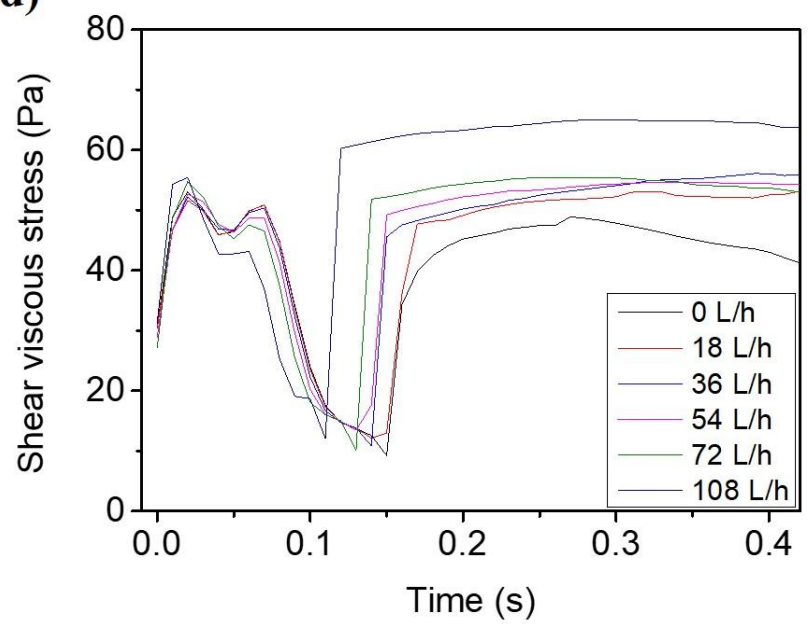
Shear viscous stress (Pa)
80
60
40
20
0
0.0
0.1
0.2
0.3
0.4
Time (s)
0 L/h
18 L/h
36 L/h
54 L/h
72 L/h
108 L/h

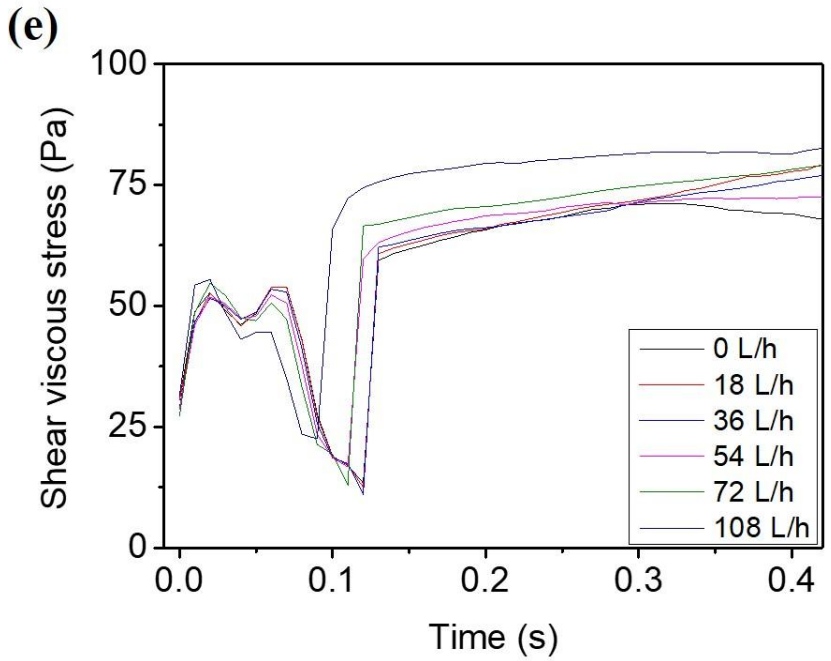

Figure 2-7 Parametric studies of shear viscous stress versus time during the GAME process, with applied voltages of (a) 15, (b) 18, (c) 20, (d) 22.5, and (e) 25 kV and different air flows.

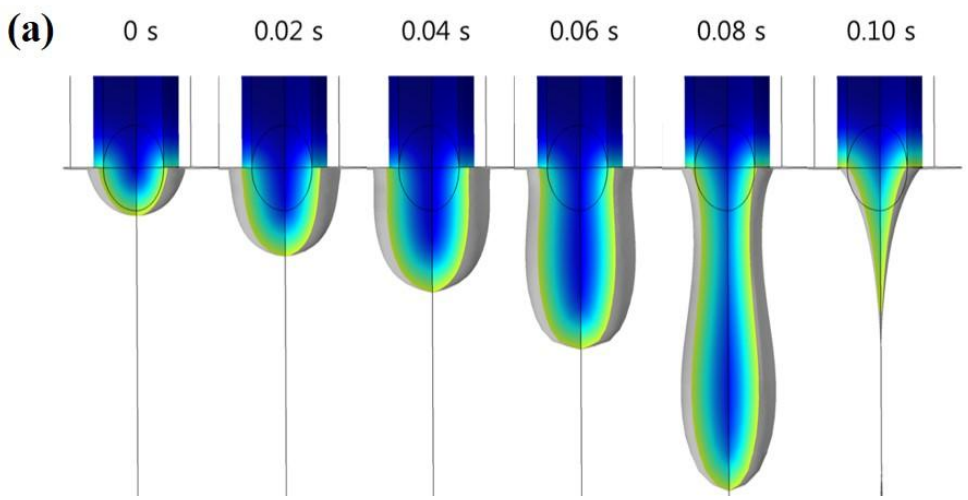

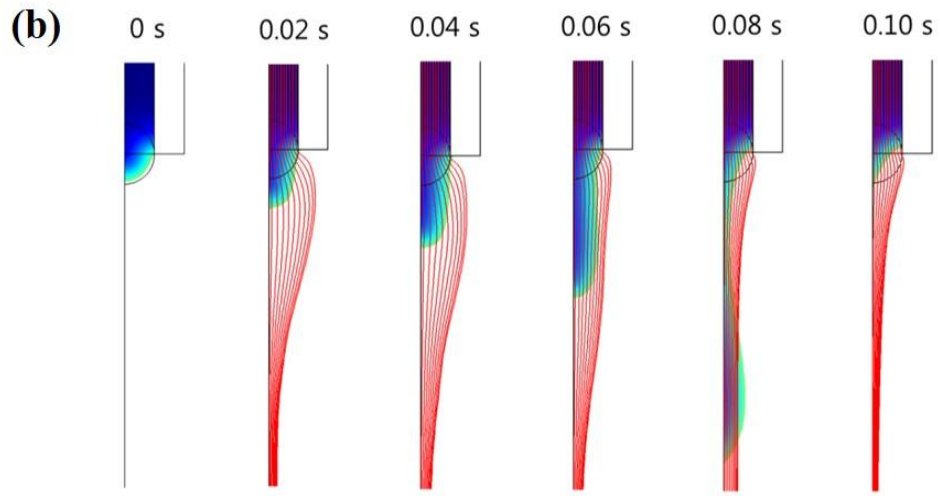

Figure 2-8 Simulation example of a single-nozzle GAME process at an applied voltage of 25 kV and an air flow rate of 72 L/h. (a) Volume fraction of the polymer melt and (b) streamline of the jet from the outer end of the core nozzle.

Next, we examined the relationship between the magnitude of shear viscous stress and jet thickness; specifically, we investigated the jet stretch ratio and voltage for stable jet formation (**Figure 2-9)**. The shear viscous stress at the end of the Taylor cone tended to increase with the applied voltage and air flow rate [**Figure 2-9**(a)]. Notably, the stress induced by air flow acted similarly to the stress affected by Maxwell stress within the range of processing conditions used in this study. Therefore, unlike the melt-blown or melt-electrospinning process, the GAME process provided additional stress for jet stretch via air flow. This relationship is described as follows:

$$\sigma_{Viscous} = \sigma_{Voltage} + \sigma_{Air}, \qquad \textbf{(2)}$$

$$\sigma_{Voltage} = A_{Voltage} * V - B_{Voltage}, \qquad \textbf{(3)}$$

$$\sigma_{Air} = A_{Air} * v_{Air}, \qquad (4)$$

where $\sigma_{Viscous}$, $\sigma_{Voltage}$, and σ_{Air} are the magnitude of total viscous surface stress and viscous stress due to the voltage and air flow, respectively. V is the applied voltage in kV and v_{Air} is the air flow rate in units of L/h. The coefficients $A_{Voltage}$, $B_{Voltage}$, and A_{Air} in our study were 7.29, 116.6, and 0.157, respectively. The stress and voltage showed a linear relationship, and the jet thickness was reduced as the total stress increased [**Figure 2-9(b) and (c)**]. As the stress at the interface increased, the jet stretch also increased [**Figure 2-9(d)**]; a sharp increase in the jet stretch ratio was observed for viscous stress values exceeding 30 Pa. Within this stress range, the ejected jet showed a mixed behavior of dripping and sharpening. Therefore, the stretch ratio became small [Figure 2-9(d)] and the time required for stable jet propagation increased significantly [Figure 2-6(a)] (average: 0.76 s; maximum time: 1.2 s). However, when the shear viscous stress reached a certain level, the forces on the liquid pendent overcame the surface tension and the inertia force completely, resulting in sharpening of the liquid instead of dripping. Here, we defined this stress as the critical viscous shear stress for the formation and propagation of a stable jet. This criterion reflects the results from the GAME experiments and other spinning processes that the straight jet in the stable jet region narrowed to a tenth of the radius of the nozzle tip by thinning (Figure 2-9(b)) and agreed with the experimental observation of polymer melts spinning and GAME process.[245] The relation between the jet thickness and distance from the nozzle tip is shown in **Figure 2-10**.

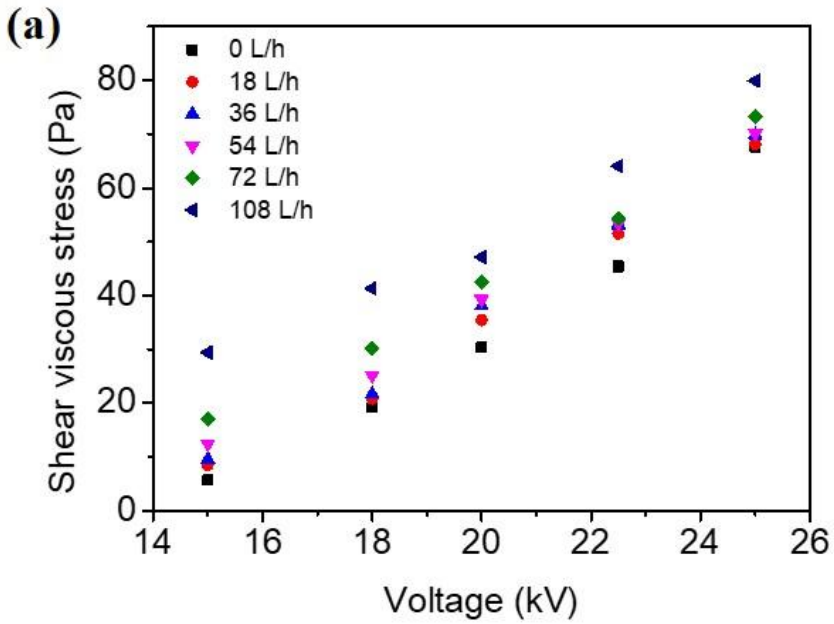
(a)
0 L/h
18 L/h
36 L/h
54 L/h
72 L/h
108 L/h
Shear viscous stress (Pa)
0
20
40
60
80
14
16
18
20
22
24
26
Voltage (kV)

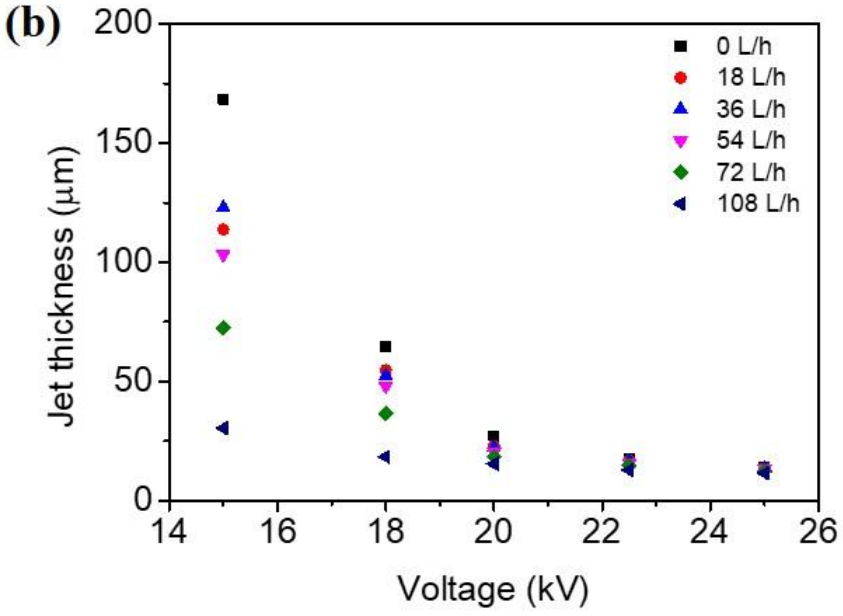
(b)
0 L/h
18 L/h
36 L/h
54 L/h
72 L/h
108 L/h
Jet thickness (μm)
0
50
100
150
200
14
16
18
20
22
24
26
Voltage (kV)

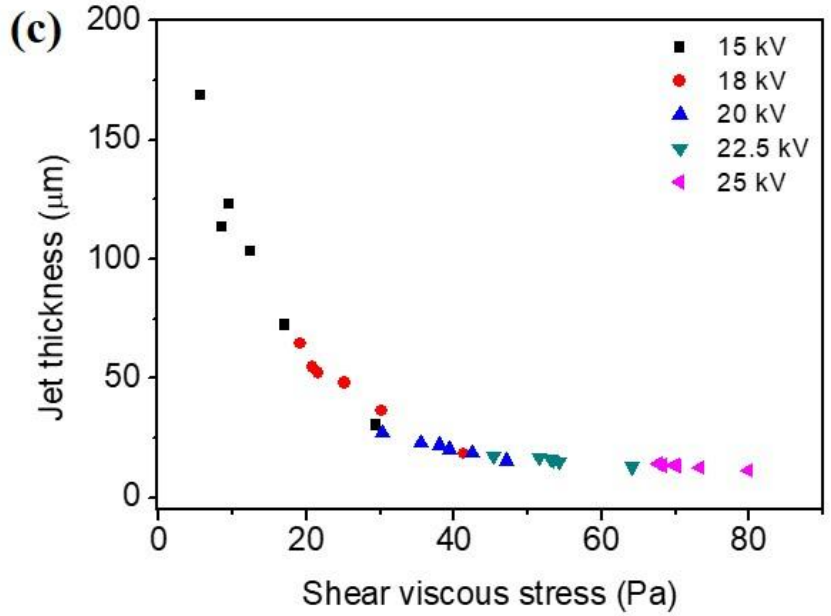

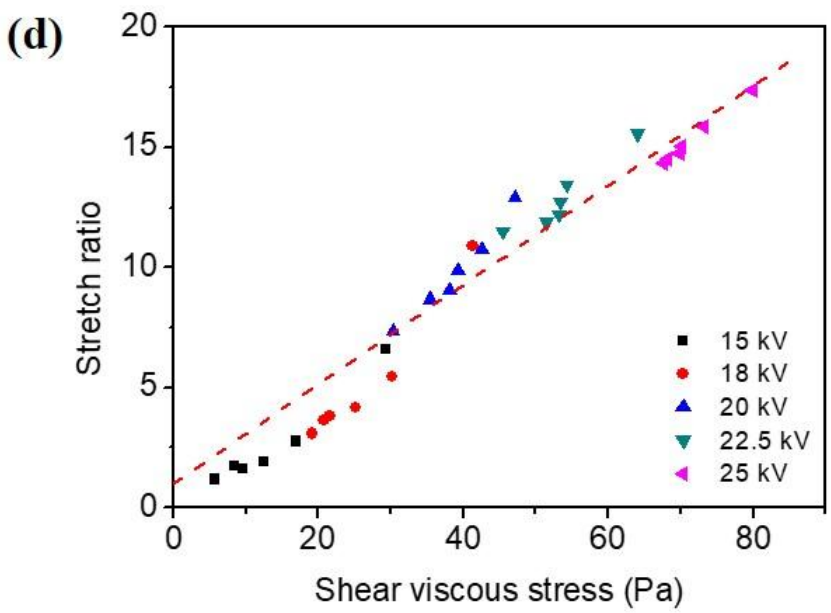

Figure 2-9 Simulated relationships of voltage, shear viscous stress, jet thickness, and jet stretch during stable jet propagation: (a) shear viscous stress–voltage, (b) jet thickness–voltage, (c) jet thickness–shear viscous stress, and (d) jet stretch–shear viscous stress.

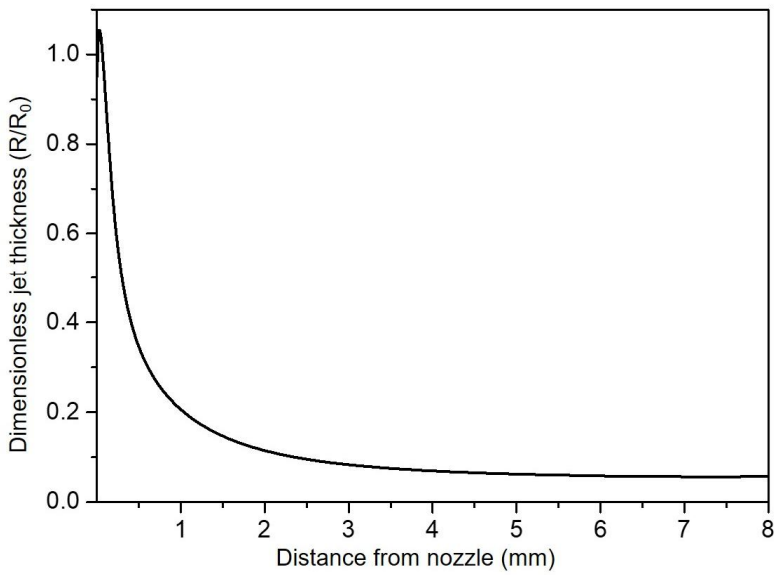

Figure 2-10 Dimensionless jet thickness according to distance from nozzle when applied voltage: 25kV and air flow rate 72 L/h.

2.3.2. Simulation of multi-nozzle GAME process

Considering the results presented thus far, we concluded that the electric field strength is crucial for good spinnability, particularly jet formation. The electric field strength varied with the process parameters in the multi-nozzle system. Therefore, the electric field distribution was calculated by varying the processing parameters (number of nozzles, tip-to-tip distance, and applied voltage) (see sections **2.2.3** and **2.2.4**). According to the configuration of the multi-nozzle system, the electric field strength was evaluated at the end of the Taylor cone. The field strength decreased with an increase in the number of nozzles and the tip-to-tip distance and increased

linearly with the applied voltage [**Figure 2-11(a–c)**]. Based on this strength in **Figure 2-11(d)**, a "spinnability diagram" was proposed [**Figure 2-11(e)**]. The diagrams in Figure 2-11(d) and (e) offer the minimum conditions of the processing parameters for ensuring that the electric field strength satisfies the critical shear viscous stress for stable jet formation and propagation. This electric field strength is defined as the critical electric field strength. Because the critical shear viscous stress is dependent on the rheological and electrical properties of polymer melts, both critical shear viscous stress and critical electric field strength are also dependent on the material. For example, the dynamic viscosity and electric permittivity of the polypropylene polymer melt used in this study were 4.6 Pa·s and 2.04 F m^{-1} at 523 K, respectively; its critical shear stress and electric field strength were 30 Pa and 15 kV/mm, respectively. The spinnability diagram in Figure 2-11(e) represents the voltage required for stable spinnability, according to the process parameters, including the number of nozzles and the distance between nozzles. Therefore, this diagram is useful for estimating parameters of large-scale systems. For example, for a hexagonal array of multi-nozzles with an auxiliary electrode (consisting of 200 nozzles with a 5-mm distance between nozzles), the minimum voltage required for good spinnability is estimated to be 45 kV. A diagram for a free electrode system is provided in **Figure 2-12**.

(a)

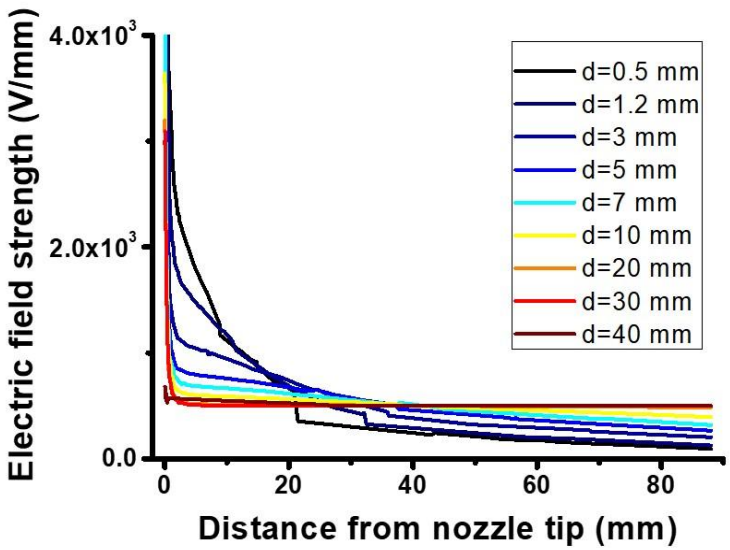
Electric field strength (V/mm)
4.0x10^3
2.0x10^3
0.0
0
20
40
60
80
Distance from nozzle tip (mm)
d=0.5 mm
d=1.2 mm
d=3 mm
d=5 mm
d=7 mm
d=10 mm
d=20 mm
d=30 mm
d=40 mm

(b)

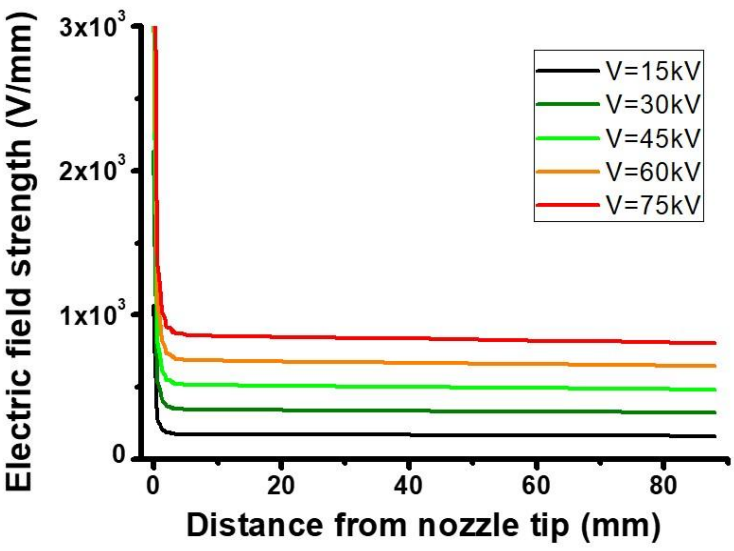
Electric field strength (V/mm)
3x10^3
2x10^3
1x10^3
0
0
20
40
60
80
Distance from nozzle tip (mm)
V=15kV
V=30kV
V=45kV
V=60kV
V=75kV

(c)

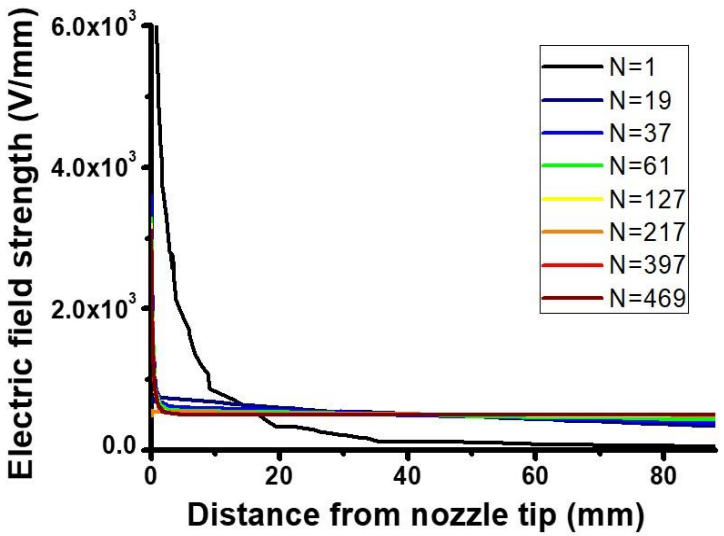
Electric field strength (V/mm)
6.0x10^3
4.0x10^3
2.0x10^3
0.0
0
20
40
60
80
Distance from nozzle tip (mm)
N=1
N=19
N=37
N=61
N=127
N=217
N=397
N=469

(d)

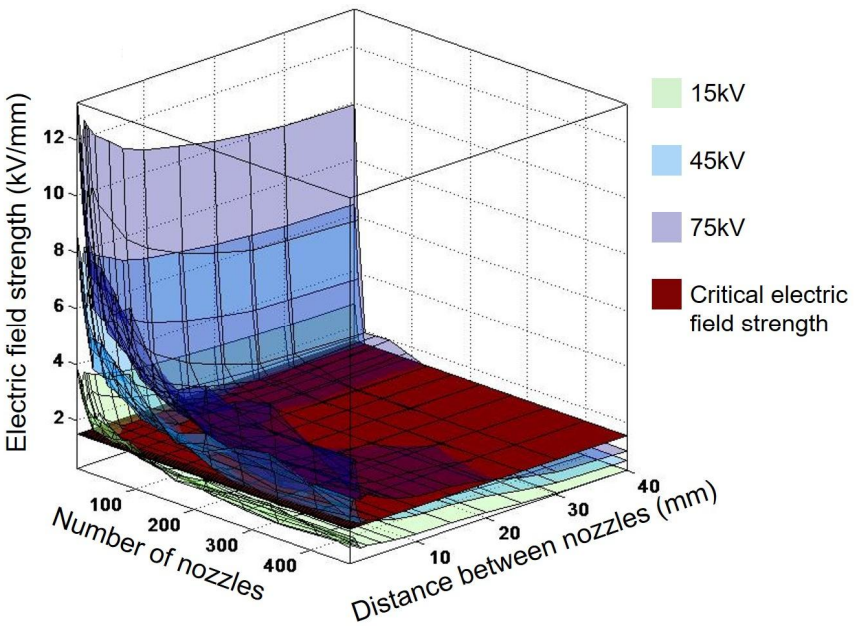
Electric field strength (kV/mm)
12
10
8
6
4
2
100
200
300
400
Number of nozzles
10
20
30
40
Distance between nozzles (mm)
15kV
45kV
75kV
Critical electric field strength

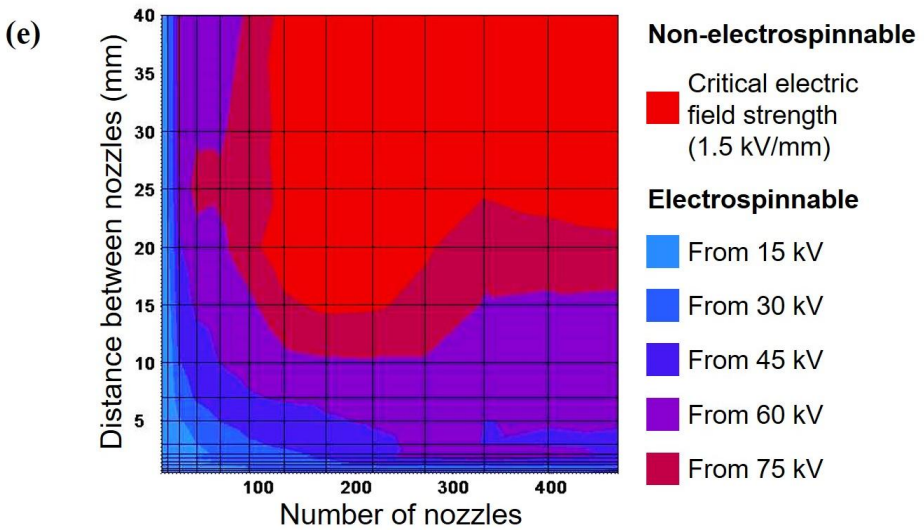

Figure 2-11 Electric field strength of the multi-nozzle system according to (a) the number of nozzles, (b) tip-to-tip distance, and (c) applied voltage. Horizontal axis indicates vertical distance from the nozzle tip. (d) Distribution of the electric field strength and (e) spinnability diagram indicating the minimum value of the applied voltage according to the process parameters of GAME (critical electric field strength: 1.5 kV/mm).

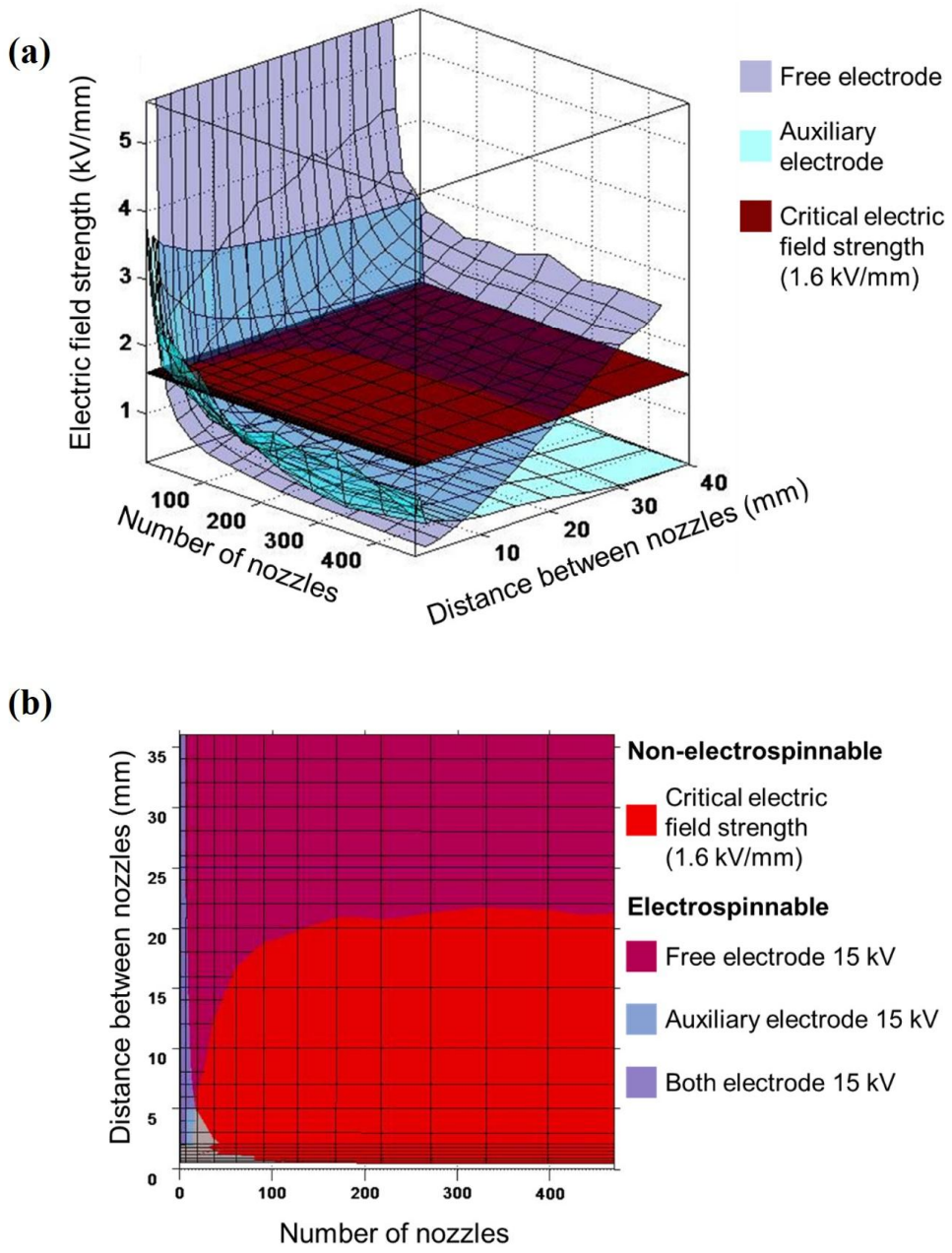

Figure 2-12 (a) Spinnability diagram of the GAME system with a free electrode. (b) Comparison of spinnability between an auxiliary electrode system and a free electrode system.

To validate the spinnability diagram, arbitrary processing conditions were simulated (**Figure 2-13)**. The results showed that a higher voltage was required for stable jet propagation at the same tip-to-tip distance with an increasing number of nozzles. In addition, a larger force was required to satisfy the spinnability criterion and promote jet sharpening. For example, for 19- and 37-nozzle systems with 5-mm spacing, voltages of 30 and 45 kV are required for stable spinning, as shown in the spinnability diagram of **Figure 2-11**(e). As discussed earlier, this prediction depends on the change in the critical electric field strength, which can be affected by various factors such as the properties of the material (e.g., viscosity, molecular weight, molecular structure, conductivity, and dielectric constant) and the processing parameters (e.g., nozzle diameter, liquid feed rate, and operating temperature). A spinnability diagram for different critical electric field strengths is shown in **Figure 2-14,** which can be used to design the appropriate processing conditions suitable for the given material.

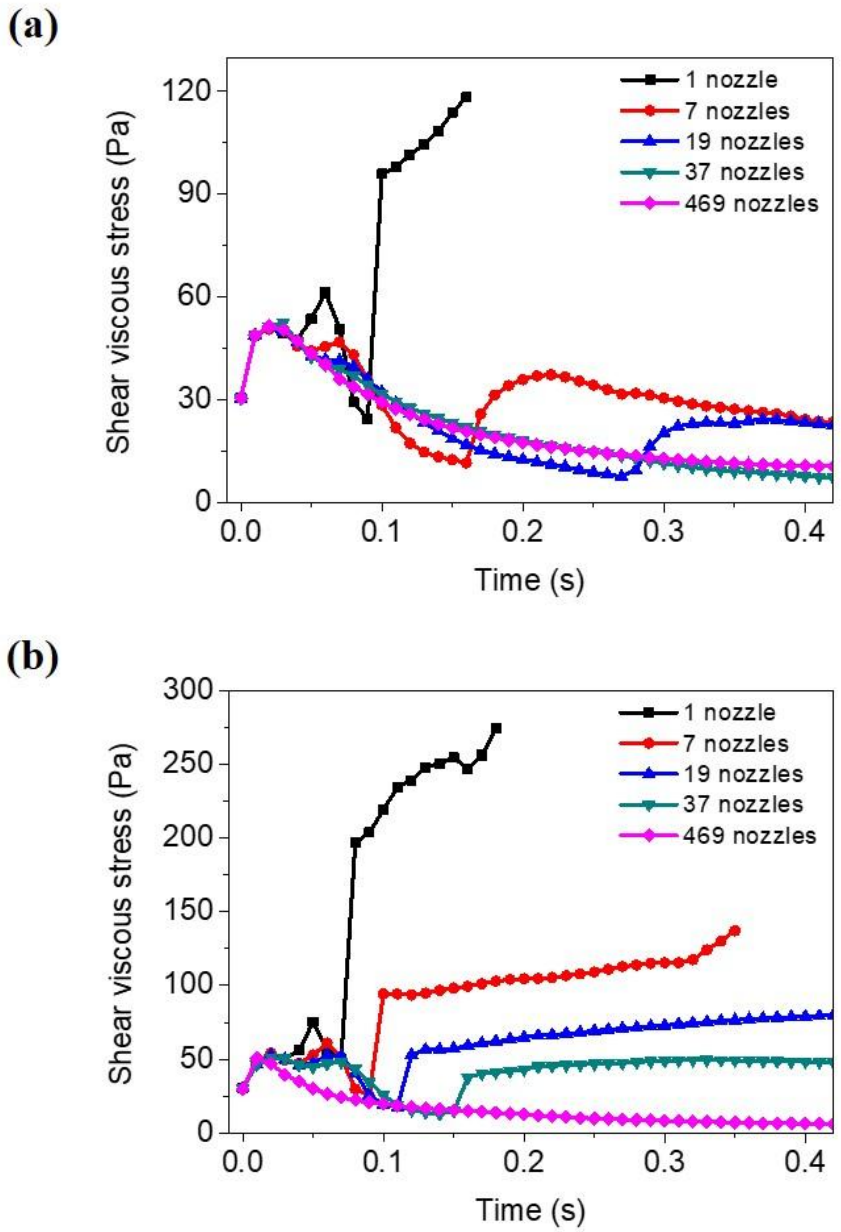

Figure 2-13 Shear viscous stress versus time during the multi-nozzle GAME process at a tip-to-tip distance of 5 mm and applied voltages of (a) 30 and (b) 45 kV.

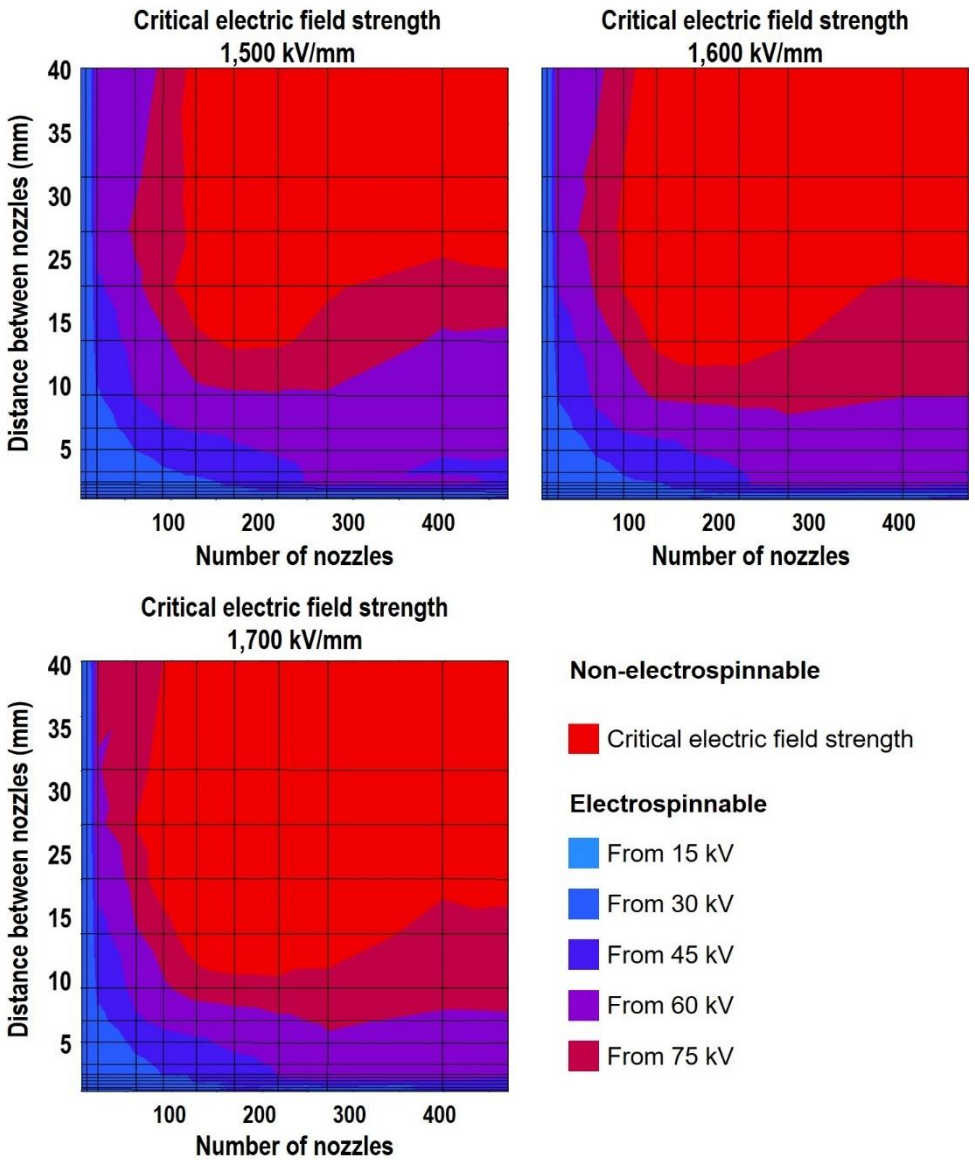

Figure 2-14 Two-dimensional spinnability diagrams of different GAME conditions for critical electric field strengths of (a) 1.5, (b) 1.6, and (c) 1.7 kV/mm.

2.4. Summary

In this study, we developed a simulation model to promote industrial use of the GAME process, which combines the advantages of electrospinning and melt-blown spinning processes. Two criteria were proposed to predict the spinnability of the material through multi-physics simulations of spinning behavior. First, a critical shear viscous stress (30 Pa) for spinnability was defined by calculating the shear viscous stress on the jet surface. Second, the critical electric field strength was defined, which constitutes the electric field strength (1.5 kV/mm) at the end of the Taylor cone as the critical shear viscous stress develops. Based on these criteria, we proposed a spinnability diagram that shows the minimal conditions necessary for a successful multi-nozzle GAME process, thereby providing a reasonable basis for GAME use at the manufacturing scale.

Chapter 3. Fabrication of inherently helical structure nanofibers

3.1. Needs for fabrication of helical nanofibers

Helical structures are common natural motifs, ranging from millimeter-sized plant tendrils [259] and micro-sized bacteria [260] to nano-sized biomolecules.[261] While helical structures have a variety of properties, one of the main advantages is the spring-like shape that allows for large elastic deformation, even with high strength materials.[262] Nanofibers have a variety of physical and chemical properties due to their thin size and large surface area. Previous studies in biomimicry have combined the optimal characteristics of nanofibers and helical structures [262, 263] to produce materials with enhanced functional and mechanical properties.

Electrospinning an efficient and simple process for making micro/nano-fibers and is commonly used to make helical fibers.[206, 264] The fabrication of helical nanofibers via electrospinning generally involves impingement, twisting, or asymmetric contraction.[265] Helical structures can emerge from impingement between the viscous electrospun fluid and the collector, as described by Taylor.[266] This phenomenon occurs via longitudinal compression of the viscous fluid as it collides perpendicularly with the collector plate.[267] Therefore, impingement is not related to bending instabilities during propagation of the electrified jet.[268] The

impingement method can be used to synthesize various patterns, including spiral, helical, sinuous, and zigzag-like structures, by controlling the process parameters such as applied voltage, angle, and motion of the collector(s).[269] However, the electrospun solution must have sufficient stiffness so as to sustain longitudinal compression.[49]. Therefore, the concentration and viscosity of the solution should be relatively high, resulting in thick polymeric fibers.

Helical structures can also be manufactured by twisting with an external force, *e.g.*, by rotation of the collector or electric field.[270, 271] The helical structure is then determined by the force exerted on the material, where one end of the fiber is fixed and the other can move to form a helix. The external force moves the free end and results in a twisted shape, such as a microrope.[272] Although not generally suitable for large-area applications or mass production, twisting in an effective method of fabricating helical fibers in a controlled manner and is easily applied to many nanoscience processes.

Asymmetric contraction can also be used to manufacture helical structures. Uneven stresses on the fiber increases instability and can result in a helical shape.[265] This can be accomplished by co-electrospinning two different solutions [273] and the effect can be enhanced by using an asymmetric configuration, such as off-centered or side-by-side spinnerets, instead of the more conventional concentric spinneret.[264] However, a mechanism for the formation of helical fibers in this way has not been proposed and the effect has only been observed with a limited number of materials.

Intrinsic curvature or initial twisting have been observed when helical fibers were produced in previous studies,[259, 274] suggesting that the position at which the jet solidifies can be considered a crucial factor in the formation of helical structures. We investigated the formation of helical nanofibers, focusing on the solidification behavior of an electrospun jet. We conducted two sets of experimental and simulated studies. The first experiment was conducted using dielectric polymer solutions with different solvent compositions to vary the vapor pressure, and then we observed changes in fiber morphology as a function of solvent evaporation rate. We also intentionally reduced the thickness of the jet to promote solvent evaporation at the jet surface; for this, we used a conductive fluid containing a high concentration of metal ions to produce a very thin jet during the early stages of the electrospinning process.

3.2. Experimental

3.2.1. Preparation of dielectric solution for helical nanofibers

Thermoplastic polyurethane (TPU, NEOTHANE 507APTM, Dongsung Co., Korea), N,N-dimethylformamide (DMF, Daejung Chemicals, Korea), and tetrahydrofuran (THF, Aldrich, US) were used as received for electrospinning. To vary the vapor pressure of the solution, 15 wt% TPU was dissolved in DMF and used to create 3:1, 2:1, and 1:1 weight ratios of DMF:THF.

3.2.2. Preparation of conductive solution for helical nanofibers

Polyvinylpyrrolidone (PVP, MW 1,300,000, Aldrich, US), poly(ethylene oxide) (PEO, MW 400,000, Aldrich, US), acetonitrile (ACN, anhydrous, Aldrich, US), and silver nitrate (99%, Daejung Chemicals, Korea) were used as received for electrospinning. PVP (810 mg) and PEO (310 mg) were dissolved in 10 g of ACN and stirred overnight. Next, 3.33 g of silver nitrate were added and mixed for 30 min. Throughout the electrospinning process, the flow rate was 1.0 mL/h, the tip-to-collector distance was 20 cm, and the fibers were collected on a grounded plate collector. The applied voltage was 25 kV for the TPU-based solutions and 18 kV for the PVP-based solutions.

3.2.3. Electrospinning and spinneret geometry

Spinnerets made of conductive or metallic material acted as an electrode and an inlet for the electrospinning solution. The geometries of the spinnerets were concentric and off-centered, a common configuration for co-electrospinning. A single fluid was electrospun through the core spinneret while the shell spinneret acted as an auxiliary electrode to create an uneven electric field distribution. An image of the spinneret configuration is shown in **Figure 3-1**.

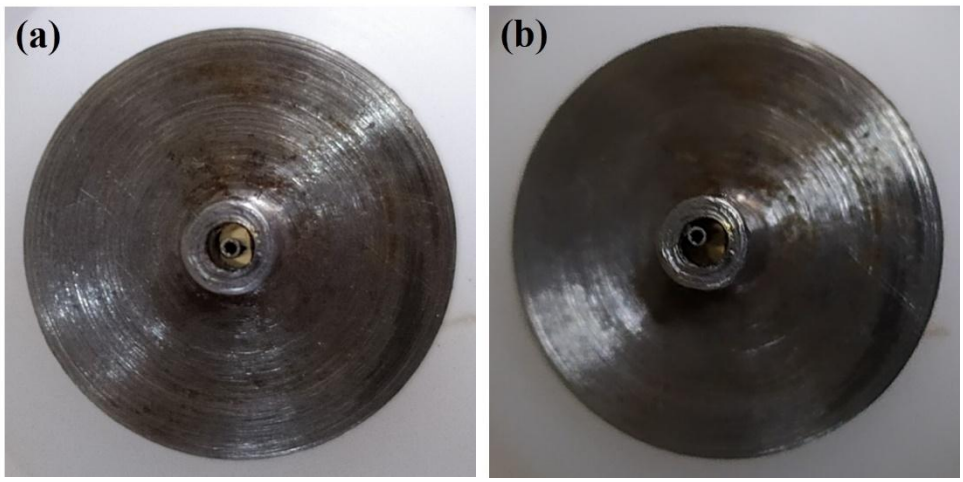

Figure 3-1 Geometry of electrospinning spinneret. (a) Concentric and (b) off-centered spinneret.

3.2.4. Characterization of Electrospun Fibers

Optical microscopy (BX51; Olympus, Japan) and field-emission scanning electron microscopy (JEOL JSM-7600F, Japan) were used to observe the structure and diameter of the electrospun fibers. Fibers were collected from 3 cm to 20 cm away from the spinneret. Images were obtained using an optical microscope (FXC500DE; FXC, Korea) near the spinneret in order to observe jet propagation. The viscosity of each electrospun solution was measured using a rheometer (AR2000, TA Instrument, US).

3.3. Results and discussion

3.3.1. Effect of solvent vapor pressure on structure

Mixtures of DMF and THF with different weight ratios were used to evaluate the effects of solvent vapor pressure on the morphology of electrospun TPU fibers. The vapor pressures of DMF and THF are 0.3 kPa and 19.3 kPa at 20°C, respectively.[275] The electrospun jet exhibited intrinsic curvature as observed previously.[262, 264]

Figure 3-2 presents the diameters of electrospun fibers collected at different distances from the spinneret. We compared fiber diameters: the diameters of fibers fabricated at both low (DMF only) and high (1:1 DMF:THF) vapor pressure decreased with increasing distance from the spinneret. However, with the low vapor pressure system, slow evaporation resulted in a steady reduction in diameter as a function of collecting distance. In contrast, fast evaporation of the high vapor pressure system resulted in fiber diameter decreasing to a stable value past a certain collector distance. This can be explained by the change of state and flight path of the jet. In general, the flight path of the jet increases with increasing collector distance.[276] However, the increase in flight path is not directly related to an increase in jet stretching.[277]

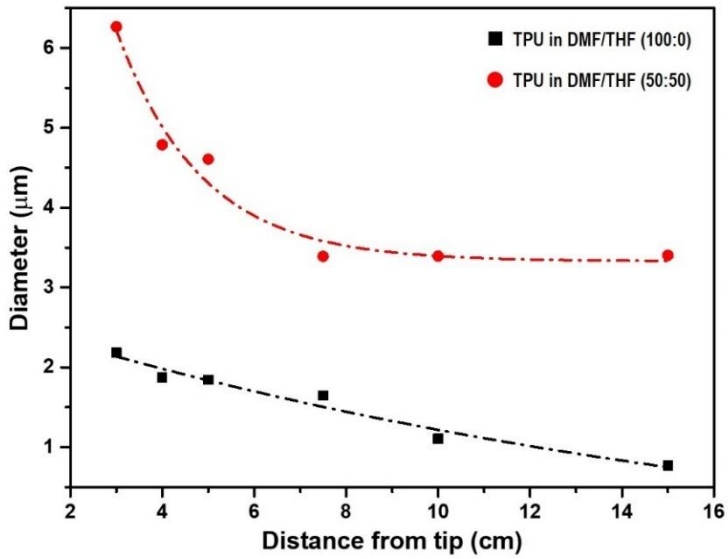

Figure 3-2 Diameters of electrospun TPU fibers collected at different distances from the spinneret tip.

If the charge carriers in the jet are maintained by adequate solvent, then the jet is subject to electrical forces during flight that can result in stretching [278]. In contrast, if the solvent evaporates rapidly, before the onset of bending instability, then the charge carrier becomes immobile and no further stretching occurs, regardless of flight distance.[279] Therefore, the distinctive behavior of the high vapor pressure jet in **Figure 3-2** indicates that solidification of the jet occurred in the early stages of electrospinning and hindered any further stretching of the jet during the whipping stage. **Figure 3-3** presents the morphologies of fibers obtained from electrospun liquids with different solvent compositions.

(a)

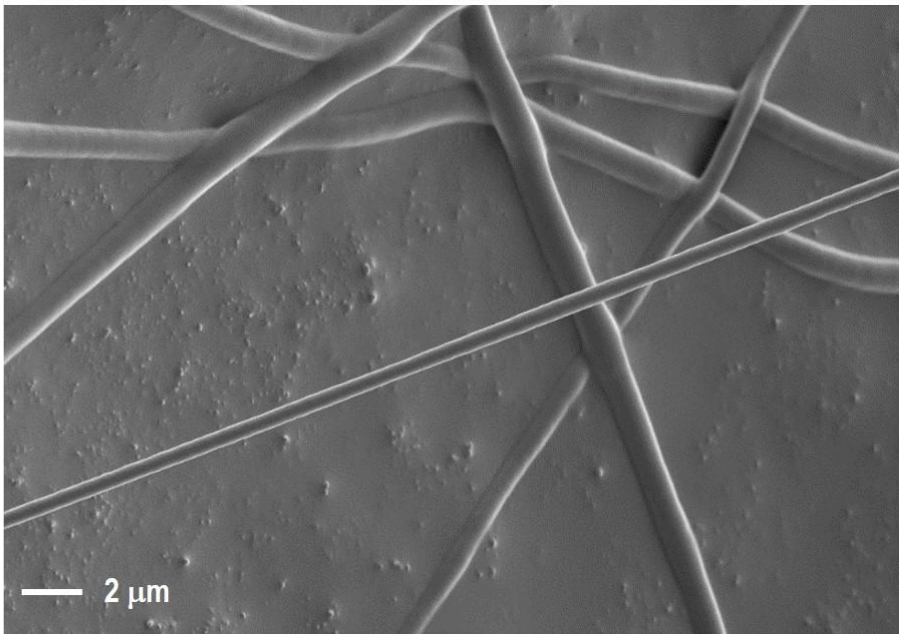

(b)

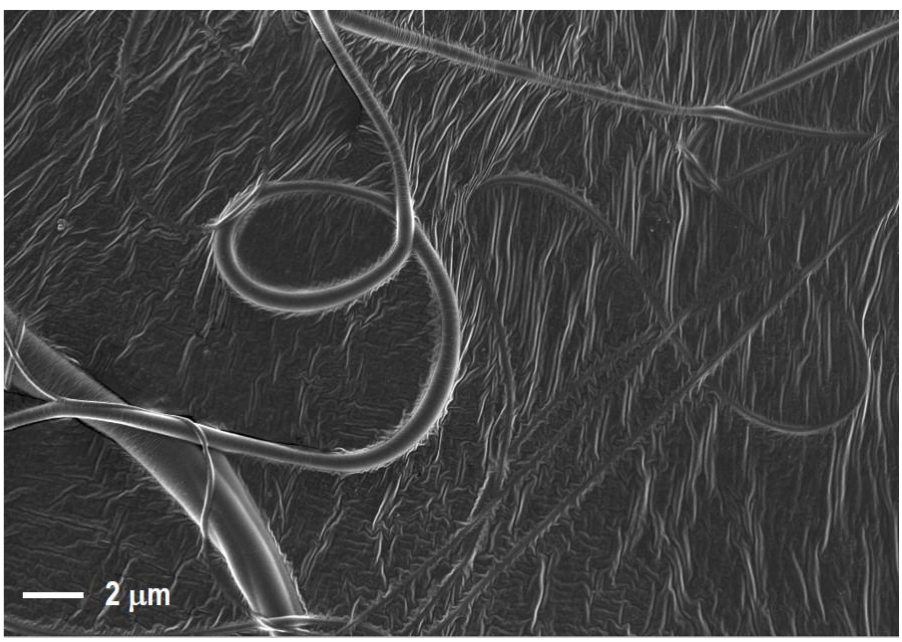

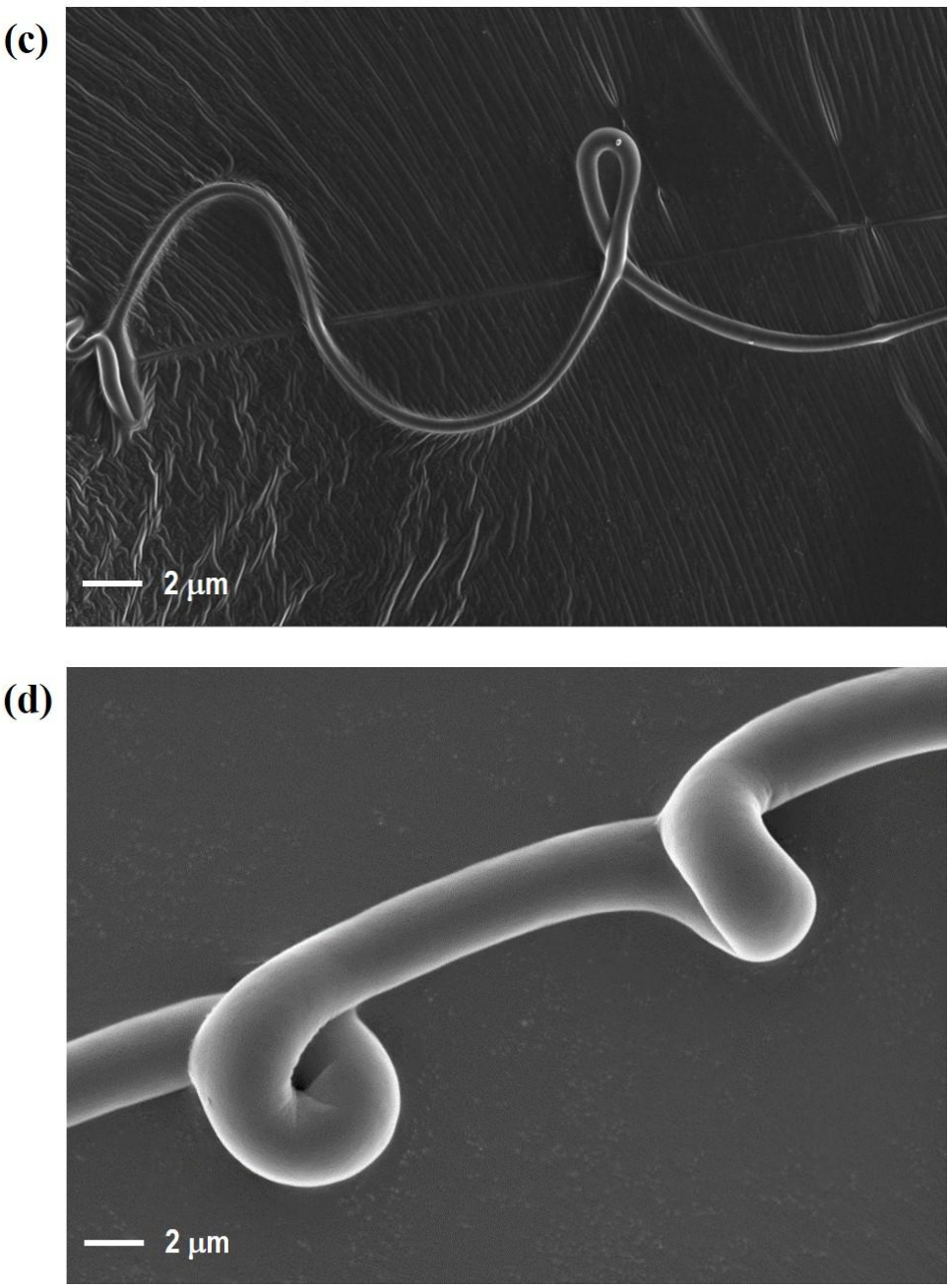

Figure 3-3 SEM micrographs of electrospun TPU fibers made with different solvents: (a) DMF, (b) DMF/THF (3:1), (c) DMF/THF (2:1), and (d) DMF/THF (1:1).

As shown in **Figure 3-2**, fiber diameter increased with increasing vapor pressure. However, the fibers also changed structurally from straight and thin to helical and thick. This can also be explained by rapid solidification of the jet during the early stages of electrospinning. In general, after onset of bending instability, the electrified jet stretches significantly depending on the solvent evaporation rate.[58, 279] If the evaporation rate is slow, then the surface charge accumulated at the jet interface can be maintained during stretching. In this case, the electrified jet undergoes continuously strong electrical stress, resulting in a high degree of stretching and a straight structure.[280] Conversely, rapid solidification results in less electrical stress and less stretching, and the intrinsic curved structure is maintained throughout the stable jet region. Furthermore, the rate of solidification decreases with surface charge.[281] As a result, whipping phenomena can be suppressed due to the reduction in flight path.[282] This was confirmed by a comparison of the areas of collected nanofibers mats generated from solutions with different solvent compositions. The diameters of the collected mats were 8.1 cm for DMF only and 3.1 cm for 1:1 (DMF:THF), representing decreases in both whipping angle and flight path (**Figure 3-4**).

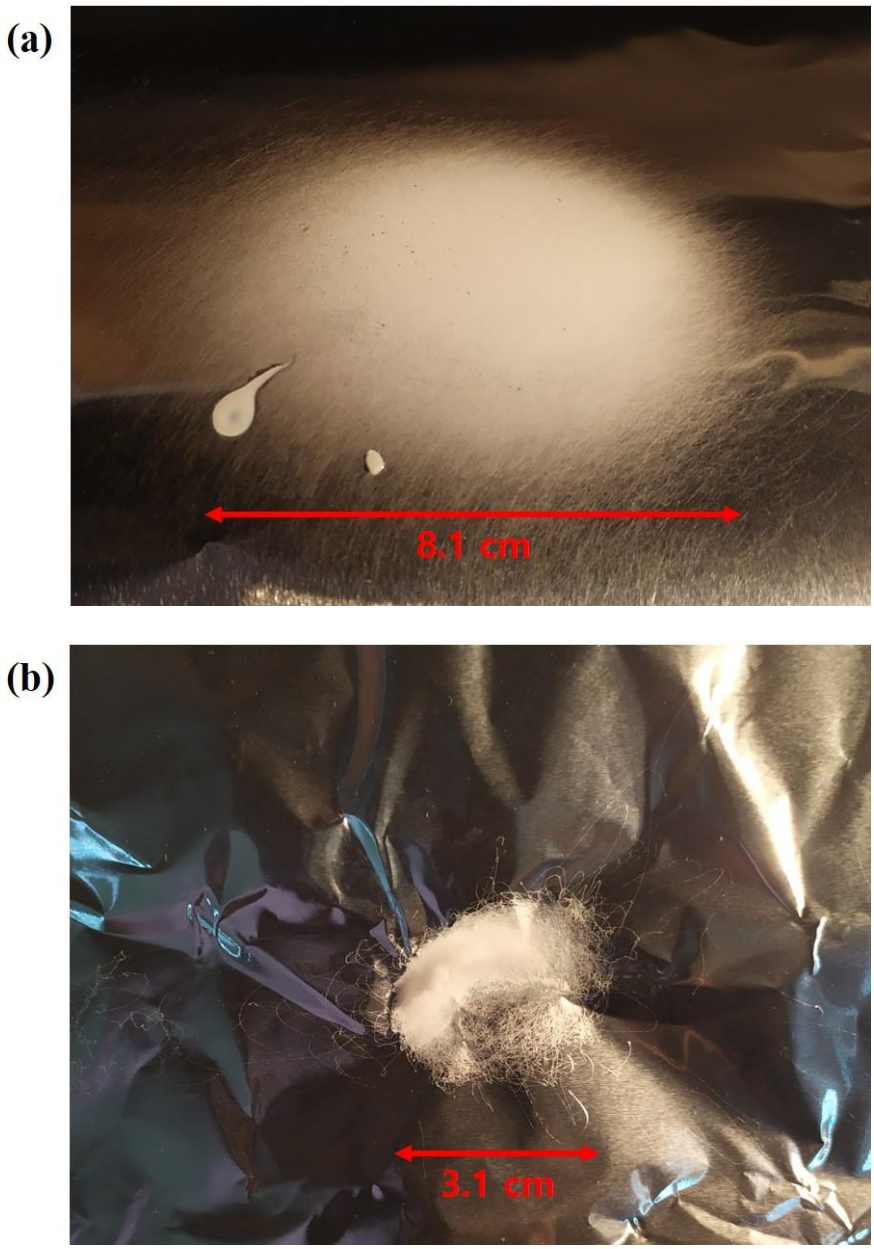

Figure 3-4 Images of collected TPU fiber mats according to solvent composition. (a) DMF. (b) 1/1 of DMF/THF (w/w).

Therefore, while the diameter of electrospun fibers is relatively thick when using a high vapor pressure solvent, a helical structure can result from the preservation of the intrinsic curvature of the jet via solidification. The SEM micrographs in **Figure 3-3** reveal that the pitch of the helical structure increases with increasing vapor pressure of the electrospun solution.

3.3.2. Effects of solidification on structure

We intentionally reduced the diameter of the ejected jet in order to enhance solvent evaporation at the surface, expecting that rapid solidification of the jet would occur in the straight jet region. Note that reducing the jet diameter has a similar effect on solidification as using a high vapor pressure solvent.[283] To facilitate rapid solidification of the jet in the stable jet region, we increased the electrical conductivity of the polymer solution by adding a large amount of silver nitrate (25 wt%), which increases electrical stress during electrospinning. Note that silver nitrate decomposes to silver ion in an acetonitrile-based polymer solution.

Figure 3-5 presents the diameters of electrospun fibers containing silver ion as a function of distance from the spinneret tip.

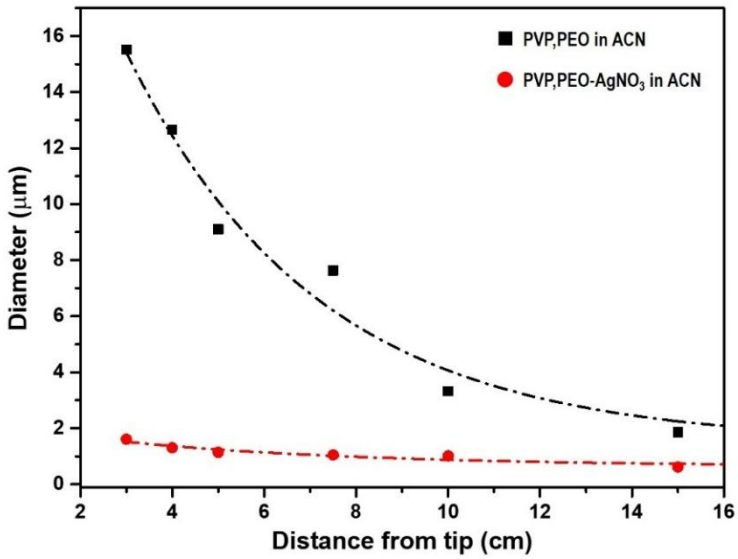

Figure 3-5 Diameters of electrospun fibers containing silver ion as a function of distance from the spinneret tip.

Electrospun fibers with and without silver ion exhibited different behaviors. The diameter of fibers containing silver ion changed relatively little with collector distance. In contrast, the mean diameter of fibers without silver ion decreased approximately eight-fold as the collector was moved further from the spinneret. **Figure 3-6** illustrates the behavior of the jet near the spinneret.

(a)

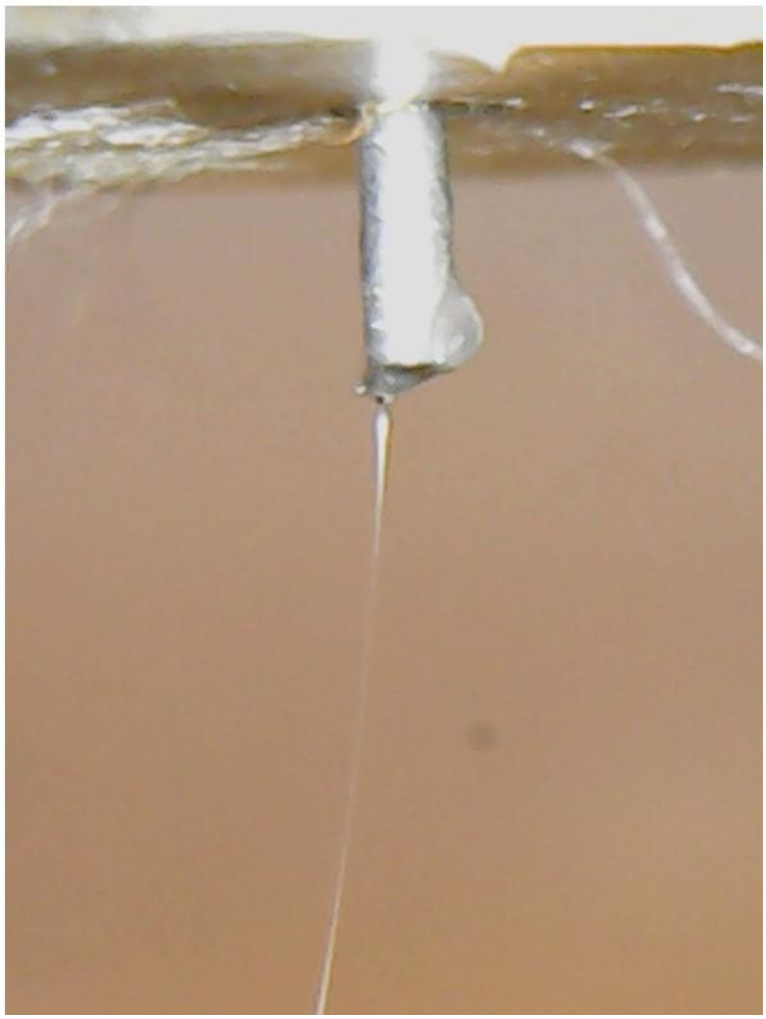

Figure 3-6 Microscopic images of ejected jet. (a) PVP,PEO in ACN and (b) PVP,PEO-$AgNO_3$ in ACN.

A Taylor cone and a long straight jet (~20 mm) are evident as is typical during electrospinning following bending and whipping. The jet containing silver nitrate had a much shorter straight jet (c.a. 1.2 mm) and did not exhibit whipping behavior. This finding suggests that the addition of silver nitrate induces strong electrical stress,

such that the electrified jet is subjected to a high degree of stretching at the initial stages of electrospinning, followed by solidification before 3 cm.

Figure 3-7 presents changes in the structures of electrospun fibers composed of mixtures of PEO and PVP with and without silver salt.

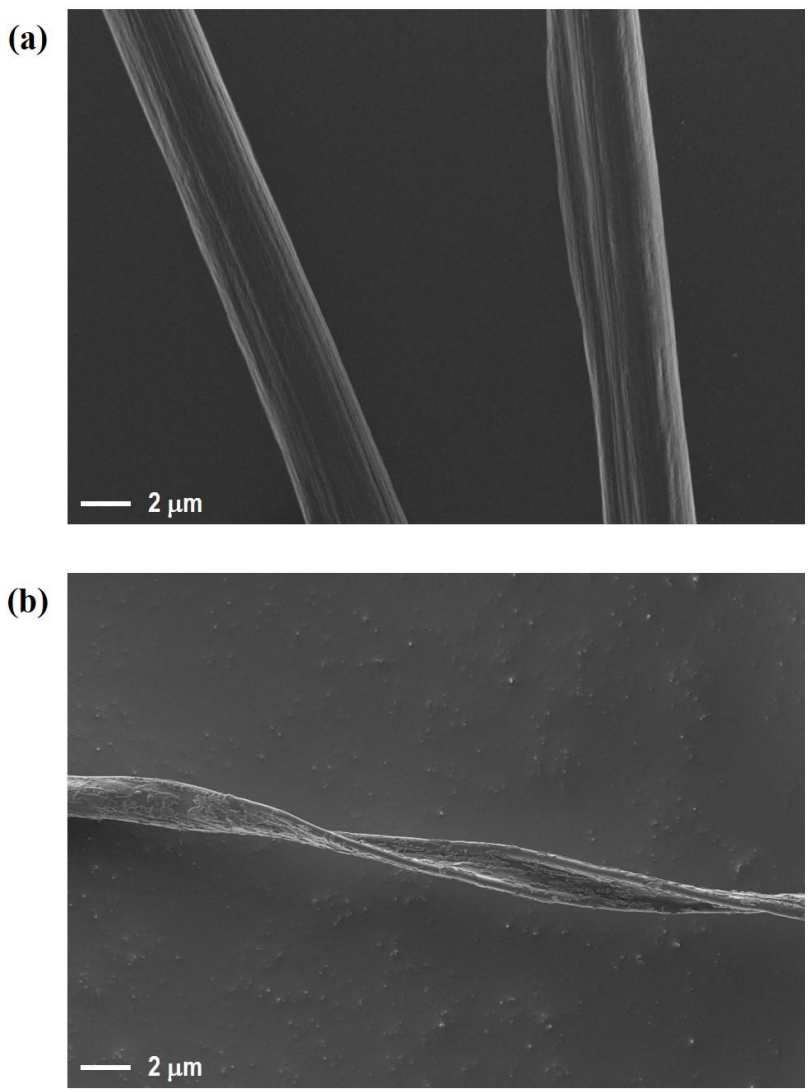

Figure 3-7 SEM image of electrospun PVP and PEO based polymer fibers. (a)

without silver ion and (b) with silver ion.

The increased electrical conductivity afforded by the silver nitrate resulted in electrical forces that reduced the diameter of the resulting fibers. Additionally, this effect changed the morphology of the fiber from straight to a twisted helical structure. The changes in morphology were due to rapid solidification of the jet near the nozzle tip. As shown in **Figure 3-5**, the diameter of the conductive jet changed little as a function of collecting distance, implying that solidification of the jet surface occurred within 3 cm of the nozzle tip. However, experimental observation of electrified jets near the tip of the spinneret is difficult. We therefore tried to evaluate jet propagation close to the electrode through electrospinning simulations using a highly conductive solution.

3.3.3. Numerical simulations of jet near nozzle

Numerical simulations were conducted using commercial COMSOL Multiphysics ® (5.2V) software. The electrospinning model was based on our previous work and incorporated a level set laminar two-phase flow and an electrostatic module to predict fluid motion and electric field distributions.[247] The simulations were designed to predict jet diameter near the spinneret tip as a function of solution conductivity. To simulate jet propagation with a highly conductive fluid, we implemented an electrical force at the liquid-gas interface.[284] The applied force includes the effects of free electrons from dielectric (polymer and solvent) materials

accumulated during process and ionic charges from the silver ions. We used a two-dimensional axisymmetric model; the geometry and boundary conditions are shown in **Figure 3-8** and detailed information about the models is provided in the appendix.

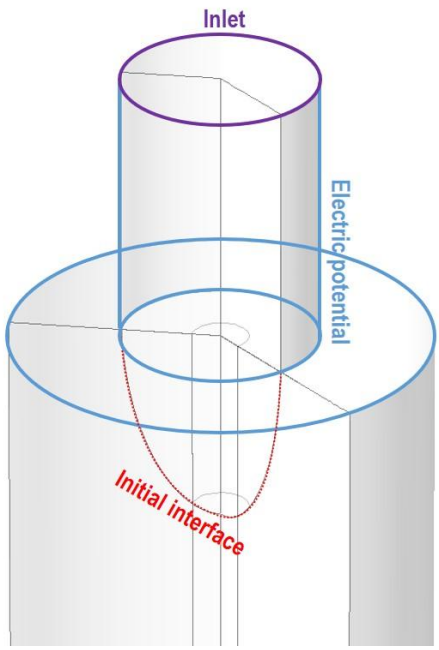

Figure 3-8 Model geometry and boundary condition of two-dimensional axisymmetric electrospinning model.

The electrical forces caused by the accumulation of free charges in the dielectric solution ($f_s^{E,d}$) and ionic charges ($f_s^{E,c}$) at the interface are defined as follows. The interface between the liquid and air was assumed to be conductive such that electrons can be exchanged through ions and the ion-polymer complex. The fast solidification process was assumed to show characteristics of both a solution and an electrospinning melt. Based on these assumptions, the force at the air interface of the

jet surface near the spinneret can be described by the following equations.[284]

$$f_s^{E,d} = \frac{\varepsilon_0}{2}\left(\frac{(D\cdot\mathbf{n})^2}{{\varepsilon_0}^2}\left(\frac{1}{\varepsilon_{polymer}}-\frac{1}{\varepsilon_{air}}\right)-(\mathbf{E}\cdot\mathbf{t})^2(\varepsilon_{polymer}-\varepsilon_{air})\right)\mathbf{n}\delta \qquad \textbf{(4)}$$

$$f_s^{E,c} = \frac{\varepsilon_0}{2}\left((\mathbf{J}\cdot\mathbf{n})^2\left(\frac{\varepsilon_{polymer}}{\sigma^2_{polymer}}-\frac{\varepsilon_{air}}{\sigma^2_{air}}\right)-(\mathbf{E}\cdot\mathbf{t})^2(\varepsilon_{polymer}-\varepsilon_{Air})\right)\mathbf{n}\delta$$

$$+\varepsilon_0(\mathbf{J}\cdot\mathbf{n})\left(\frac{\varepsilon_{polymer}}{\sigma_{polymer}}-\frac{\varepsilon_{air}}{\sigma_{air}}\right)(\mathbf{E}\cdot\mathbf{t})\mathbf{t}\delta \qquad \textbf{(5)}$$

These expressions include the surface force from induced free charges of displacement in the dielectric materials and Lorentz forces. The relaxation time for charges in the fluid is much shorter than that of molecular relaxation. This results in rapid charge accumulation at the surface of the jet. Furthermore, only charges at or near the surface can interact with the external electrical force. We implemented that force on an interface thickness, δ.[251, 252, 285] The conductivity of each solution was varied by adjusting its space charge density. The conductivity of ionic species was described as follows:

$$\rho_i K_i = K \qquad \textbf{(6)}$$

where K_i is ion mobility and ρ_i is the space charge density.[286] Silver nitrate at 25 wt% can be fully dissolved in acetonitrile. Therefore, the density of ions in solution was estimated as 1.5 mol L^{-1}, assuming perfect ionization. However, silver ions in solution are known to form ion clusters or metallopolymers with PVP and only a

small amount of the total charges are involved in electrical interactions. We therefore changed the charge density from a dielectric level of 10^{-5} to 10^{-1} C/m^3.[287-289] Using this model, we tried to simulate the behavior of the jet as a function of solution conductivity.

Figure 3-9 presents simulations of jet propagation near the spinneret tips using dielectric and conductive fluids.

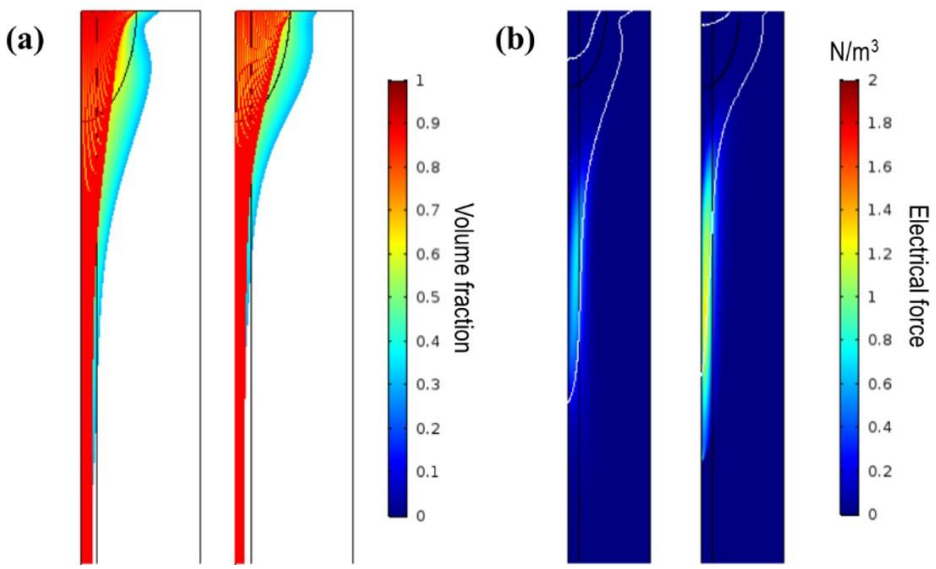

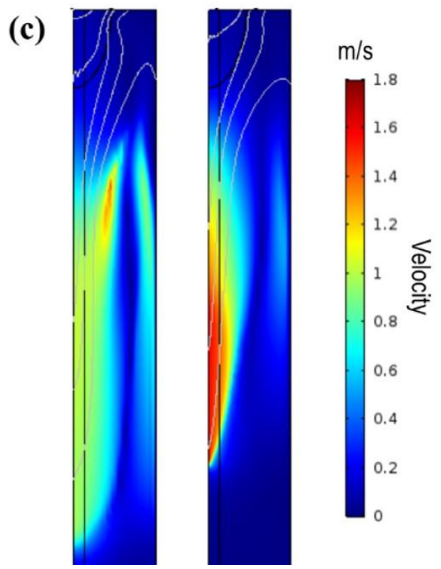

Figure 3-9 Simulations of electrospun dielectric (left) and conductive (right) fluids: comparisons of (a) volume fraction, (b) electrical force, and (c) velocity are provided after ejection of a stable jet.

Relatively small mesh sizes were required to estimate changes in jet radius down to the micron scale. Additionally, the level-set parameter that describes the liquid/gas interface is dependent on mesh size.[257] Unfortunately, small mesh sizes increase computational costs.[290] We therefore estimated jet morphologies using the streamline defined by the moving fluids. The jet diameter in the conductive case was smaller than that in the dielectric case (**Figure 3-9 (a)**) due to stronger surface electric forces (**Figure 3-9 (b)**). The transportation of charge occurs primarily by convection after ejection from the Taylor cone. The velocity of the jet also increased with increasing conductivity (**Figure 3-9 (c)**). Therefore, we were able to analyze changes in the diameter of the ejected jet by varying the charge density of the

polymer solution. **Figure 3-10** presents the predicted jet radius near the spinneret tip (within 5 mm).

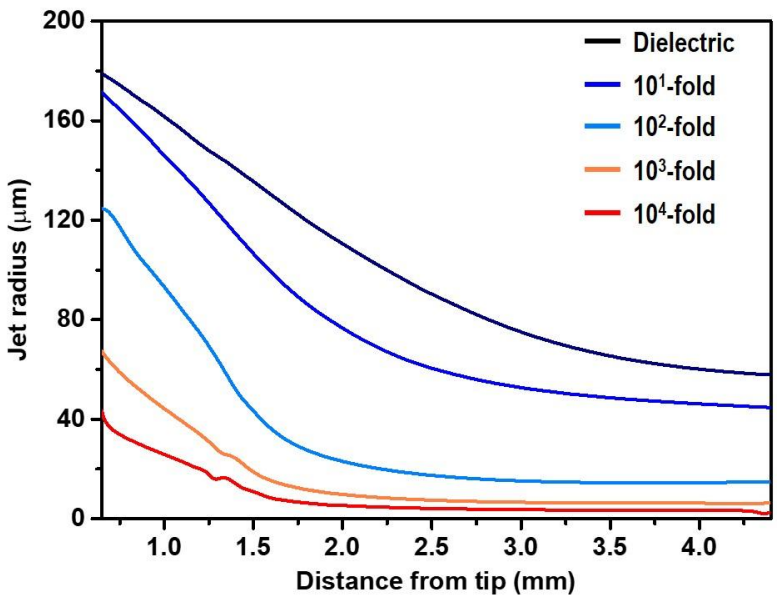

Figure 3-10 Predicted jet radius is shown as a function of surface charge density near the spinneret tip.

Charge density was varied from the dielectric level to 10^4-fold thereof. This is a reasonable range of charge densities, given previous calculations showing 0.2 C/m^2 for a dielectric to 2500 C/m^2 for a highly conductive material.[234, 247] Jet diameter decreased with increasing charge density in the solution due to increases in the number of charge carriers available to interact with the external electric field. The

rate of reduction in jet diameter was high near the spinneret tip and decreased with increasing distance. This finding is similar to those of previously reported studies. However, there are generally noticeable differences between the dielectric and conductive fluids in terms of jet radius.[291] Here, the dielectric jet radius decreased gradually, as shown in a previous TPU fiber experiment. However, the rate of radius reduction in the conductive jet decreased abruptly within about 2 mm. Although the simulation model did not include the effects of solvent evaporation, it did consider the basic rheological properties of fluids: viscosity and surface tension. Both jet stretching and the stretching ratio were affected by the rheological properties of the solution. As the jet elongates, the electric force decreases with decreasing charge density. The simulated data in the high charge density case fit well with the experimental data where the jet radius did not decrease significantly after an initial rapid stretching. This finding indicates that rapid solidification occurred during the early stages of the stable jet region.

3.3.4. Further enhanced helical structrues

Finally, we tried to enhance intrinsic fiber curvature or initial twisting using an uneven electric field distribution. We hypothesized that if solidification occurs rapidly within the straight jet region, then the proportion of helical fibers can be increased by enhancing the intrinsic curvature of the jet near the electrode. Therefore, we controlled the electric field distribution by using an asymmetric spinneret

geometry and analyzed the effects on fiber morphology. Concentric and off-centered spinnerets (**Figure 3-1**) can generate even and uneven electric field distributions, respectively. In a previous study, Wu *et al*. [53] used the same spinneret in a co-electrospinning process. Here, we employed single-fluid electrospinning using only the inner spinneret.

Figure 3-11 (a) and **(b)** present SEM micrographs of fibers electrospun from a highly conductive solution using the concentric and off-centered spinnerets, respectively.

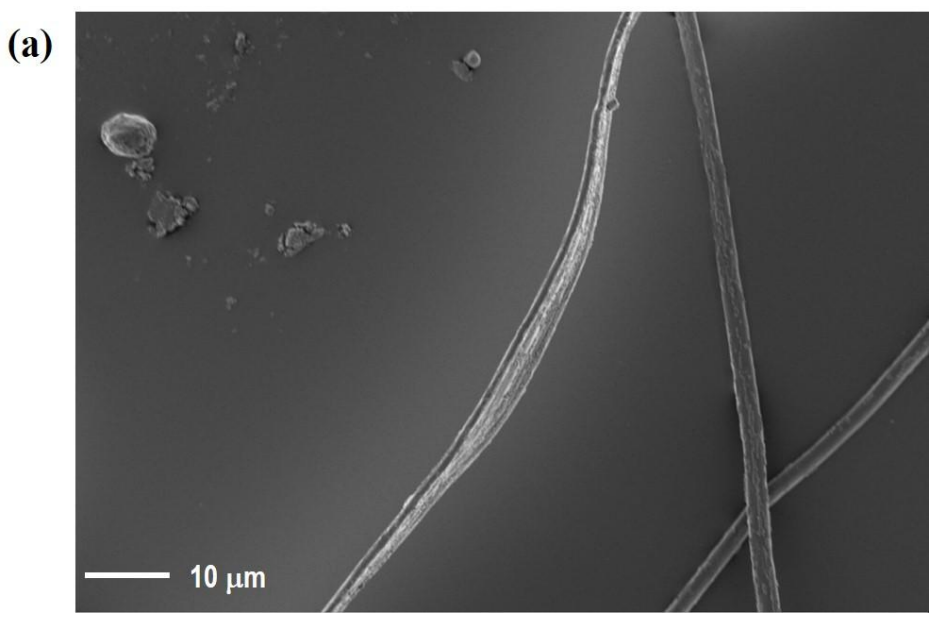

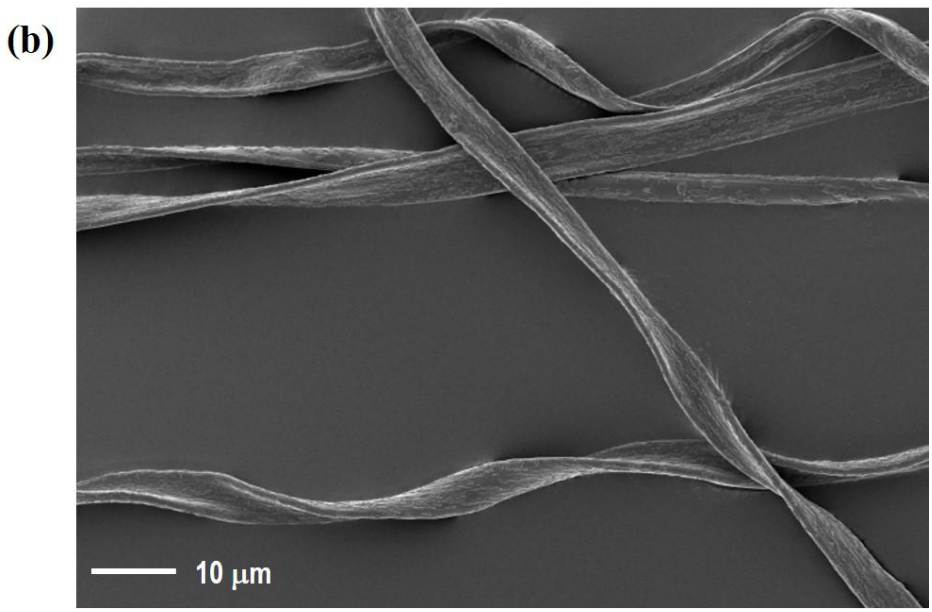

Figure 3-11 SEM micrographs of electrospun helical PVP/PEO-Ag fibers produced with (a) concentric and (b) off-centered spinnerets.

Fibers created with the off-centered spinneret had significantly higher proportions of helical fibers, while the concentric nozzle created more straight fibers. Morphological differences were also evident. The off-centered spinneret created fibers with more twisting and tighter pitches than those created with the concentric spinneret. Previous studies have demonstrated that these effects are due to an uneven electric field distribution. We therefore simulated the behavior of the electrified jet under an applied asymmetric electric field distribution.

The initial deformation of ejected fluid from an asymmetric electrode was analyzed using the simulation parameters described above. A two-dimensional model that considers the asymmetric spinneret and the applied potential was used to predict the

motion of the ejected jet within the stable jet region. The model geometry used the same dimensions as those of the spinneret used in our experiments (**Figure 3-12**).

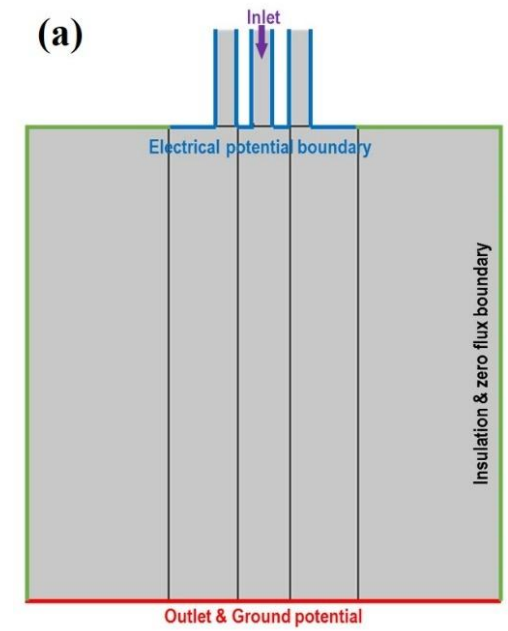

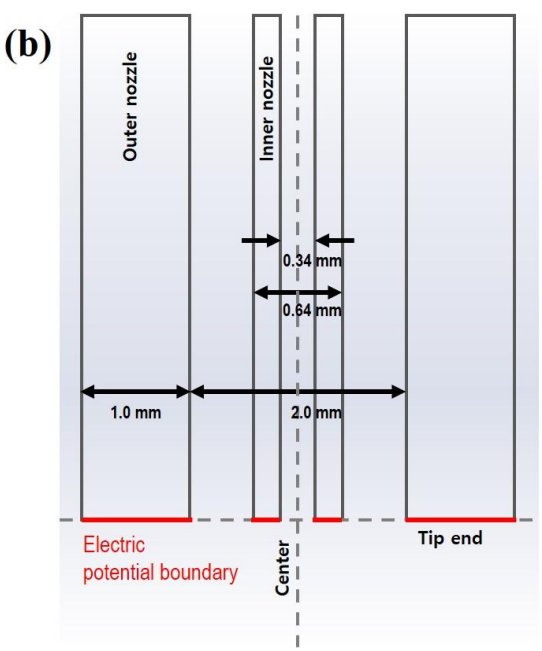

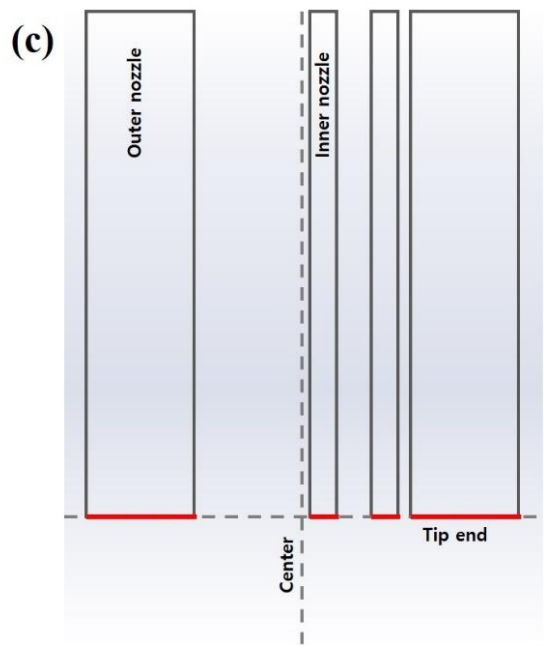

Figure 3-12 (a) Schematic illustration of geometries and boundary conditions of the simulation model. (b) Inset box showing materials and initial condition of interface between liquid and gas interface.

Figure 3-13 (a) and **(b)** present the jet propagation as a function of electrospinning for the concentric and off-centered cases, respectively. The simulation yielded volume fractions of each fluid and associated streamlines. The red lines in **Figure 3-13** indicate the movement of fluids by the electrical wind due to propagation of the electrified jet. In the off-centered case, we observed a large bending of the jet near the spinneret. Although a slight bend was also evident in the concentric case, the off-center jet exhibited much larger curvatures with drag at the jet/air interface affecting the dynamics of the surrounding air. These simulations confirmed that the electric field distribution can affect the formation of the initial jet curvature near the spinneret

or electrode, resulting in asymmetric deformation. This resulted in higher proportions of helical fibers when using the asymmetric spinneret.

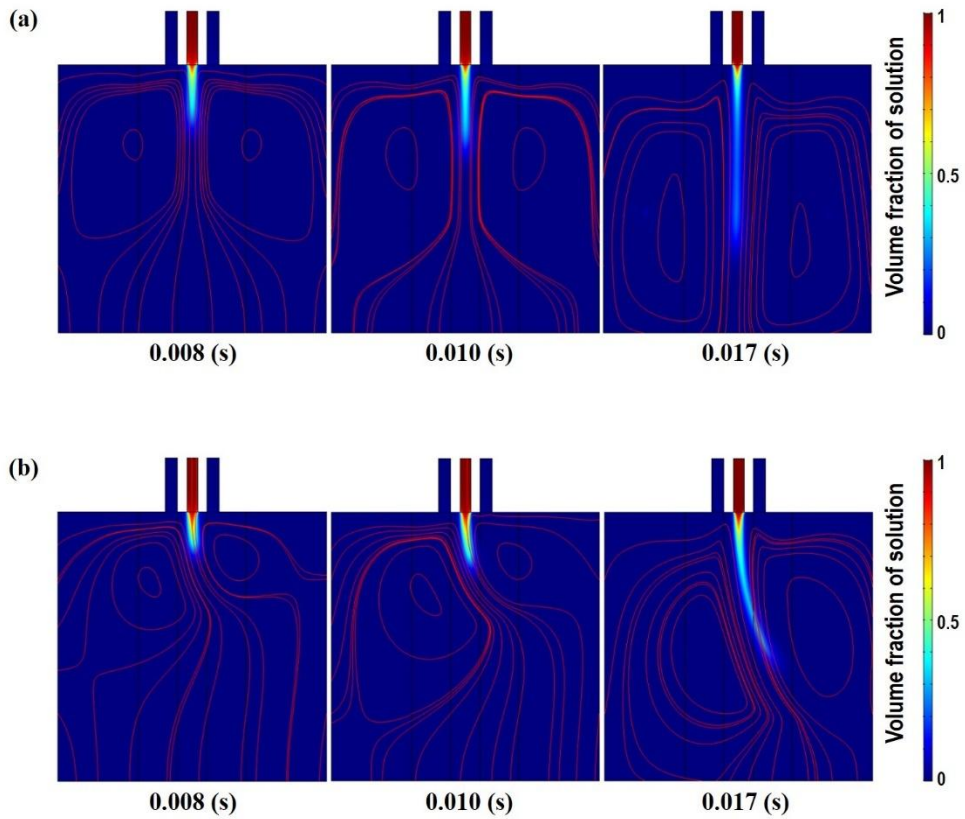

Figure 3-13 Numerical simulations of electrospun jet morphologies created with different spinnerets (electrodes): (a) concentric spinneret and (b) off-centered spinneret.

Although this report proposes a new way to fabricate helical fibers using an electrospinning process, certain limitations remain. The first is the compatibility of polymers with various solvents having different vapor pressures. Second, the electrospinnability of highly conductive materials is generally poor.[265] Finally,

rapid solidification can result in electrospun fibers of relatively poor quality, *i.e.,* large diameter, rough surface, uneven diameter distribution.[292] Resolving these issues will yield an electrospinning process that will greatly contribute to the nanotechnology industry.

3.4. Summary

The effects of solvent vapor pressure on the solidification position of a jet of electrospinning fluid and on subsequent fiber structure were investigated. As the vapor pressure of the solvent increased, the morphology of the fibers changed dramatically from straight to helical due to rapid solidification. This finding suggests that solidification occurred prior to the onset of bending instability while further elongation during the whipping stage was suppressed such that the fibers maintained their initial curvature. To control the solidification position, a conductive solution was prepared by adding a large amount of silver ion to the polymer solution. The fiber diameter resulting from the ion-containing jet decreased rapidly with distance from the spinneret due to the increased charge density of the solution and the consequent electric forces. Simulation results confirmed that fiber diameter is significantly reduced when the jet solidifies before the evolution of bending instability (whipping). Experimentally, rapid solidification of the jet yielded helical fibers. Additionally, the application of an uneven electrical field distribution resulted in asymmetric behavior of the ejected jet near the spinneret tip. This produced higher proportions of helical fibers due to intrinsic deformation and rapid solidification within the stable jet region.

Chapter 4. Fabrication of a stretchable, wrinkle-free electrode with switchable transparency

4.1. Transparent and stretchable electrode

Transparent and stretchable electrodes (TSEs) are a new class of materials under rapid development because of their widespread applications for stretcha ble electronics and optoelectronics.[293] TSEs are optically transparent, electr ically conducting, and mechanically deformable; these crucial but somewhat conflicting properties must be integrated simultaneously. Furthermore, TSEs c an be integrated with humans via wearable or implantable electric devices th at monitor human activity or extend perception via electronics[294] or the In ternet of things.[295] Specific applications include bioresorbable electronics, [296] skin-inspired devices (e.g., e-skins),[297, 298] smart windows,[299] wea rable sensors, and actuators.[300, 301]

Many researchers have attempted to fabricate TSEs using one-dimensional metal materials, which is an efficient and feasible route because of optical a nd electrical advances, especially in terms of silver nanowires (AgNWs) and nanofibers (AgNFs).[302, 303] Since the fabrication of solution-processed AgNW

transparent electrodes,[304] many researchers have attempted to improve their elec trical properties under mechanical deformation.[305-311]

Theoretical and experimental studies have determined that the junction between nanowires is crucial for maintenance of conductivity during mechanical deformation;[309, 312-317] the inter-junction resistance becomes relatively high.[318] Long AgNW electrodes have been used to enhance optoelectrical properties and flexibility by ensuring an effective percolation network and reducing inter-nanowire junctions.[319] AgNFs improve these effects, such that the electrical conductivity with flexibility substantially increases;[302, 320] stretchability is also enhanced with the aid of an elastomeric substrate and its adhesion between conducting materials.[321]

Stretching is the most challenging mechanical deformation mode for electrodes and has been achieved using elastomeric prestrained substrates.[293, 322] The underlying concept is simple: in-plane buckled fibers, formed by the prestrained substrate,[323] exhibit stretchability.[324] Therefore, the elastomeric substrate is crucial for fabrication of TSEs using this method.[293, 323, 325, 326] Polydimethylsiloxane (PDMS) has been used most frequently because of its transparency and elastomeric properties.[312, 321, 327] However, the elongation at break of PDMS is approximately 150%,[328] which is insufficient for induction of adequate in-plane buckling, because prestraining is restricted. PDMS requires an additional device to create and maintain its prestrained state; it can exhibit creep deformation under stress. When the load is removed from PDMS, large residual strain may remain, allowing insufficient buckling. In the worst scenario, large residual strain and low strength can be weaknesses for repeated stretching in

practical applications, such as epidermal[311] and tattoo-like devices.[329] Therefore, a better substrate is needed to increase in-plane buckling and maintain its mechanical properties after repeated stretching. The properties needed to meet this requirement are large elongation at break, sufficient strength, minimal residual strain, and no stress in the prestrained state.

A shape memory polymer (SMP) can be an alternative to PDMS for a substrate. An SMP is a smart material that exhibits the ability to return to its original shape from a temporarily deformed or fixed shape by an external stimulus, such as heating.[330] Crosslinked polycyclooctene (PCO) is an SMP with good shape memory performance, high fixity ratio for temporary shapes, and high recovery ratio from a fixed shape to the original shape.[331] Crystallinity of crosslinked PCO was decreased when heated above transition temperature due to melting of crystalline phase, however, it was recovered after cooling due to recrystallization. Because of its shape memory nature, an elongated PCO substrate can be fixed without any additional apparatus for maintenance of prestrain, and can recover its original shape.[332] Furthermore, crosslinked PCO exhibits advantageous optical properties. From an originally opaque state, it becomes transparent and elastomeric when heated above a transition temperature, due to a change in its microstructure. Our previous studies showed that it can be elongated up to 500%, and can recover 98% of its original shape at 200% elongation; moreover, its optical transmittance for 550 nm wavelength light is greater than 80%.[331]

Here, we fabricated a TSE using crosslinked PCO as an elastomeric substrate to achieve in-plane buckling of nanofibers. First, we fabricated a free-standing and

continuous AgNF network, which was transferred to the prestrained PCO substrate. To minimize adverse effects during the transfer process, free-standing AgNF was fabricated using a reduction reaction of Ag precursor nanofiber via ultraviolet (UV) radiation. Upon heating, the PCO substrate recovered its original shape and induced in-plane buckling of the AgNF network, thereby producing an SMP–TSE composite. The mechanical, electrical, and optical properties of the SMP–TSE were characterized to verify its suitability as a TSE. Finally, we demonstrated that the SMP–TSE was bendable, foldable, stretchable, and recoverable, while applying electrical stimuli.

4.2. Experimental

4.2.1. Materials

Highly crystalline PCO (MW 90,000; Vestenamer 8012, Evonik), dicumyl peroxide (98% purity; Sigma-Aldrich), and tetrahydrofuran (Sigma-Aldrich) were used to fabricate an SMP.[331] Silver nitrate (99%; DaeJung Chemicals & Metals), acetonitrile (anhydrous; Sigma-Aldrich), polyvinylpyrrolidone (PVP; MW 1,300,000; Sigma-Aldrich), and Triton-X (Sigma-Aldrich) were used as receiving materials for electrospinning of silver precursor nanofibers. PDMS (SYLGARD^{TM} 184 Silicon Elastomer Kit, Dow Corning) was used to fabricate PDMS film (10:1 ratio of resin and curing agent).

4.2.2. Preparation of shape memory polymer substrate

The crosslinked PCO, with 1% wt. dicumyl peroxide, was dissolved in tetrahydrofuran at 100°C for 4 h. The mixture was dried at room temperature for 24 h and then dried in a vacuum oven at 80°C for another 24 h, to remove the tetrahydrofuran. The dried mixture was molded in a hot-press machine at 80°C for 1 h and maintained at 170°C for 30 min for crosslinking. Fabricated, crosslinked, PCO substrates were used without any further treatment.

4.2.3. Fabrication of free-standing silver nanofiber

In total, 405 mg of PVP was dissolved in 5 g of acetonitrile at room temperature for 2 h; 2.43 g of $AgNO_3$ and 5.4 mg of Triton-X were added to the solution and stirred for 1 h. Before electrospinning was performed, the solution was vigorously stirred with a centrifugal mixer (ARE-310, THINKY) for 5 min. The flow rate of the solution was 0.4 mL/h, tip-to-collector distance was 15 cm, and applied voltage was 18 kV. Free-standing nanofibers were collected on a tailored collector to maintain their structure and minimize damage. The collector rotated at 50 rpm (21 cm/sec). The silver precursor nanofibers were reduced to silver by irradiation for 3 h with a UV curing machine (RX-H1000R, Raynics, Republic of Korea); the distance between the sample and the lamp was 10 cm. Notably, the UV reduction process provides a great advantage in terms of covering a large area, which allows mass production while completely preserving the structure of the nanofiber networks. To summarize, we fabricated PVP nanofibers containing a silver precursor ($AgNO_3$) by

electrospinning and proceeded to UV reduction, to prepare a free-standing AgNF network without damaging that network.

4.2.4. Characterization of SMP–TSE

We used field-emission scanning electron microscopy (FE-SEM, JSM-7600F, JEOL, Japan), X-ray diffraction (New D8 Advance, Bruker, Germany), infrared spectroscopy (Nicolet 6700, Thermo Scientific, USA), and optical microscopy (BX51, Olympus, Japan) for structural and chemical characterization of the AgNF, crosslinked PCO, and SMP–TSE. Mechanical characterization was conducted using a dynamic mechanical analyzer (DMA, Q800, TA Instruments, USA); bending and stretching tests for electrodes were conducted using a universal testing machine (Quasar 5, Galdabini, Italy). Resistance was measured using an electrometer (6517B, Keithley, USA). Changes in temperature were measured directly using an infrared camera (A325sc, FLIR, USA). Optical transmittance of the 550 nm wavelength was measured using a spectrophotometer (V-1100D, Shanghai Mapada Instruments, China).

4.3. Results and discussion

4.3.1. Fabrication of free-standing silver nanofibers

A thin and interconnected, continuous, AgNF network was first fabricated to develop the SMP–TSE (**Figure 4-1**).

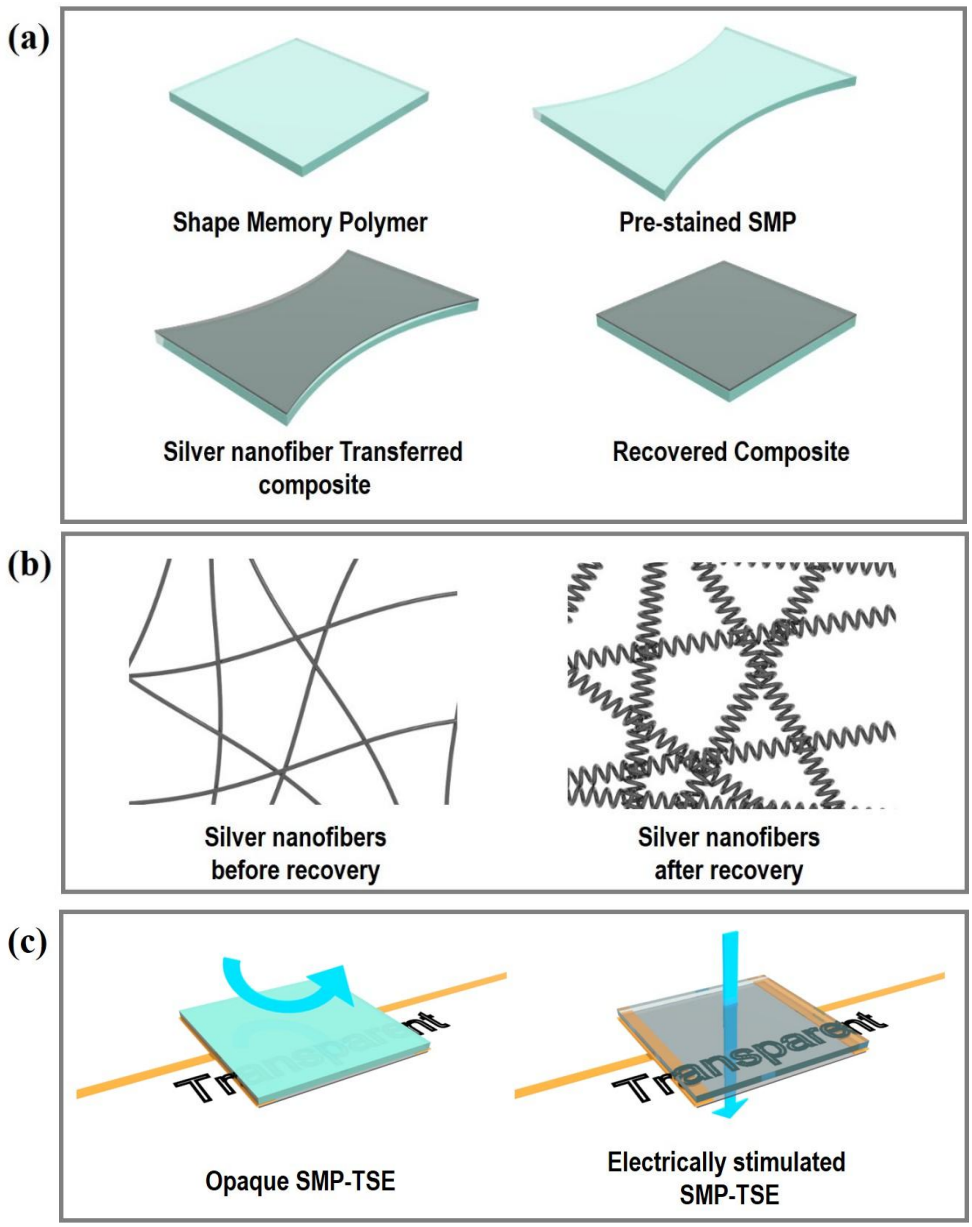

Figure 4-1 Schematic illustration of shape memory polymer–transparent and stretchable electrode (SMP–TSE) composite. (a) Fabrication of SMP–TSE. (b) In-plane buckling of silver nanofibers on SMP. (c) Electrically switchable transparent and opaque modes of SMP–TSE.

SMP–TSE was prepared using the two steps shown in **Figure 4-1a**. First, crosslinked PCO film was heated for its lower elastic modulus and prestrained to 200%. The film was then cooled to room temperature to fix the elongated shape. Second, free-standing AgNFs were transferred to this prestrained substrate. These were attached using a small amount of ethanol, thereby forming the SMP–TSE composite. The SMP–TSE was heated above the transition temperature of PCO, thus recovering its original shape and forming sufficient in-plane buckling of AgNFs (**Figure 4-1b**). To apply electrical stimuli, copper tape electrodes were attached to the AgNFs; changes in temperature, optical transmittance, elastic modulus, and shape memory behaviors were observed (**Figure 4-1c**). The AgNFs were fabricated using electrospinning. The prepared electrospinning solution became yellow due to the reduction of silver ions to silver nanoparticles (AgNPs) due to the mildly reducing nature of polyvinylpyrrolidone (PVP) (see **Figure 4-2** for UV–visible spectroscopic analysis).

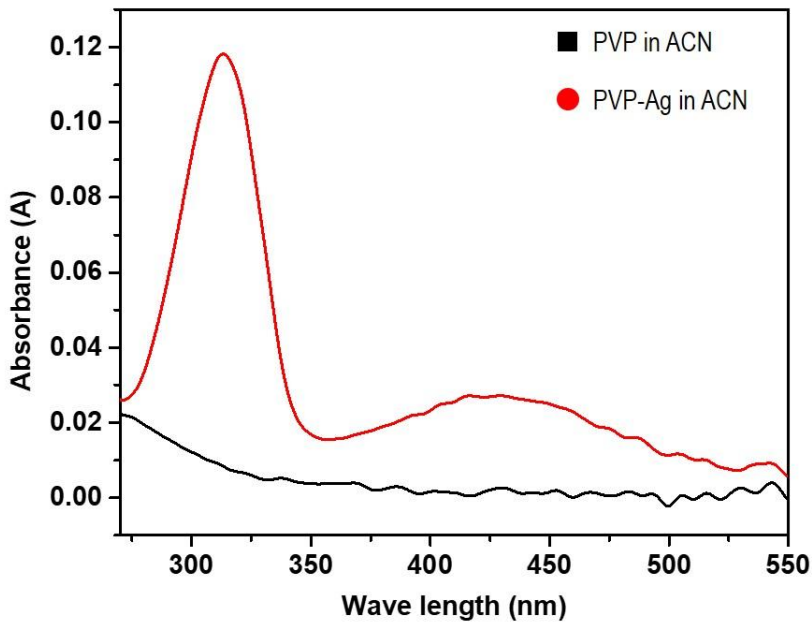

Figure 4-2 UV–visible spectroscopic analysis of polyvinylpyrrolidone (PVP) solution and PVP–$AgNO_3$ solution dissolved in acetonitrile.

UV–visible light was absorbed near wavelengths of 310 and 425 nm. The small peak near 420 nm could be caused by a surface plasmon resonance peak of AgNPs,[333] implying that a small amount of AgNPs had already formed during solution mixing, due to a coordination–reduction mechanism.[333] The wavelength near 310 nm was absorbed, reducing silver ions to AgNPs. After 3 h of UV reduction of the electrospun Ag precursor nanofibers using the prepared solution, AgNPs formed on the surface of the nanofibers. As the AgNPs grew, it became more difficult for the UV (needed for further reduction of Ag ions) to penetrate the fibers. Therefore,

uneven growth of AgNPs was observed between the top and bottom sides after the UV reduction process (**Figure 4-3**).

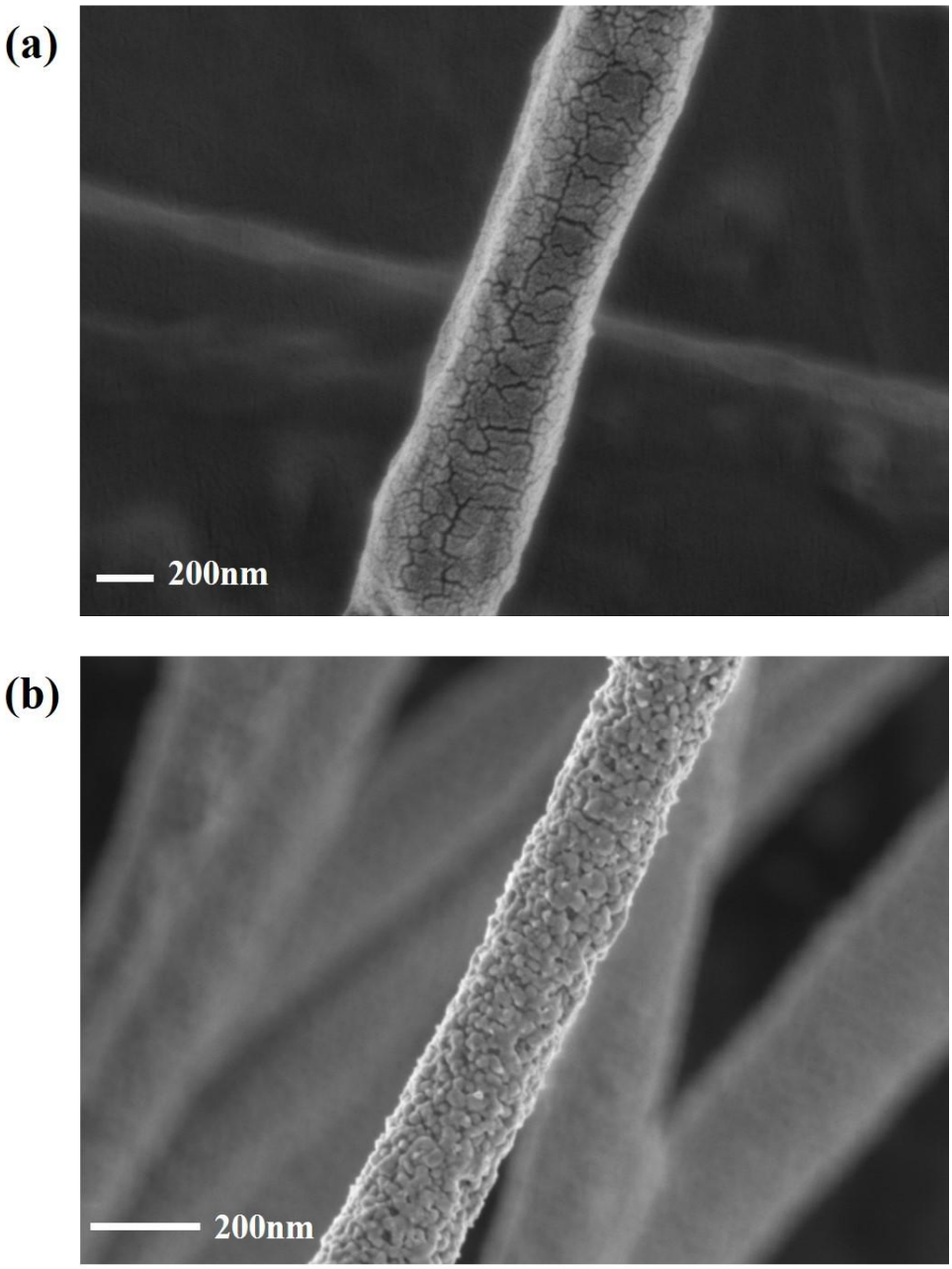

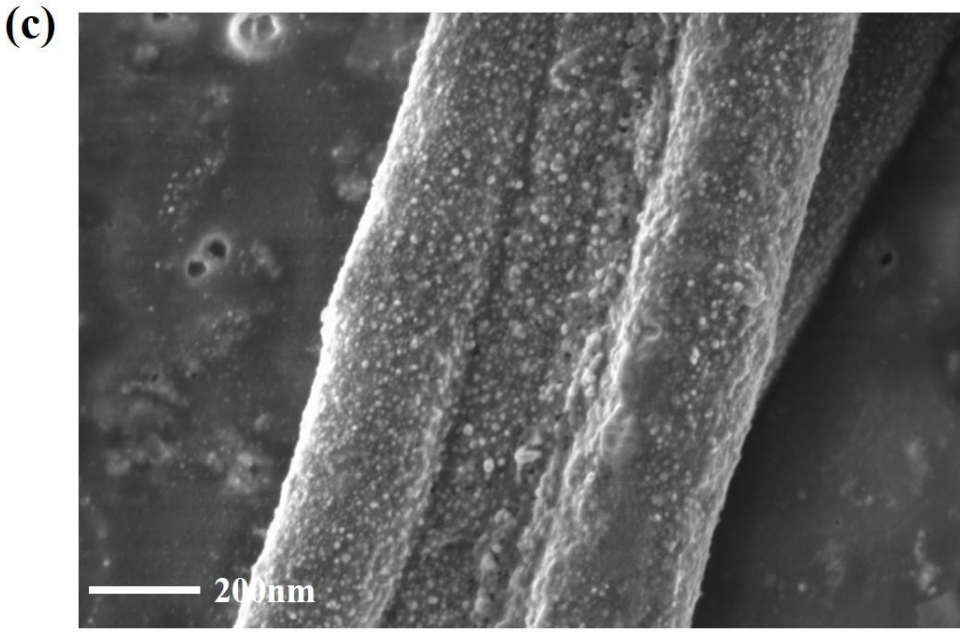

Figure 4-3 Field-emission scanning electron microscopy image of Ag nanofibers. (a) Silver precursor nanofiber before UV reduction, and (b) Top surface and (c) bottom surface after 3h of UV reduction.

To fabricate uniform AgNFs, UV should evenly irradiate the precursor nanofibers. When the nanofibers are on the substrate, the bottom side cannot always be reduced. Despite use of transparent substrates, such as glass or polymers, the majority of wavelengths near 300 nm are absorbed by the substrate, yielding a similar result. Furthermore, polymers absorb wavelengths of 300–400 nm and show yellowing or degradation due to a change in molecular structure.[334] Therefore, the free-standing fiber network is necessary not only for minimizing the damage during transfer but for uniformly reducing AgNFs. A tailored collector was used for electrospinning of free-standing nanofibers (**Figure 4-4**). Uniform reduction of the Ag precursor nanofiber was visible after 3 h of UV reduction.

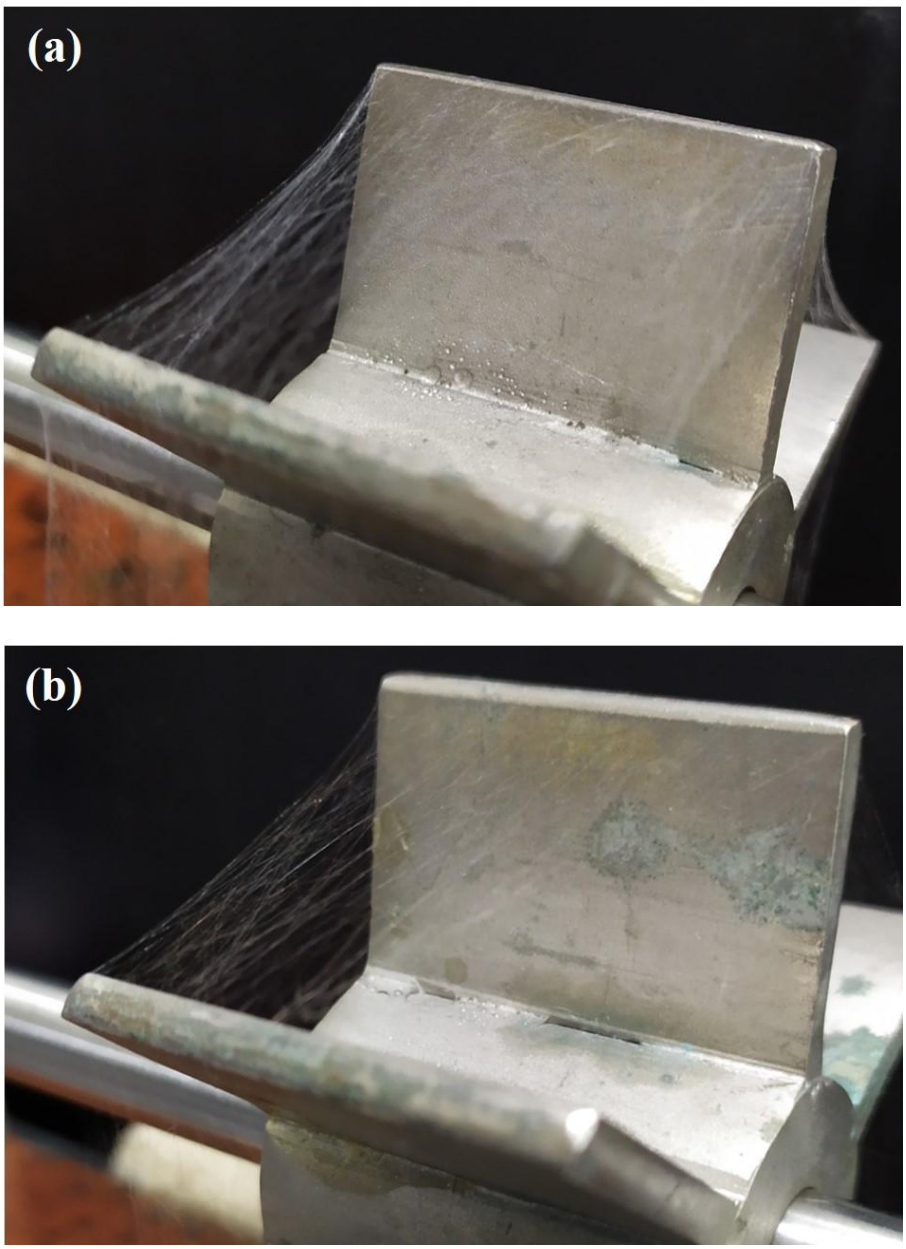

Figure 4-4 (a) Electrospun Ag precursor nanofiber collected on a tailored collector, and (b) Ag nanofiber network after 3 h of UV reduction.

Figure 4-5 shows FE-SEM images of the prepared AgNF, confirming that reduced AgNPs were densely formed on the surface of the PVP fiber frame. The average size of the particles was approximately 14 nm (standard deviation, 5.5 nm). Because AgNPs formed along the surface, electron conduction is expected via percolation. Junctions in AgNW and AgNF networks are known to exhibit high resistance and negatively affect overall conductivity.[314] The resistance of the junction can be reduced by increasing contact area between wires. The junction resistance can be reduced by robust welding during UV reduction process, resluting in improving conductivity.[302, 323] Our study confirmed that welding occurred at junctions between AgNFs, as shown in **Figure 4-5b.** In addition, FE-SEM photographs show that thin AgNFs, with average diameters of 350 nm, were fabricated by electrospinning. The X-ray diffraction results confirm that the AgNFs consist of AgNPs (**Figure 4-6**). The X-ray diffraction pattern has 2θ values of 38.17°, 44.43°, 64.66°, and 77.4° for the (111), (200), (220), and (311) planes of the face-centered cubic structures of Ag.

The cohesiveness of AgNPs in our AgNF was investigated by washing AgNFs with ethanol and acetone several times (see **Figure 4-7** for an image of a cross-section of washed AgNF). After AgNFs had been washed, hollow nanofibers remained. Because of even irradiation of UV, the thickness of the outer silver layer was uniform (approximately 100 nm). Reduction of AgNFs occurred first at the surface; as the reaction proceeded, this prevented UV from penetrating the fibers. Thus, unreacted PVP and $AgNO_3$ remained inside the AgNFs; these unreacted components were removed by washing, such that hollow fibers remained. Because electrons can move

through the surface of conductive materials, the washed AgNFs are expected to function well as electrodes.

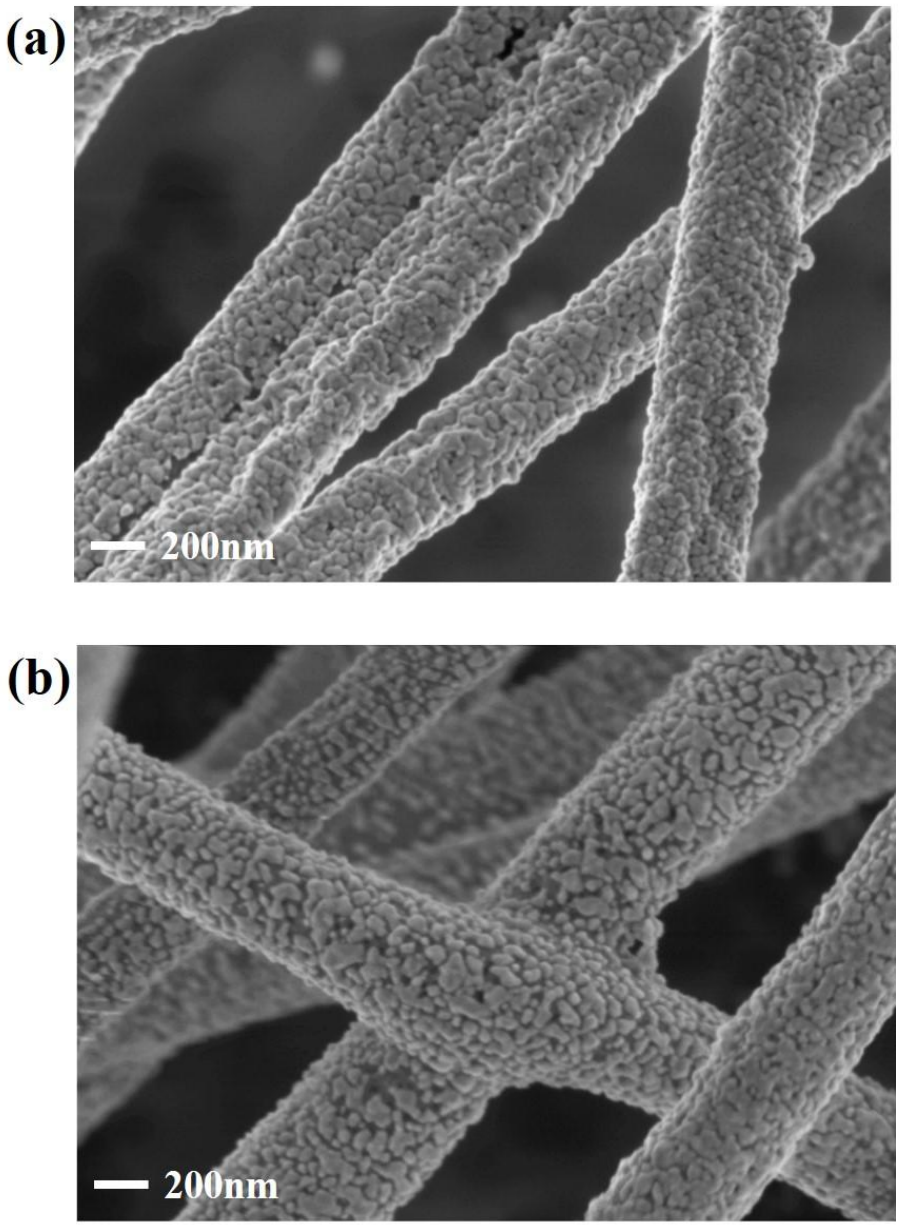

Figure 4-5 FE-SEM images of Ag nanofiber after UV reduction. (a) Electrospun Ag nanofibers and nanoparticles along them. (b) Junctions formed between fibers during UV reduction.

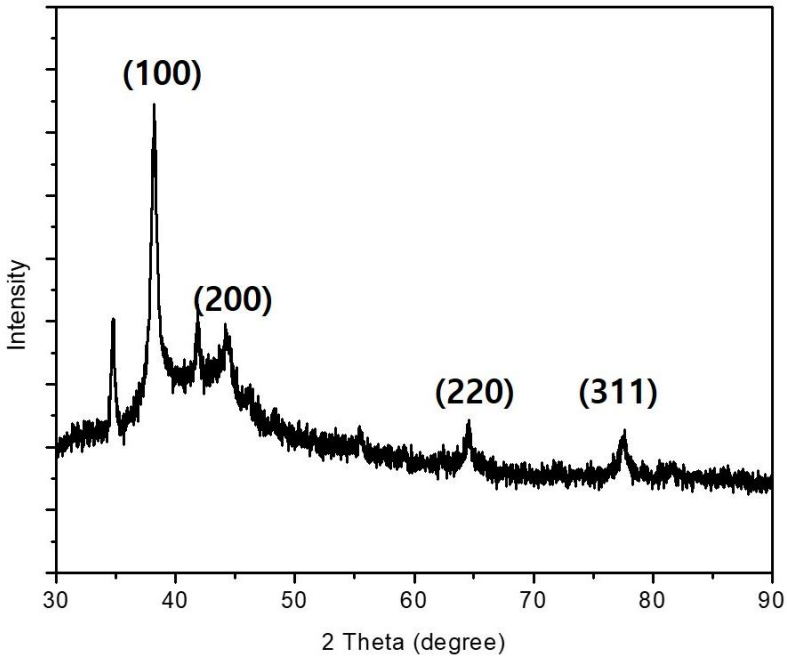

Figure 4-6 X-ray diffraction analysis of silver nanofibers after UV reduction.

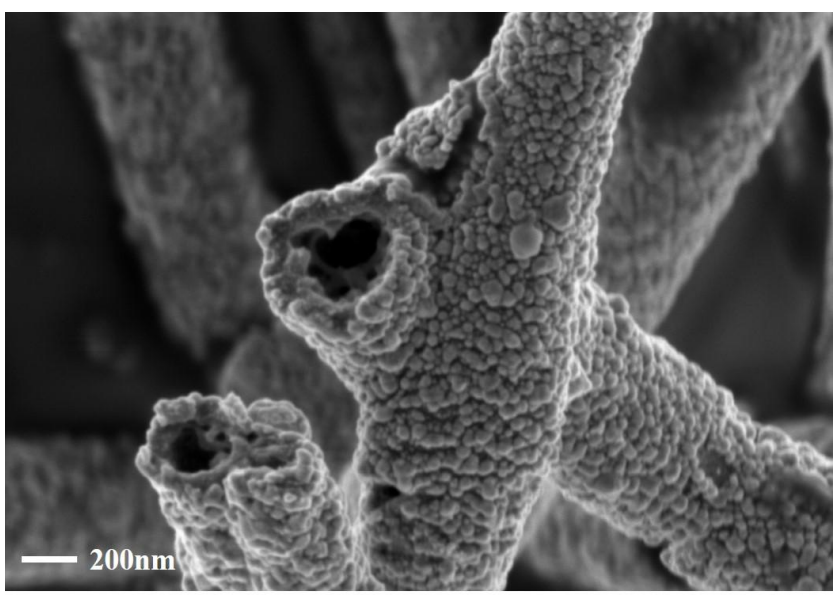

Figure 4-7 FE-SEM image of UV-reduced Ag nanofiber washed with ethanol and acetone.

4.3.2. Optoelectrical properties of silver nanofibers

The optical transmittance and resistance of the fabricated AgNF was characterized (**Figure 4-8**). The transmittance, T, of the electrode based on fibrous materials can be estimated by the area fraction, AF, of conducting materials, such that $\%T = 100 - aAF$, where a is a coefficient that depends on the material.[335] To measure the optoelectrical properties, we controlled the AF of AgNFs by varying electrospinning time from 10 s to 2 min. In general, the AgNW electrode measured approximately 10 Ω/sq. at 90%.[302] The prepared AgNFs showed a resistance of 3.63 Ω/sq. with T of 97.57% at the 550 nm wavelength. These results are comparable with the findings of prior studies, indicating good optoelectrical properties.[320] The sheet resistance of an AgNW-based transparent electrode is mainly determined by the junction resistance between wires, because the resistance of a junction is approximately 11 Ω; a reduced number of junctions is required to improve sheet resistance.[314] In AgNFs, as the aspect ratio of the material increased from wire to fiber, the number of junctions decreased and the space between fibers increased, resulting in a continuous AgNF network with good optoelectrical properties.

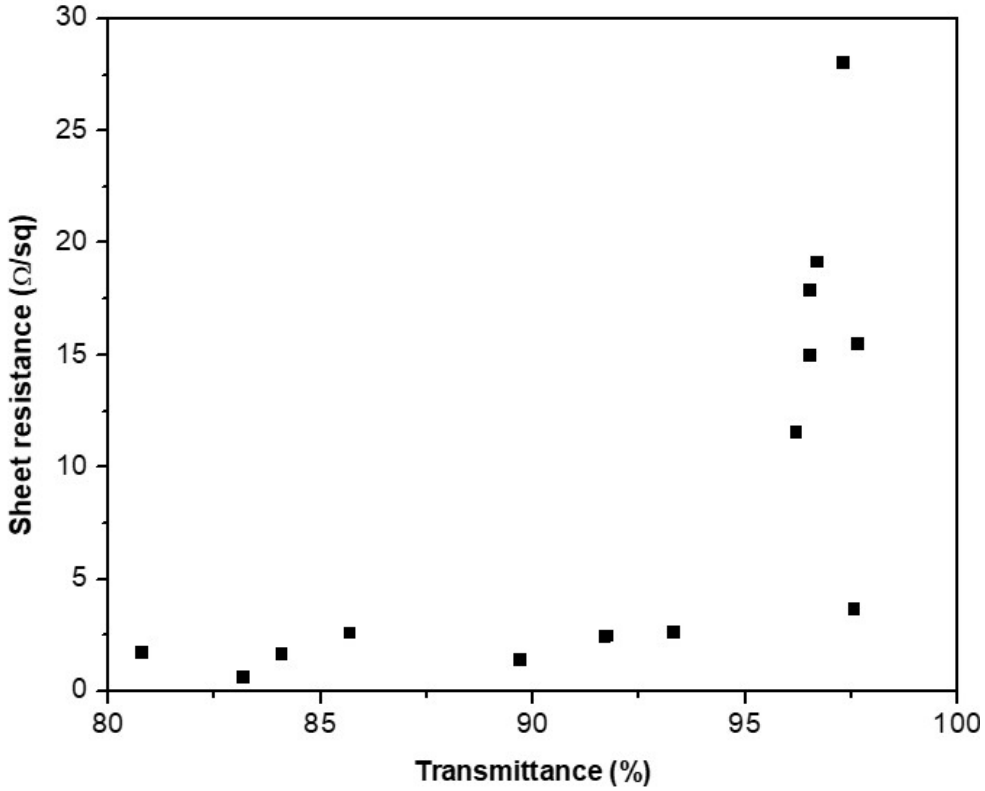

Figure 4-8 Optical transmittance of visible light at a wavelength of 550 nm and the relationship between optical transmittance and sheet resistance.

4.3.3. Shape memory substrate

Crosslinked PCO substrates were prepared and their mechanical properties and shape memory performance were characterized, as shown in **Figure 4-7**. The residual strain of PCO was analyzed according to the applied tensile strain, then compared with the residual strain of PDMS (**Figure 4-9a**). Residual strain is known to affect the formation and shape of wrinkling or folding.[336] Because of its excellent elastomeric properties and shape memory behavior, the PCO showed a

high recovery ratio. Under 50%, 100%, and 150% tensile strains, the residual strains of the PCO were 0.62%, 2.26%, and 2.27%, respectively; the residual strains of PDMS were 1.12%, 9.32%, and 23.32%, respectively. At 200% strain, the breaking strain of PDMS, PCO showed only 3.01% residual strain. Furthermore, the PCO could be elongated up to 550% at room temperature and 280% at 80°C; therefore, PCO is beneficial for fabrication of buckled nanofibers, because of its large prestrain (**Figure 4-10**).

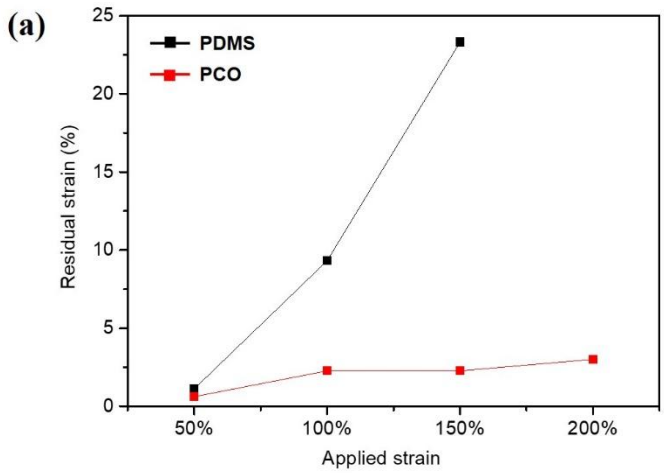
(a)
PDMS
PCO
Residual strain (%)
0
5
10
15
20
25
50%
100%
150%
200%
Applied strain

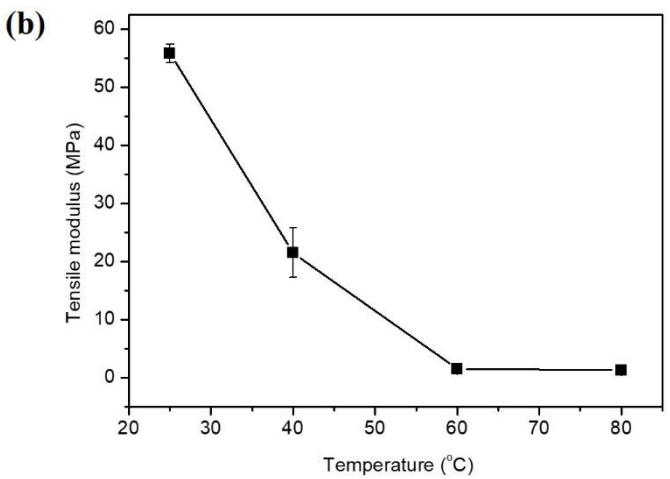
(b)
Tensile modulus (MPa)
0
10
20
30
40
50
60
20
30
40
50
60
70
80
Temperature (°C)

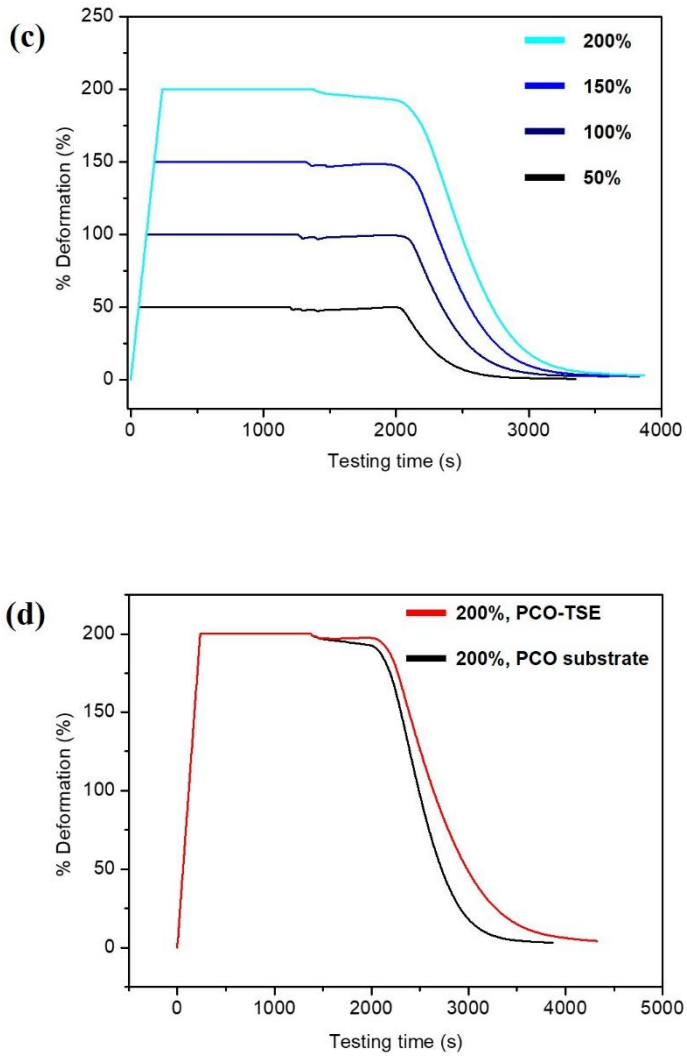

Figure 4-9 Mechanical and shape memory properties of crosslinked polycyclooctene (PCO) substrate. (a) Residual strain vs. applied strain of crosslinked PCO and polydimethylsiloxane (PDMS); (b) elastic modulus of crosslinked PCO vs. temperature and shape memory behavior of (c) Crosslinked PCO substrate for different strains; and (d) shape memory polymer–transparent and stretchable electrode (SMP–TSE) at a strain of 200%.

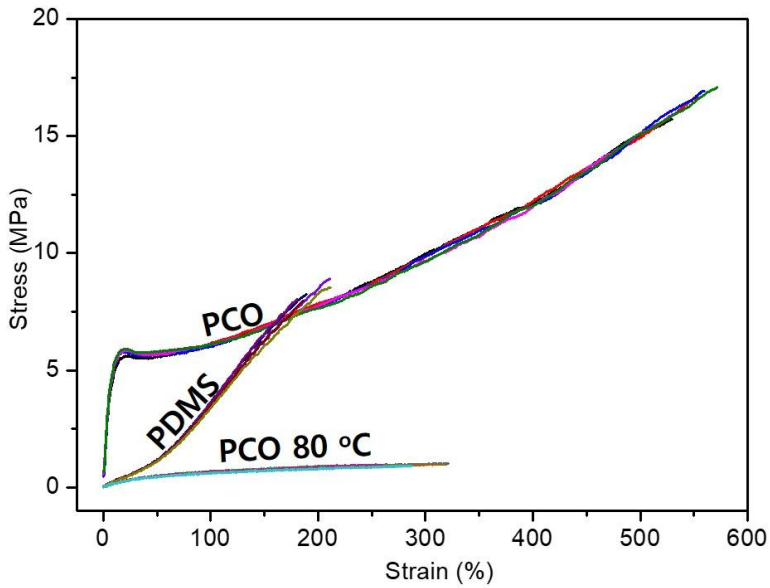

Figure 4-10 Stress–strain curves of polydimethylsiloxane (PDMS), crosslinked polycyclooctene (PCO) at room temperature, and crosslinked PCO above its transition temperature (80°C). The breaking strains were 195% (PDMS), 280% (crosslinked PCO, room temperature), and 550% (crosslinked PCO, 80°C).

The elastic modulus of PCO can be adjusted by temperature change. **Figure 4-9b** shows the elastic modulus of PCO according to temperature. The modulus was 55.8 MPa at room temperature; it abruptly decreased above the transition temperature, T_g = 65°C, and was 1.29 MPa at 80°C (**Table 4-1**). Importantly, T_g was determined by a dynamic mechanical analyzer oscillation test (**Figure 4-11**); a detailed analysis of the mechanical behavior was performed in our previous study.[331] **Figure 4-9c** shows the shape memory behavior of the PCO, which was characterized by a cyclic

thermomechanical test.[337, 338] The test involved four steps. First, the specimen was elongated up to 50, 100, 150 and 200 % with the strain rate of 50%/min at 80 °C.

Table 4-1 Transition temperature, T_g, of crosslinked PCO substrate, deduced from the tan δ value of a dynamic mechanical analyzer oscillation test.

Sample	T_g (°C)
1	63.6
2	64.8
3	64.2
Average	64.2
Deviation	0.4899

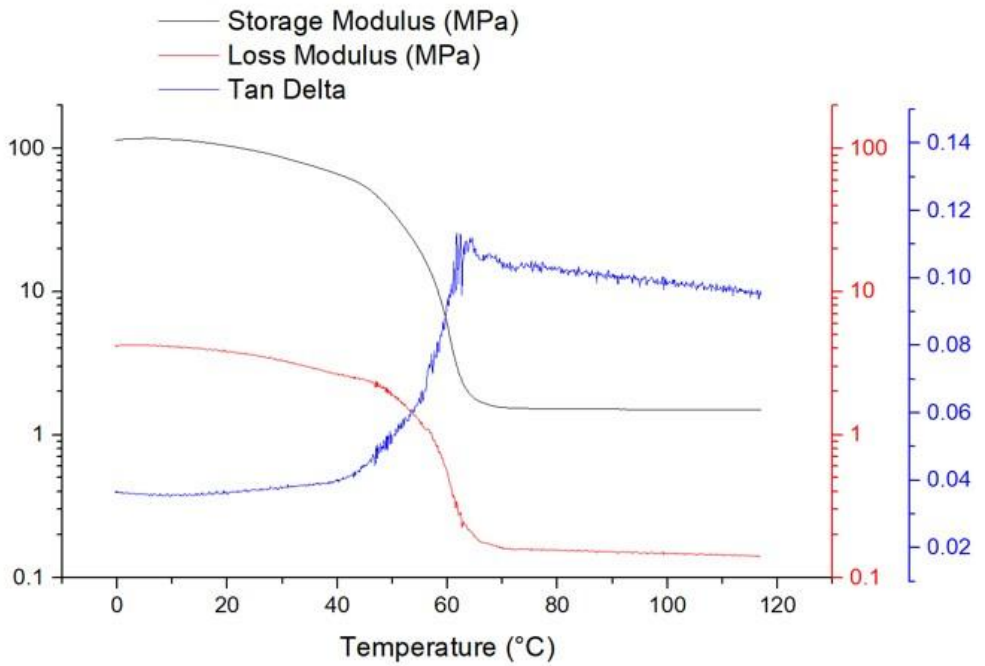

Figure 4-11 Dynamic mechanical analyzer oscillation test of crosslinked PCO.

Second, the specimen was cooled to 0°C with fixed elongation. Third, the specimen was unloaded for 5 minutes to obtain a temporary shape. Fourth, the strain was recovered by heating to 80°C. The shape memory properties were evaluated by fixity ratio and recovery ratio. They are calculated by the following equations

$$fixity\ ratio = \varepsilon_f / \varepsilon_m \qquad \textbf{(7)}$$

$$recovery\ ratio = \left(\varepsilon_m - \varepsilon_r\right) / \varepsilon_m \qquad \textbf{(8)}$$

Where ε_m is the maximum strain, ε_f is the strain of the temporary shape, and ε_r is the strain after recovery step. The fixity ratio was 99.9, 99.6, 99.0 and 96.5% and the recovery ratio was 98.8, 97.7, 98.5 and 98.5% under 50, 100, 150 and 200% uniaxial

strain respectively. The outstanding recovery behavior under 200% strain was used to fabricate the buckled form of our AgNF network.

Next, we investigated how the crosslinked PCO could enhance the stretchability of SMP–TSE, focusing on the shape of buckled AgNFs. The relationship between wavelength, λ, and amplitude, A, of buckled nanofibers is related to the ratio of the elastic moduli of an electrode and its substrate.[323, 338-340] Both λ and A increase as the elastic modulus of the substrate decreases. In addition, A increases with increasing substrate prestrain (see **(9)** and **(10)** in reference [323, 338] for detailed relationship).

$$A \approx \frac{12}{5}\left(\frac{E_{AgNW}}{\overline{E}_s}\right)^{1/4} R\sqrt{\varepsilon_{pre} - \varepsilon_{cri}} \qquad \textbf{(9)}$$

$$\lambda \approx \frac{3}{10}\left(\frac{E_{AgNW}}{\overline{E}_s}\right)^{1/4} R \qquad \textbf{(10)}$$

As shown in **Figure 4-11,** when the temperature increased, the elastic modulus of PCO decreased (from 55.8 MPa at room temperature to 1.29 MPa above T_g). The observed elastic modulus of PCO is smaller than the elastic modulus of PDMS (2.05 MPa), theoretically implying that λ can be decreased by 16.7% and A can be increased by 8.9%. The ratio of the lengths of the buckled and stretched fibers with a sinusoidal wave structure can be described by the waviness, A/λ.[338, 340] A/λ increased by 29%, offering greater stretchability. Furthermore, when considering

maximum prestrain, A can be increased by up to 550% for the PCO substrate, because of its higher breaking strain (**Equation 10**).

4.3.4. Shape memory polymer–transparent and stretchable electrode

To prepare SMP–TSE, an AgNF network was transferred to the crosslinked PCO substrate, which had been elongated to 200%. When the PCO with AgNF was heated, it recovered its original shape and formed in-plane buckled AgNF. The structure of this buckled AgNF is shown in **Figure 4-12**. Because of adhesion by ethanol, out-of-plane buckling, which has adverse effects after repeated stretching,[341] was observed infrequently. Furthermore, a serpentine-like structure of AgNFs formed efficiently, because of the biaxial recovery of the SMP. Mechanical and electrical characterization of this fabricated SMP–TSE is shown in **Figure 4-13**.

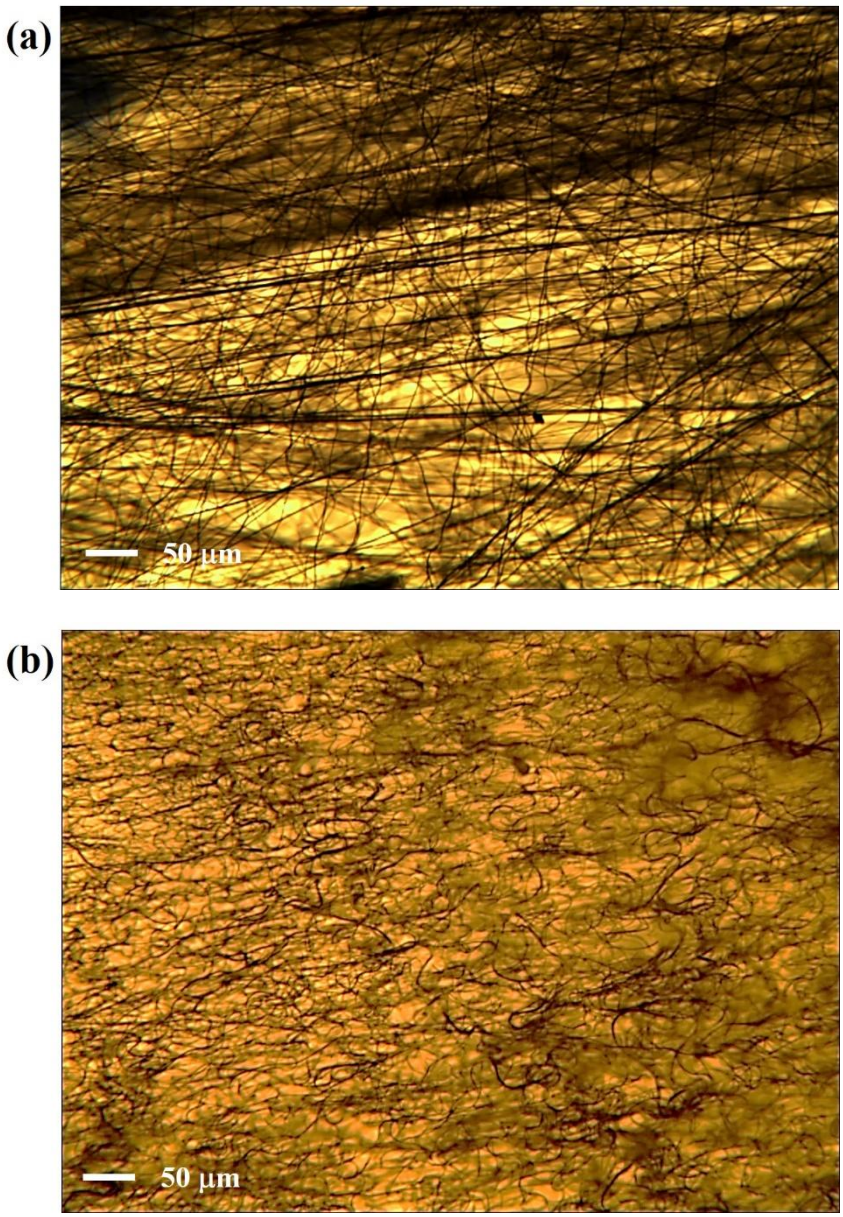

Figure 4-12 Optical microscopic images of shape memory polymer–transparent and stretchable electrode (SMP–TSE) composite. The Ag nanofiber array showed in-plane buckling. (a) Before recovery of crosslinked PCO and (b) after recovery (200% prestrain).

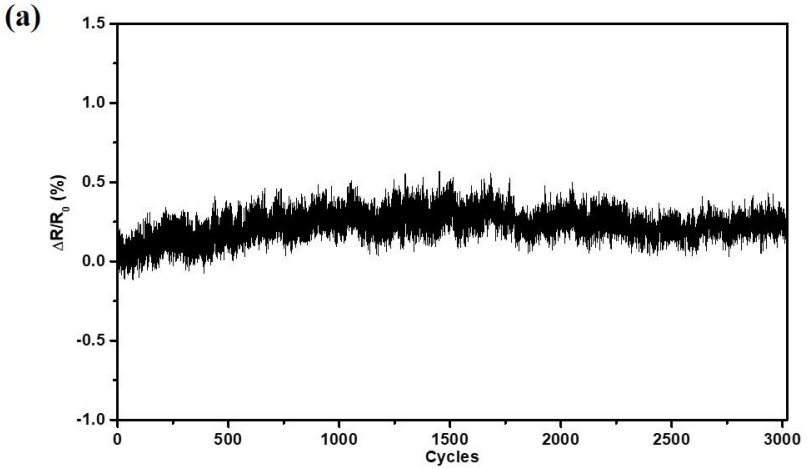
(a)
1.5
1.0
0.5
0.0
-0.5
-1.0
ΔR/R0 (%)
0
500
1000
1500
2000
2500
3000
Cycles

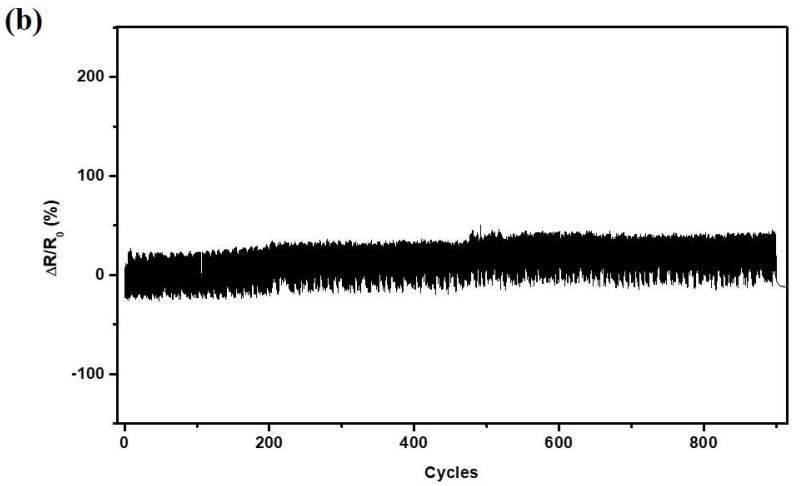
(b)
200
100
0
-100
ΔR/R0 (%)
0
200
400
600
800
Cycles

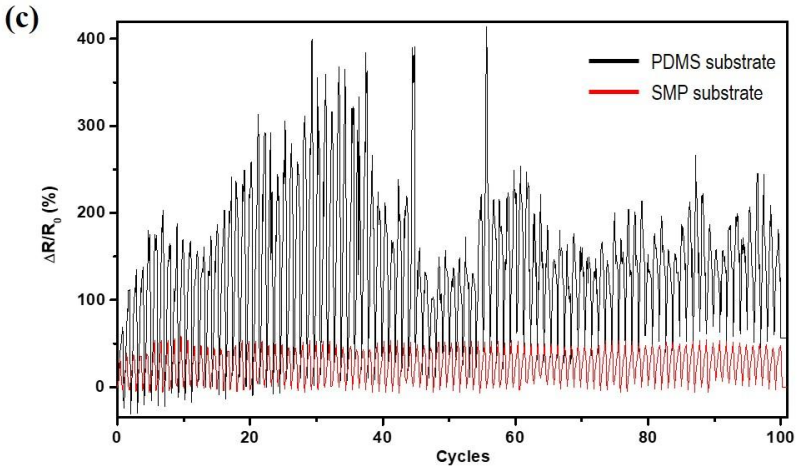

Figure 4-13 Electrical properties of shape memory polymer–transparent and stretchable electrode (SMP–TSE) during mechanical deformation. (a) Resistance change for a bending test over 3,000 cycles (radius of curvature of 0.45 cm), (b) stretching test over 900 cycles (uniaxial strain of 10%), and (c) stretching test over 100 cycles (uniaxial strain of 10%) of SMP–TSE and polydimethylsiloxane (PDMS)–TSE. Note that SMP-TSE was tested at elevated temperature (80 °C) higher than the transition temperature of SMP.

A bending test was conducted with a radius of curvature of 0.45 cm, which revealed negligible resistance change after 3,000 cycles (**Figure 4-13a**). A tensile stretching test showed a maximum resistance increase of 6.75% after 900 cycles with 10% uniaxial strain (**Figure 4-13b**). An electrode fabricated using PDMS under similar conditions was compared with the SMP–TSE (**Figure 4-13c**), which confirmed that the SMP–TSE showed a much smaller change in resistance during each cycle and over all cycles; this demonstrated the improved stretchability of SMP–TSE.

Finally, the thermal properties of the SMP–TSE composite were investigated while applying an electrical potential difference of 4 V. The temperature change was

observed using an infrared camera, as shown in **Figure 4-14**. The electrodes were able to heat the composite above T_g of PCO. Many previous studies have concluded that Joule heating occurs due to percolation of electrons and high interparticle resistance.[320] Because of this, and because of the high conductivity of the SMP–TSE, its temperature changed rapidly, exceeding T_g in a few seconds, which resulted in rapid microstructural changes.

This study investigated the electrical, optical, thermal, and mechanical properties of the SMP–TSE, as well as their relationships. To demonstrate the utility of the composite, a smart display was manufactured that is bendable, foldable, stretchable, and recoverable, and can also be controlled by electrical signals (**Figure 4-15**). **Figure 4-15a** shows the transition from the opaque to transparent modes of the SMP–TSE at 2 V. Thirty seconds and 45 s were required for turning on and off, respectively. The temperature of electrode elivated upto 70°C by applied volatge which is higher than trnasition temperature of the crosslinked PCO substrate. **Figure 4-15b** shows recovery from mechanical deformation by electrical stimulus. The deformed shape (60° folded for 1-mm thickness of SMP–TSE, 41.5% tensile strain) was fixed and recovered by applying a voltage. As a result, local recovery occurred in the conducting portion, which indicated successful shape memory behavior and optical transparency.

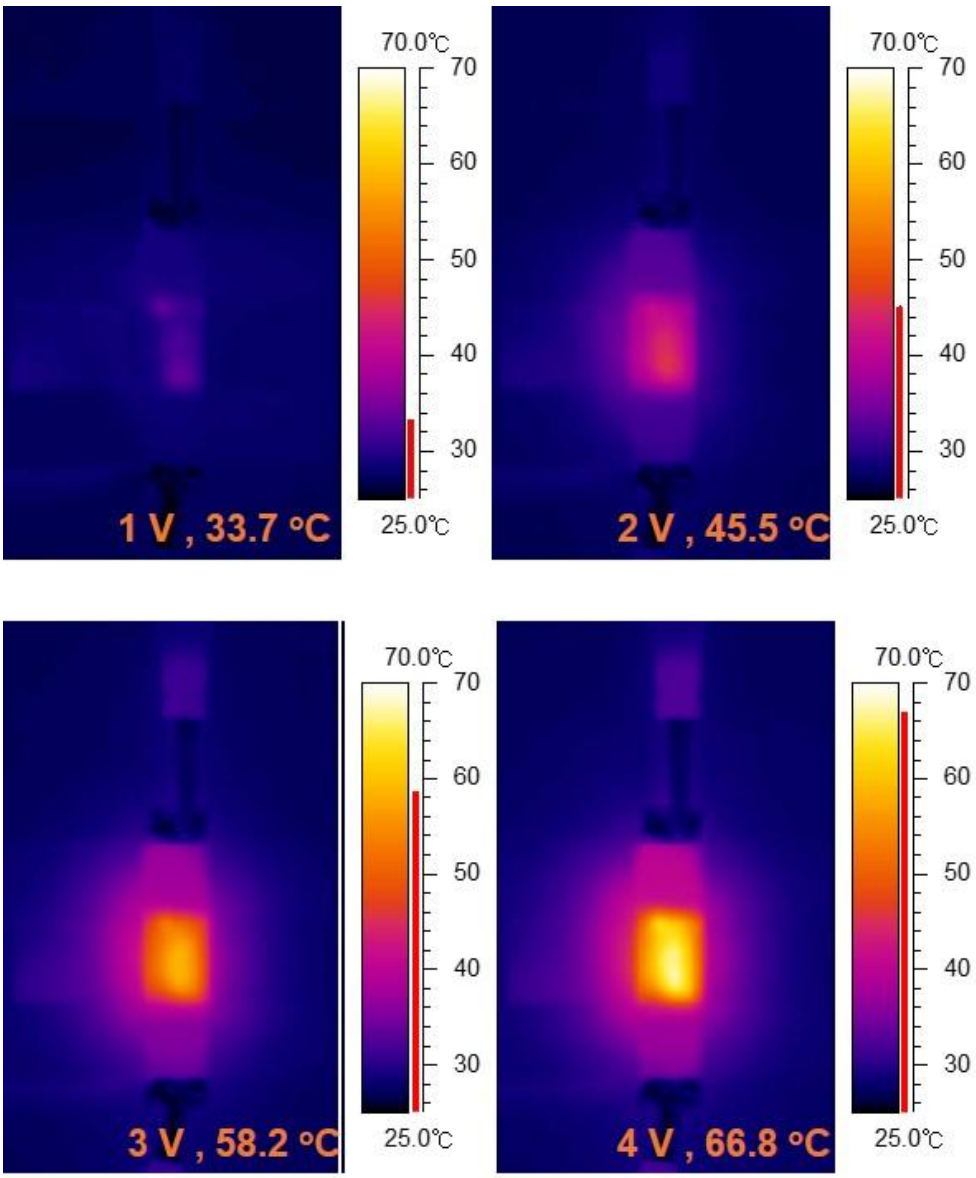

Figure 4-14 Thermal properties of shape memory polymer–transparent and stretchable electrode (SMP–TSE) with a 4 V potential difference applied.

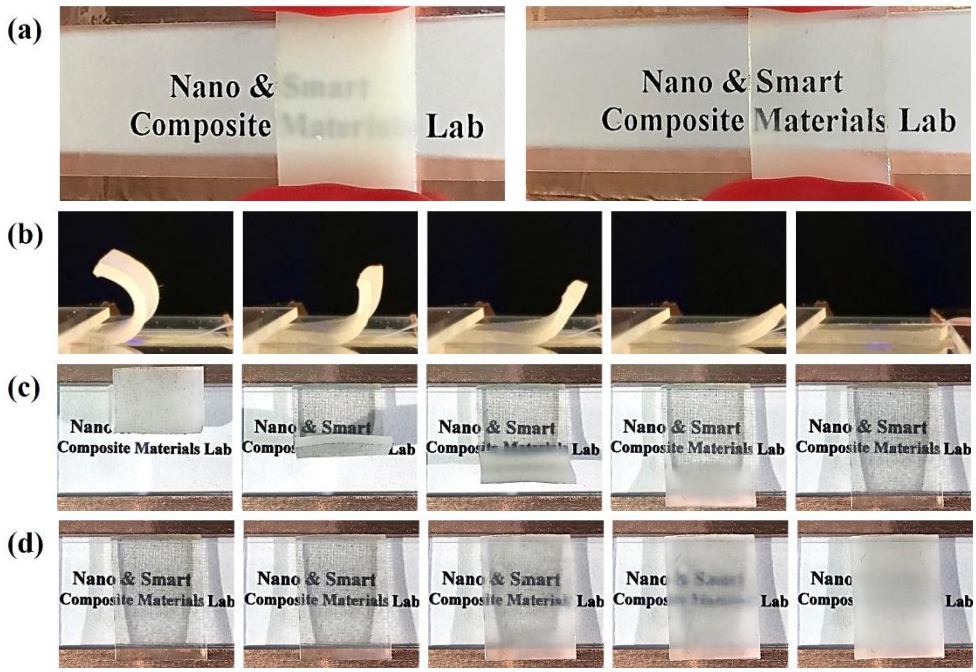

Figure 4-15 Demonstration of a shape memory polymer–transparent and stretchable electrode (SMP–TSE) smart display. (a) Electrical switching of optical transmittance (2 V, 30 s to reach transparent mode and 0 V, 45 s to reach opaque mode). Bending and recovery in (b) side view and (c) top view. (d) Transition to opaque mode after recovery.

4.4. Summary

We successfully fabricated a TSE using a continuous AgNF network with a crosslinked PCO substrate (SMP–TSE). Because of the shape memory behavior, particularly the good recovery characteristic of PCO, in-plane buckled nanofibers were efficiently formed by preparing the PCO substrate, which was prestrained and fixed by cooling in the deformed state; a continuous AgNF network was then transferred to the substrate and heated. The SMP–TSE was wrinkle-free and exhibited switchable optical transparency, alternating with the microstructure of the

PCO substrate. The SMP–TSE exhibited minimal change in resistance during repeating bending and slightly increased resistance (6.75%) during repeated stretching. Using SMP–TSE, we demonstrated an electrically actuated smart display with switchable optical transparency that is bendable, foldable, stretchable, and recoverable. We expect that this electrically actuated SMP–TSE can contribute to developments of skin-like electronic devices because of its simple and efficient production process, as well as its mechanical stability and good optoelectrical properties.

Chapter 5. Conclusions

This study aimed to fabricate silver nanofibers using new process parameters of electrospinning and develop transparent and stretchable electrodes for stretchable electronics using them. A series of research was carried out to achieve goals, from which the following conclusions were reached.

A simulation model was developed to promote industrial use of electrospinning including gas-assisted melt electrospinning. Two criteria were proposed to predict the spinnability of the material through multi-physics simulation of spinning behavior. A critical shear viscous stress (30 Pa) for spinnability was defined by analyzing the shear viscous stress on the jet surface. The critical electric field strength was defined as the electric field strength (1.5 kV/mm) at the end of the Taylor cone when critical shear viscous stress was developed. Based on those criteria, a spinnability diagram that can ensure minimal conditions for a successful multi-nozzle GAME process was proposed.

An electrospinning process for fabricating helical fibers was designed. We investigated the effects of the vapor pressure of the solvents on the solidification of the jet and following fiber structure. A dramatical change was observed as the vapor pressure of the solvent increased. The structure of the fibers was changed from straight to helical due to fast solidification. A conductive solution was prepared by adding large amount of silver ions to control the solidification position. Simulation

results showed that the thickness of the conductive jet rapidly reduced due to strong electric stress. Solidification of the jet was promoted, resulting in helical fibers. To enhance the helical structure, a nozzle with asymmetric geometry was used to make uneven distribution of electric field. As the results of asymmetric deformation, the portion and structure of helical fibers were enhanced.

Transparent and stretchable electrode was fabricated using continuous silver nanofiber network and crosslinked PCO substrate. SMP-TSE was fabricated by transferring free-standing AgNFs on prestrained crosslinked PCO substrate. Due to the shape memory behavior, in-plane buckled nanofibers were efficiently formed without wrinkling of substrate. The fabricated SMP-TSE exhibited great flexibility and stretchability. The resistance of the electrode showed minimal change during repeating bending and slightly increased resistance (6.75%) during repeated stretching. We demonstrated an electrically actuated smart electrode with switchable optical transparency that is bendable, foldable, stretchable, and recoverable.

Chapter 6. Appendix

Governing equations and boundary condition of gas-assisted polymer melt electrospinning process simulation

The polymer melt and hot air included in the simulation were assumed to be incompressible and Newtonian fluids. The liquid–gas interface was treated using a level-set equation. The Navier–Stokes equation used in the simulation is as follows [1-2]:

$$\rho\frac{\partial \mathbf{u}}{\partial t}+\rho(\mathbf{u}\cdot\nabla)\mathbf{u}=\nabla\cdot\left[-pI+\mu(\nabla\mathbf{u}+(\nabla\mathbf{u})^{T})\right]+\rho\mathbf{g}+\mathbf{F}_{\mathbf{st}}+\mathbf{F}_{\mathbf{e}}$$

$$\nabla\cdot\mathbf{u}=0$$

$$\frac{\partial\phi}{\partial t}+\mathbf{u}\cdot\nabla\phi=\gamma\nabla\cdot\left(h\nabla\phi-\phi(1-\phi)\cdot\mathbf{n}\right)$$

where ρ, $\boldsymbol{u}$, p, I, μ, $\boldsymbol{g}$, γ, ϕ, and h represent the density, velocity, pressure, identity matrix, dynamic viscosity, gravitational acceleration constant, level-set variable, re-initialization parameter, and interface thickness, respectively. The density and dynamic viscosity of the fluid were defined using the following level-set functions:

$$\rho = \phi\rho_{Polymer} + (1-\phi)\rho_{Air}$$

and

$$\mu = \phi\mu_{Polymer} + (1-\phi)\mu_{Air},$$

respectively.

The surface force ($\boldsymbol{F_{st}}$) is defined as

$$\mathbf{F}_{st} = \nabla \cdot (\sigma (I - (\mathbf{n}\mathbf{n}^T))\delta),$$

where σ is the surface tension coefficient and δ is the Dirac delta function to calculate the force acting on the interface. The volumetric electric force ($\boldsymbol{F_e}$) is derived from the electrostatic Maxwell stress tensor.

$$\mathbf{T}_e = \varepsilon\left(\mathbf{E}\mathbf{E} - \frac{\mathbf{E}^2}{2}I\right)$$
$$\mathbf{F}_e = \nabla \cdot \mathbf{T}_e = \rho_e \mathbf{E} - \frac{\mathbf{E}^2}{2}\nabla\varepsilon$$

where ε is the electric permittivity, which was also calculated using the level-set function, $\varepsilon = \phi\varepsilon_{Polymer} + (1-\phi)\varepsilon_{Air}$. Given E as the electric field and ρ_e as the volumetric charge density, the electric force due to free charge accumulation at the interface is defined as follows:

$$\mathbf{f}_s^{\mathbf{E}} = \frac{\varepsilon_0}{2}\left(\frac{(\mathbf{D}\cdot\mathbf{n})^2}{\varepsilon_0^{\,2}}\left(\frac{1}{\varepsilon_{Polymer}} - \frac{1}{\varepsilon_{Air}}\right) - (\mathbf{E}\cdot\mathbf{t})^2(\varepsilon_{Polymer} - \varepsilon_{Air})\right)\mathbf{n}\delta,$$

where ε_0, $\boldsymbol{D}$, $\boldsymbol{n}$, and $\boldsymbol{t}$ are the vacuum permittivity, electric displacement, interface normal, and tangential unit vector, respectively.

The charge conduction and convection during the electrospinning process were calculated by the charge conservation law:

$$\frac{\partial\rho_e}{\partial t} + \nabla\cdot(\rho_e\mathbf{u}) = -\frac{K}{\varepsilon}\rho_e,$$

where K is the electric conductivity of the fluid defined using the following level-set function:

$$(K = \phi K_{Polymer} + (1-\phi)K_{Air})$$

Finally, Gauss's law was used to calculate the electric field strength and distribution:

$$\nabla \cdot (\varepsilon \mathbf{E}) = \rho_e, \quad \mathbf{E} = -\nabla V$$

The geometry and boundary condition for the model is presented in **Figure A-1.**

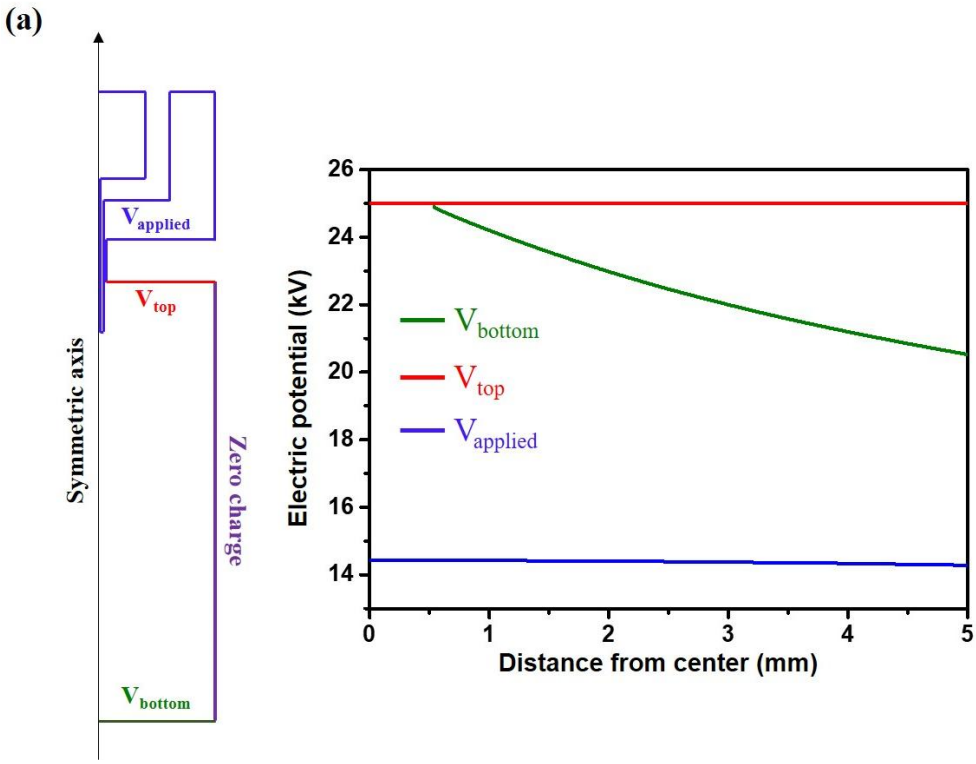

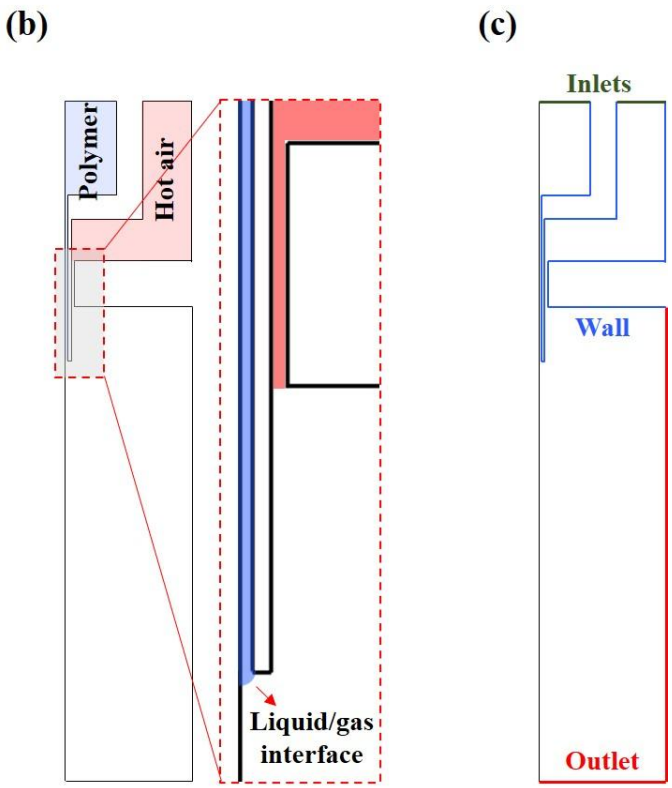

Figure A-1 Geometry and boundary conditions of single-nozzle model. (a) Electrostatic boundaries, (b) Nozzle geometry, and (c) fluid dynamic boundaries.

Figure A-1(a) shows electrostatic boundaries. The electric potentials of the boundaries were given by $V=V_{(applied,\ top,\ bottom)}$. Blue line indicates high voltage ($\underline{V_{applied}}$) applied. On the other hand, the potentials at the top and bottom boundary (red and green line), the electric potential was set to change according to distance due to interference with the neighboring nozzles. Therefore, the electric potential (V_{top} and V_{bottom}) was calculated using the results of multi-nozzle array in **Figure A-1**(b) and (c). The electric potential values are given in **Figure A-1**(a). The zero-charge boundary at outermost side of the model was set by

$$\mathbf{n} \cdot \mathbf{D} = 0 ,$$

The boundaries related to fluid dynamics are in **Figure A-1**(c). The wall boundary (blue line) is given by

$$\mathbf{u} = 0 ,$$

The outlet condition was modeled by,

$$\left[-p\mathbf{I} + \mu\left(\nabla\mathbf{u} + \left(\nabla\mathbf{u} \right)^{T} \right) \right] \mathbf{n} = -p_0 \mathbf{n} ,$$

where gauge pressure (p_o) was set 0 Pa and backflow was suppressed.

The inlet boundary for polymer melt was modeld by,

$$U_p = \frac{-(r+2)(r-2)}{24\pi}$$

For hot air,

$$U_{air} = \frac{-375 V_{air} (r-3)(r-5)}{2\pi}$$

where r indicates distance from the center axis and V_{air} is adjusted for proper velocity of air at the nozzle tip.

Governing equation and boundary condition of electrospinning process simulation

Polymer solution in simulation was assumed to be Newtonian and incompressible

fluid. The velocities and densities of fluids were calculated using Narvier-Stokes equation.[251, 252]

$$\rho \frac{\partial u}{\partial t} + \rho(u \cdot \nabla)u = \nabla \cdot \left[-pI + \mu(\nabla u + (\nabla u)^T) \right] + \rho g + F_{st} + F_e$$

$$\nabla \cdot u = 0$$

$$\frac{\partial \phi}{\partial t} + u \cdot \nabla \phi = \gamma \nabla \cdot \left(h \nabla \phi - \phi(1-\phi) \cdot n \right)$$

Where ρ, μ, g, I, h, ϕ, p, γ and u represent the density, dynamic viscosity, gravitational acceleration constant, identity matrix, interface thickness, level set variable, pressure, re-initialization parameter, and velocity, respectively. The liquid-gas interface was treated using a level-set equation. Density and dynamic viscosity of the fluid were defined using level set functions

$$\rho = \phi \rho_{Polymer} + (1 - \phi) \rho_{Air}$$

And

$$\mu = \phi \mu_{Polymer} + (1 - \phi) \mu_{Air}$$

respectively.

The surface force (F_{st}) is defined as

$$F_{st} = \nabla \cdot (\sigma (I - (nn^T))\delta),$$

where σ and δ are the surface tension coefficient and Dirac delta function to

calculate the force acting on the interface. The volumetric electric force (F_e) is derived from the electrostatic Maxwell stress tensor.

$$T_e = \varepsilon\left(EE - \frac{E^2}{2} I \right)$$

$$F_e = \nabla \cdot T_e = \rho_e E - \frac{E^2}{2}\nabla\varepsilon$$

ε is electrical permittivity which was also calculated using level-set function, $\varepsilon = \phi\varepsilon_{Polymer} + (1-\phi)\varepsilon_{Air}$, E is the electric field and ρ_e is the volumetric charge density.

The electrical forces due to accumulation of free charges in dielectric solution ($f_s^{E,s}$) and ionic charges ($f_s^{E,c}$) at the interface are defined as follows respectively.[284]

We implemented the forces from free surface charge from dielectric material and surface charge from ionic charges. At given experimental condition, ionic charges can move because the electric field strength is enough for charge conduction between the external materials.

$$f_s^{E,d} = \frac{\varepsilon_0}{2}\left(\frac{(D\cdot\mathbf{n})^2}{{\varepsilon_0}^2}\left(\frac{1}{\varepsilon_{polymer}} - \frac{1}{\varepsilon_{air}} \right) - (\mathbf{E}\cdot\mathbf{t})^2(\varepsilon_{polymer} - \varepsilon_{air}) \right)\mathbf{n}\delta$$

$$f_s^{E,c} = \frac{\varepsilon_0}{2}\left((\mathbf{J}\cdot\mathbf{n})^2\left(\frac{\varepsilon_{polymer}}{\sigma_{polymer}^2} - \frac{\varepsilon_{air}}{\sigma_{air}^2} \right) - (\mathbf{E}\cdot\mathbf{t})^2(\varepsilon_{polymer} - \varepsilon_{Air}) \right)\mathbf{n}\delta$$

$$+\varepsilon_0(\mathbf{J}\cdot\mathbf{n})\left(\frac{\varepsilon_{polymer}}{\sigma_{polymer}}-\frac{\varepsilon_{air}}{\sigma_{air}}\right)(\mathbf{E}\cdot\mathbf{t})\mathbf{t}\delta$$

Where ε_0, D, $\mathbf{J}$, $\boldsymbol{n}$ and $\boldsymbol{t}$ are the vacuum permittivity, electric displacement, current density, interface normal and tangential unit vector, respectively. The electrical displacement D becomes,

$$\nabla D = \rho_t - \rho_b = \rho_e = \varepsilon_0 \varepsilon_r E$$

Where ρ_t is total volumetric charge density and ρ_b is bonded charge density. And the current density due to the ionic conduction and migration is

$$J = \rho_i (K_i E + u)$$

Where ρ_i is charge density due to ionic species and K_i is mobility of charged species. Then the conductivity K is described as

$$\rho_i K_i = K$$

The charge conduction and convection during the electrospinning process were calculated by the charge conservation law.

$$\frac{\partial \rho_e}{\partial t} + \nabla \cdot (\rho_e u) = -\frac{K}{\varepsilon}\rho_e$$

Where K is the electric conductivity of the fluid defined using level-set function.

$$(K = \phi K_{Polymer} + (1-\phi) K_{Air})$$

Finally, Gauss's law was adopted to calculated electrical field strength and distribution.

$$\nabla \cdot (\varepsilon E) = \rho_e, \quad E = -\nabla V$$

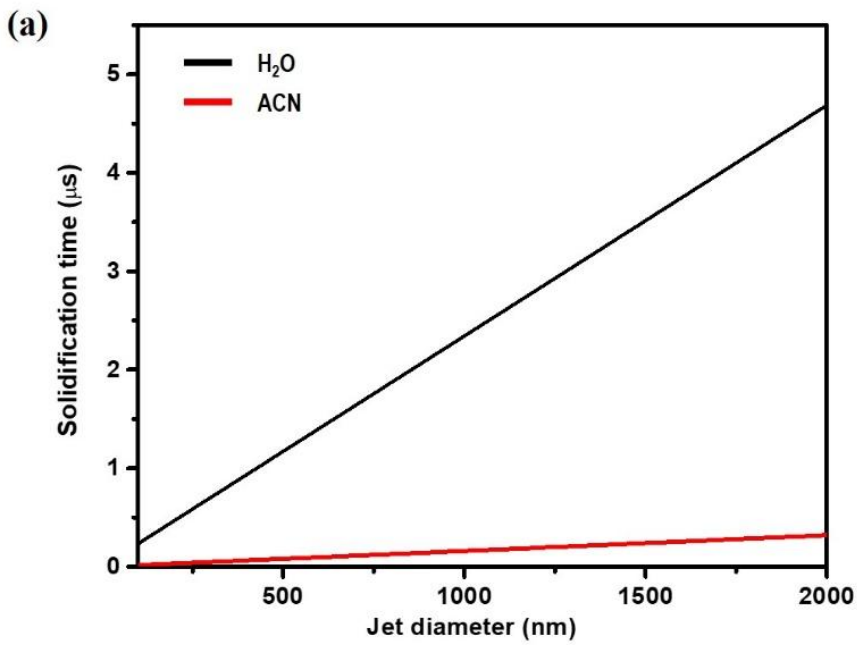

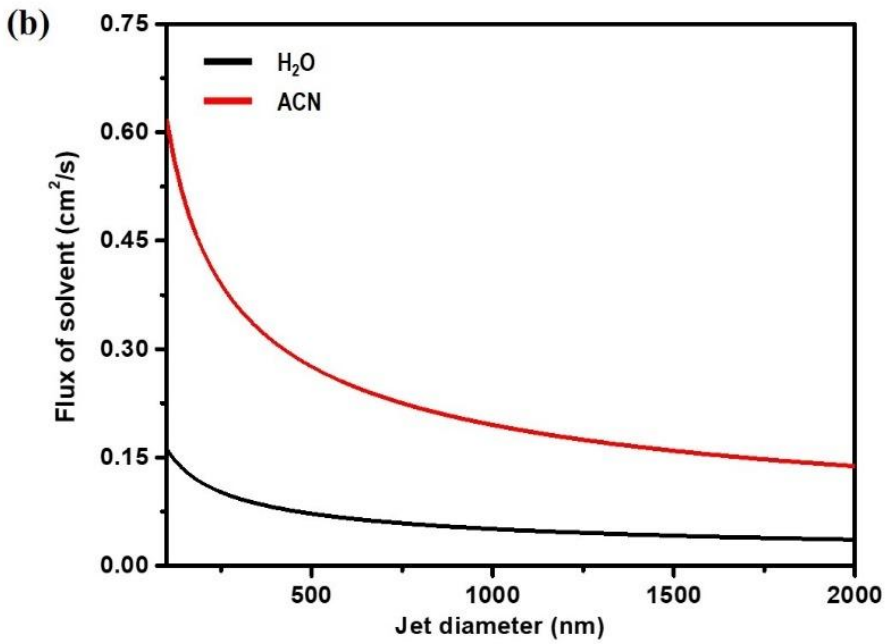

Figure A-2 (a) Calculated solidification time scale and (b) flux of solvent, at the surface of the jet according to jet diameter. The black and red line indicate solvents, H_2O and ACN respectively.

Based on the experimental and theoretical analysis, we proposed a model of formation of helical fibers using electrospinning process focused on the solidification position of the jet. As shown in **Figure A-3**, according to solidification position of the jet, the final fiber morphologies can be varied. When solidification of the surface of the jet occurred at the end whipping, the fibers gets thinner and shows straight structure due to strong elongation by whipping motion. On the other hand, when the solidification occurred before the evolution of the bending instability, the jet can maintain their initial deformation. The solidification of the jet enhanced by

using high vapor pressure solvent or reducing the jet diameter. We accelerated the reduction of the jet diameter by adding large amount of metal ion salt in polymer solution in this study. As the position is close to the nozzle tip, the structure becomes more twisted rather than spiral.

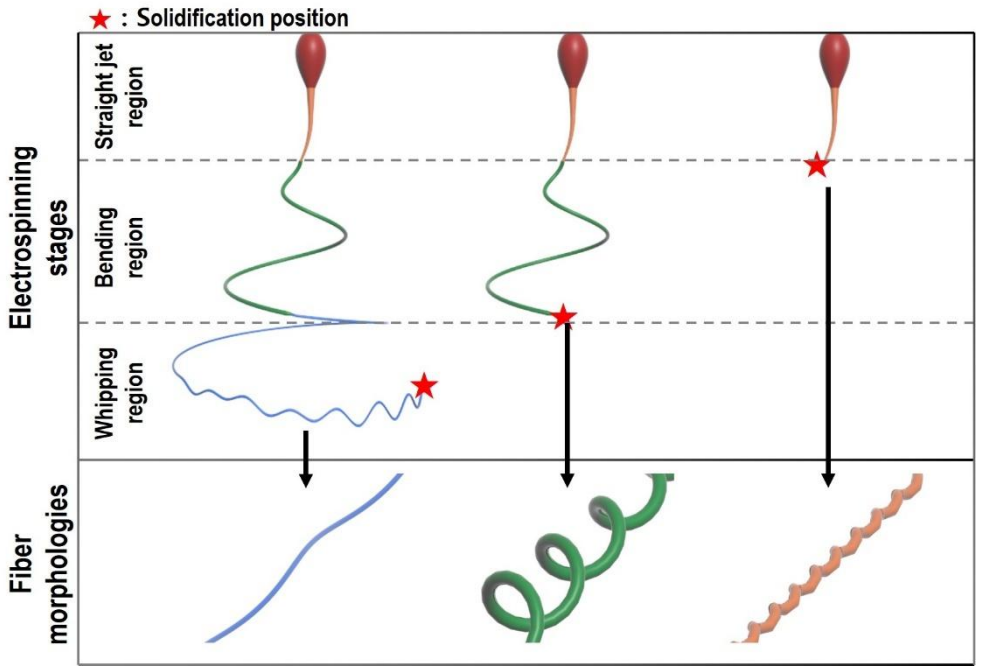

Figure A-3 Illustration of the fiber morphologies according to solidification position of electrospun jet.

Table A-1 Abbreviation

Abbreviations	Full names
AcAc	Acetylacetonate
BA	Benzoic acid
CA	Cellulose acetate

Cisplatin	Cis-Diammineplatinum(II) dichloride
CMC	Carboxymethyl cellulose
CVL:BPA	Crystal violet lactone : bisphenol A
DCM	Dichloromethane
DMAc	*N,N*-dimethylacetamide
DMF	*N,N*-dimethylformamide
DMSO	Dimethyl sulfoxide
DSSCs	Dye-sensitized solar cells
Finite-element method	FEM
HD	Hexadecane
HFIP	1,1,1,3,3,3-hexafluoro-2-propanol
KAB	Keyacid Blue
KAU	Keyacid Uranine
MWNTs	Multiwalled carbon nanotubes
NPs	Nanoparticles
P3HT:PCBM	Poly(3-hexylthiophene):phenyl-C61-butyric acid methyl ester
PAN	Poly(acrylonitrile)
PANI	Polyaniline
PAT	Poly(2-aminothiazole)
PBS	Poly(butyl acrylate-co-styrene)
PC	Poly(caprolactone)
PCL	Poly(caprolactone)
PEDOT:PSS	Poly(3,4-ethylenedioxythiophene) polystyrene sulfonate
PEG	Polyethylene glycol (PEG)
PEO	Polyethylene oxide
Phen	Phenanthroline
PLA	Polylactic acid
PLLA	Poly(L-lactic acid)

PMMA	Poly(methyl methacrylate)
Poly(NIPAAm-co-NMA)	Poly(N-isopropylacrylamide-co-N-methylolacrylamide)
PS	Polystyrene
PS	Polystyrene
PU	Polyurethane
PVA	Poly(vinyl alcohol)
PVAc	Polyvinyl acetate
PVDF	Poly(vinylidenefluoride)
PVDF-HFP	Poly(vinylidenefluoride-co-hexa fluoro propylene)
PVP	Poly(vinylpyrrolidone)
SA	Stearic acid
SAN	Styrene-co-acrylonitrile
SDS	Sodium dodecyl sulfate
SIP	Self-immolative polymer
Teflon® AF	Teflon amorphous fluoropolymer
TFA	Trifluoroacetic acid
TFE	2,2,2-trifluoroethanol
THF	Tetrahydrofuran

Table A-2 Material properties of PCO and crosslinked PCO

	PCO	Crosslinked PCO
Molecular weight (g/mol)	142,750	N/A
PDI	1.88	N/A
T_m (°C)	54	275 (degration)
T_g (°C)	-65	64.2

Crystallinity (%)	30	24.1

Reference

1. Cooley, J.F., *Apparatus for electrically dispersing fluids*. 1902, Google Patents.
2. Teo, W.E. and S.J.N. Ramakrishna, *A review on electrospinning design and nanofibre assemblies.* 2006. **17**(14): p. R89.
3. Reneker, D.H. and I.J.N. Chun, *Nanometre diameter fibres of polymer, produced by electrospinning.* 1996. **7**(3): p. 216.
4. Ali, A.A., M.J.C.P.A.A.S. El-Hamid, and Manufacturing, *Electro-spinning optimization for precursor carbon nanofibers.* 2006. **37**(10): p. 1681-1687.
5. Ruiz-Rosas, R., et al., *The production of submicron diameter carbon fibers by the electrospinning of lignin.* 2010. **48**(3): p. 696-705.
6. Fridrikh, S.V., et al., *Controlling the fiber diameter during electrospinning.* 2003. **90**(14): p. 144502.
7. Deitzel, J.M., et al., *The effect of processing variables on the morphology of electrospun nanofibers and textiles.* 2001. **42**(1): p. 261-272.
8. Lim, C., E. Tan, and S.J.A.P.L. Ng, *Effects of crystalline morphology on the tensile properties of electrospun polymer nanofibers.* 2008. **92**(14): p. 141908.
9. Zhou, Z., et al., *Development of carbon nanofibers from aligned electrospun polyacrylonitrile nanofiber bundles and characterization of their microstructural, electrical, and mechanical properties.* 2009. **50**(13): p. 2999-3006.
10. Visser, J., et al., *Nat Commun. 2015; 6 Huang ZM, Zhang YZ, Kotaki M, Ramakrishna S.* 2003. **63**: p. 2223.
11. McKee, M.G., et al., *Correlations of solution rheology with electrospun fiber formation of linear and branched polyesters.* 2004. **37**(5): p. 1760-1767.
12. Tiwari, S.K., S.S.J.M.S. Venkatraman, and E. C, *Importance of viscosity parameters in electrospinning: Of monolithic and core–shell fibers.* 2012. **32**(5): p. 1037-1042.
13. Gupta, P., et al., *Electrospinning of linear homopolymers of poly (methyl*

methacrylate): exploring relationships between fiber formation, viscosity, molecular weight and concentration in a good solvent. 2005. **46**(13): p. 4799-4810.

14. Zhmayev, E., H. Zhou, and Y.L. Joo, *Modeling of non-isothermal polymer jets in melt electrospinning.* Journal of Non-Newtonian Fluid Mechanics, 2008. **153**(2-3): p. 95-108.
15. Collins, G., et al., *Charge generation, charge transport, and residual charge in the electrospinning of polymers: a review of issues and complications.* 2012. **111**(4): p. 044701.
16. Dalton, P.D., et al., *Direct in vitro electrospinning with polymer melts.* 2006. **7**(3): p. 686-690.
17. Sun, Z., et al., *Compound core–shell polymer nanofibers by co-electrospinning.* 2003. **15**(22): p. 1929-1932.
18. He, M., et al., *Fibrous guided tissue regeneration membrane loaded with anti-inflammatory agent prepared by coaxial electrospinning for the purpose of controlled release.* 2015. **335**: p. 121-129.
19. Zamani, M., M.P. Prabhakaran, and S.J.I.j.o.n. Ramakrishna, *Advances in drug delivery via electrospun and electrosprayed nanomaterials.* 2013. **8**: p. 2997.
20. Shami, Z., et al., *Triple Axial Coelectrospun Multifunctional Double-Shell TiO2@ ZnO Carbon Hollow Nanofibrous Mat Transformed to C-Attached TiO2 Brush-Like Nanotube Arrays: An Mo6+ Adsorbent Nonwoven Mat.* 2014. **53**(39): p. 14963-14973.
21. Chen, Y., et al., *Triple-coaxial electrospun amorphous carbon nanotubes with hollow graphitic carbon nanospheres for high-performance Li ion batteries.* 2012. **5**(7): p. 7898-7902.
22. Lee, B.-S., H.-S. Yang, and W.-R.J.N. Yu, *Fabrication of double-tubular carbon nanofibers using quadruple coaxial electrospinning.* 2014. **25**(46): p. 465602.
23. Yang, H.-S., et al., *Fabrication of carbon nanofibers with Si nanoparticle-stuffed cylindrical multi-channels via coaxial electrospinning and their anodic performance.* 2014. **4**(88): p. 47389-47395.
24. Nguyen, T.T.T., O.H. Chung, and J.S.J.C.P. Park, *Coaxial electrospun poly*

(lactic acid)/chitosan (core/shell) composite nanofibers and their antibacterial activity. 2011. **86**(4): p. 1799-1806.

25. Nguyen, T.T.T., et al., *Porous core/sheath composite nanofibers fabricated by coaxial electrospinning as a potential mat for drug release system.* 2012. **439**(1-2): p. 296-306.
26. Khorshidi, S., et al., *A review of key challenges of electrospun scaffolds for tissue-engineering applications.* 2016. **10**(9): p. 715-738.
27. Yu, Y., et al., *Encapsulation of Sn@ carbon nanoparticles in bamboo-like hollow carbon nanofibers as an anode material in lithium-based batteries.* 2009. **48**(35): p. 6485-6489.
28. Kumar, P.S., et al., *Hierarchical electrospun nanofibers for energy harvesting, production and environmental remediation.* 2014. **7**(10): p. 3192-3222.
29. Qu, H., S. Wei, and Z.J.J.o.M.C.A. Guo, *Coaxial electrospun nanostructures and their applications.* 2013. **1**(38): p. 11513-11528.
30. Chen, M., et al., *Electrospinning of calixarene-functionalized polyacrylonitrile nanofiber membranes and application as an adsorbent and catalyst support.* 2013. **29**(38): p. 11858-11867.
31. Kurban, Z., et al., *A solution selection model for coaxial electrospinning and its application to nanostructured hydrogen storage materials.* 2010. **114**(49): p. 21201-21213.
32. Li, D. and Y.J.N.l. Xia, *Direct fabrication of composite and ceramic hollow nanofibers by electrospinning.* 2004. **4**(5): p. 933-938.
33. Xu, Y., et al., *Influence of the drug distribution in electrospun gliadin fibers on drug-release behavior.* 2017. **106**: p. 422-430.
34. Wang, Q., et al., *Electrospun hypromellose-based hydrophilic composites for rapid dissolution of poorly water-soluble drug.* 2017. **174**: p. 617-625.
35. Reneker, D.H., et al., *Bending instability of electrically charged liquid jets of polymer solutions in electrospinning.* 2000. **87**(9): p. 4531-4547.
36. Zuo, W., et al., *Experimental study on relationship between jet instability and formation of beaded fibers during electrospinning.* 2005. **45**(5): p. 704-709.
37. Carroll, C.P. and Y.L. Joo, *Axisymmetric instabilities in electrospinning of*

highly conducting, viscoelastic polymer solutions. 2009. **21**(10): p. 103101.

38. Li, F., X.-Y. Yin, and X.-Z. Yin, *Axisymmetric and non-axisymmetric instability of an electrified viscous coaxial jet.* Journal of Fluid Mechanics, 2009. **632**: p. 199-225.
39. Li, F., X.-Y. Yin, and X.-Z. Yin, *Axisymmetric and non-axisymmetric instability of an electrically charged viscoelastic liquid jet.* Journal of Non-Newtonian Fluid Mechanics, 2011. **166**(17): p. 1024-1032.
40. Li, F., X.-Y. Yin, and X.-Z. Yin, *Linear instability of a coflowing jet under an axial electric field.* Physical Review E, 2006. **74**(3): p. 036304.
41. Anton, F., *Production of artificial fibers*. 1937, Google Patents.
42. Zhou, F.L., R.H. Gong, and I. Porat, *Polymeric nanofibers via flat spinneret electrospinning.* Polymer Engineering & Science, 2009. **49**(12): p. 2475-2481.
43. Thoppey, N.M., et al., *Unconfined fluid electrospun into high quality nanofibers from a plate edge.* Polymer, 2010. **51**(21): p. 4928-4936.
44. Wu, D., et al., *High throughput tip-less electrospinning via a circular cylindrical electrode.* J Nanosci Nanotechnol, 2010. **10**(7): p. 4221-6.
45. Forward, K.M., A. Flores, and G.C. Rutledge, *Production of core/shell fibers by electrospinning from a free surface.* Chemical Engineering Science, 2013. **104**: p. 250-259.
46. Rahimi, M. and J. Mokhtari, *Fabrication of thermo-regulating hexadecane-polyurethane core-shell composite nanofibrous mat as advanced technical layer: Effect of coaxial nozzle geometry.* Journal of Industrial Textiles, 2016. **47**(6): p. 1134-1151.
47. Lee, B.-S., et al., *New Electrospinning Nozzle to Reduce Jet Instability and Its Application to Manufacture of Multi-layered Nanofibers.* Scientific Reports, 2014. **4**(1): p. 6758.
48. Yu, D.-G., et al., *Improving Polymer Nanofiber Quality Using a Modified Co-axial Electrospinning Process.* 2011. **32**(9-10): p. 744-750.
49. Reznik, S.N., et al., *Transient and steady shapes of droplets attached to a surface in a strong electric field.* Journal of Fluid Mechanics, 2004. **516**: p. 349-377.
50. Reznik, S.N., et al., *Evolution of a compound droplet attached to a core-*

shell nozzle under the action of a strong electric field. Physics of Fluids, 2006. **18**(6): p. 062101.

51. Kaerkitcha, N., S. Chuangchote, and T. Sagawa, *Control of physical properties of carbon nanofibers obtained from coaxial electrospinning of PMMA and PAN with adjustable inner/outer nozzle-ends.* Nanoscale Res Lett, 2016. **11**(1): p. 186.
52. Tong, X. and X. Bin-Jie, *Preparation and characterization of coaxial electrospun polysulfone amide/polyurethane.* Journal of Industrial Textiles, 2016. **46**(8): p. 1581-1597.
53. Wu, H., et al., *Effects of Electric Field and Polymer Structure on the Formation of Helical Nanofibers via Coelectrospinning.* Industrial & Engineering Chemistry Research, 2015. **54**(39): p. 9585-9590.
54. Kaerkitcha, N., et al., *Influence of the viscosity ratio of polyacrylonitrile/poly(methyl methacrylate) solutions on core–shell fibers prepared by coaxial electrospinning.* Polymer Journal, 2017. **49**(6): p. 497-502.
55. Halaui, R., et al., *Polymeric microtubes for water filtration by co-axial electrospinning technique.* Polymers for Advanced Technologies, 2017. **28**(5): p. 570-582.
56. Zhou, Z., et al., *Needleless emulsion electrospinning for scalable fabrication of core-shell nanofibers.* Journal of Applied Polymer Science, 2014. **131**(20): p. n/a-n/a.
57. Yu, D.-G., et al., *Electrospinning of Concentrated Polymer Solutions.* Macromolecules, 2010. **43**(24): p. 10743-10746.
58. Yan, J. and D.-G. Yu, *Smoothening electrospinning and obtaining high-quality cellulose acetate nanofibers using a modified coaxial process.* Journal of Materials Science, 2012. **47**(20): p. 7138-7147.
59. Huang, W., et al., *Drug-loaded zein nanofibers prepared using a modified coaxial electrospinning process.* AAPS PharmSciTech, 2013. **14**(2): p. 675-81.
60. Yu, D.G., et al., *Modified coaxial electrospinning for the preparation of high-quality ketoprofen-loaded cellulose acetate nanofibers.* Carbohydr Polym, 2012. **90**(2): p. 1016-23.

61. Xie, J., et al., *Highly stable coated polyvinylpyrrolidone nanofibers prepared using modified coaxial electrospinning.* Fibers and Polymers, 2014. **15**(1): p. 78-83.
62. Yu, D.-G., et al., *Linear drug release membrane prepared by a modified coaxial electrospinning process.* Journal of Membrane Science, 2013. **428**: p. 150-156.
63. Yang, J.-M. and D.-G. Yu, *Co-axial electrospinning with sodium thiocyanate solution for preparing polyacrylonitrile nanofibers.* Journal of Polymer Research, 2012. **19**(2): p. 9789.
64. Yu, D.G., et al., *Polyacrylonitrile nanofibers prepared using coaxial electrospinning with LiCl solution as sheath fluid.* Nanotechnology, 2011. **22**(43): p. 435301.
65. Yu, D.G., et al., *Polyacrylonitrile nanofibers coated with silver nanoparticles using a modified coaxial electrospinning process.* Int J Nanomedicine, 2012. **7**: p. 5725-32.
66. Guenthner, A.J., et al., *Dynamics of Hollow Nanofiber Formation During Solidification Subjected to Solvent Evaporation.* Macromolecular Theory and Simulations, 2006. **15**(1): p. 87-93.
67. Dayal, P. and T. Kyu, *Porous fiber formation in polymer-solvent system undergoing solvent evaporation.* Journal of Applied Physics, 2006. **100**(4): p. 043512.
68. Li, F., X.-Y. Yin, and X.-Z. Yin, *Instability analysis of a coaxial jet under a radial electric field in the nonequipotential case.* Physics of Fluids, 2006. **18**(3): p. 037101.
69. Li, F., X.-Y. Yin, and X.-Z. Yin, *Linear instability analysis of an electrified coaxial jet.* Physics of Fluids, 2005. **17**(7): p. 077104.
70. Li, F., X.-Y. Yin, and X.-Z. Yin, *Instability analysis of an inner-driving coaxial jet inside a coaxial electrode for the non-equipotential case.* Journal of Electrostatics, 2008. **66**(1-2): p. 58-70.
71. Fong, H. and D.H. Reneker, *Elastomeric nanofibers of styrene–butadiene–styrene triblock copolymer.* Journal of Polymer Science Part B: Polymer Physics, 1999. **37**(24): p. 3488-3493.
72. Babapoor, A., G. Karimi, and M. Khorram, *Fabrication and characterization*

of nanofiber-nanoparticle-composites with phase change materials by electrospinning. Applied Thermal Engineering, 2016. **99**: p. 1225-1235.

73. Chronakis, I.S., S. Grapenson, and A. Jakob, *Conductive polypyrrole nanofibers via electrospinning: electrical and morphological properties.* Polymer, 2006. **47**(5): p. 1597-1603.
74. Ju, Y.-W., et al., *Electrochemical properties of electrospun PAN/MWCNT carbon nanofibers electrodes coated with polypyrrole.* Electrochimica Acta, 2008. **53**(19): p. 5796-5803.
75. Yang, R., et al., *Bubble-electrospinning for fabricating nanofibers.* Polymer, 2009. **50**(24): p. 5846-5850.
76. Huang, C., et al., *Electrospun polymer nanofibres with small diameters.* Nanotechnology, 2006. **17**(6): p. 1558.
77. Ramakrishna, S., et al., *Electrospun nanofibers: solving global issues.* Materials today, 2006. **9**(3): p. 40-50.
78. Karuppuswamy, P., et al., *Polycaprolactone nanofibers for the controlled release of tetracycline hydrochloride.* Materials Letters, 2015. **141**: p. 180-186.
79. Zhang, X., et al., *Electrospun nanofiber-based anodes, cathodes, and separators for advanced lithium-ion batteries.* Polymer Reviews, 2011. **51**(3): p. 239-264.
80. Jayaprakash, N., et al., *Porous hollow carbon@ sulfur composites for high-power lithium–sulfur batteries.* Angewandte Chemie International Edition, 2011. **50**(26): p. 5904-5908.
81. Zhou, F.-L., et al., *Jet deposition in near-field electrospinning of patterned polycaprolactone and sugar-polycaprolactone core–shell fibres.* Polymer, 2011. **52**(16): p. 3603-3610.
82. Lee, B.-S., et al., *An effective method for manufacturing hollow carbon nanofibers and microstructural analysis.* Macromolecular Research, 2012. **20**(6): p. 605-613.
83. Na, H., et al., *Fabrication of PVDF/PVA microtubules by coaxial electrospinning.* Polymer, 2012. **53**(13): p. 2736-2743.
84. Pakravan, M., M.C. Heuzey, and A. Ajji, *Core-shell structured PEO-chitosan nanofibers by coaxial electrospinning.* Biomacromolecules, 2012. **13**(2): p.

412-21.

85. Zhou, F.L., et al., *Coaxially electrospun axon-mimicking fibers for diffusion magnetic resonance imaging.* ACS Appl Mater Interfaces, 2012. **4**(11): p. 6311-6.

86. Ji, X., et al., *Polyelectrolyte Doped Hollow Nanofibers for Positional Assembly of Bienzyme System for Cascade Reaction at O/W Interface.* ACS Catalysis, 2014. **4**(12): p. 4548-4559.

87. Huang, Y.-S., et al., *Novel highly aligned, double-layered, hollow fibrous polycarbonate membranes with a perfectly tightly packed pentagonal pore structure fabricated using the electrospinning process.* RSC Advances, 2015. **5**(108): p. 88857-88865.

88. Khalf, A., K. Singarapu, and S.V. Madihally, *Cellulose acetate core–shell structured electrospun fiber: fabrication and characterization.* Cellulose, 2015. **22**(2): p. 1389-1400.

89. Huang, J., et al., *Macromol. Mater. Eng. 11/2016.* Macromolecular Materials and Engineering, 2016. **301**(11): p. 1281-1281.

90. Lee, B.S., et al., *Novel multi-layered 1-D nanostructure exhibiting the theoretical capacity of silicon for a super-enhanced lithium-ion battery.* Nanoscale, 2014. **6**(11): p. 5989-98.

91. Han, D. and A.J. Steckl, *Triaxial electrospun nanofiber membranes for controlled dual release of functional molecules.* ACS Appl Mater Interfaces, 2013. **5**(16): p. 8241-5.

92. Isaacoff, B.P. and K.A. Brown, *Progress in Top-Down Control of Bottom-Up Assembly.* Nano Lett, 2017. **17**(11): p. 6508-6510.

93. Tharakan, J.P. and P.C. Chau, *Operation and pressure distribution of immobilized cell hollow fiber bioreactors.* Biotechnol Bioeng, 1986. **28**(7): p. 1064-71.

94. Feng, C., et al., *Preparation and characterization of electro-spun nanofiber membranes and their possible applications in water treatment.* Separation and Purification Technology, 2013. **102**: p. 118-135.

95. Liu, S., et al., *Coaxial electrospinning route to prepare Au-loading SnO2 hollow microtubes for non-enzymatic detection of H2O2.* Electrochimica Acta, 2014. **141**: p. 161-166.

96. Xiaoqiang, L., et al., *Fabrication and properties of core-shell structure P(LLA-CL) nanofibers by coaxial electrospinning.* Journal of Applied Polymer Science, 2009. **111**(3): p. 1564-1570.
97. Lallave, M., et al., *Filled and hollow carbon nanofibers by coaxial electrospinning of alcell lignin without binder polymers.* Advanced Materials, 2007. **19**(23): p. 4292-4296.
98. Loscertales, I.G., et al., *Electrically forced coaxial nanojets for one-step hollow nanofiber design.* J Am Chem Soc, 2004. **126**(17): p. 5376-7.
99. Zussman, E., et al., *Electrospun Polyaniline/Poly(methyl methacrylate)-Derived Turbostratic Carbon Micro-/Nanotubes.* 2006. **18**(3): p. 348-353.
100. Ou, K.-L., et al., *Membranes of epitaxial-like packed, super aligned electrospun micron hollow poly(l-lactic acid) (PLLA) fibers.* European Polymer Journal, 2011. **47**(5): p. 882-892.
101. Lee, B.-S., et al., *Novel multi-layered 1-D nanostructure exhibiting the theoretical capacity of silicon for a super-enhanced lithium-ion battery.* Nanoscale, 2014. **6**(11): p. 5989-5998.
102. Choi, S.-J., et al., *Coaxial electrospinning of WO 3 nanotubes functionalized with bio-inspired Pd catalysts and their superior hydrogen sensing performance.* Nanoscale, 2016. **8**(17): p. 9159-9166.
103. Steinhart, M., et al., *Palladium nanotubes with tailored wall morphologies.* Advanced Materials, 2003. **15**(9): p. 706-709.
104. Hang, Y., et al., *Preparation of regenerated silk fibroin/silk sericin fibers by coaxial electrospinning.* Int J Biol Macromol, 2012. **51**(5): p. 980-6.
105. Lee, G.H., J.-C. Song, and K.-B. Yoon, *Controlled wall thickness and porosity of polymeric hollow nanofibers by coaxial electrospinning.* Macromolecular Research, 2010. **18**(6): p. 571-576.
106. Moghe, A. and B. Gupta, *Co-axial electrospinning for nanofiber structures: preparation and applications.* Polymer Reviews, 2008. **48**(2): p. 353-377.
107. Absar, S., et al., *Investigation of synthesis and processing of cellulose, cellulose acetate and poly (ethylene oxide) nanofibers incorporating anti-cancer/tumor drug cis-diammineplatinum (II) dichloride using electrospinning techniques.* Journal of Polymer Engineering, 2015. **35**(9): p. 867-878.

108. Jiang, S., et al., *Highly flexible and tough concentric triaxial polystyrene fibers.* ACS Appl Mater Interfaces, 2014. **6**(8): p. 5918-23.
109. Kamperman, M., et al., *Nanomanufacturing of continuous composite nanofibers with confinement-induced morphologies.* Polymer Chemistry, 2010. **1**(7): p. 1001-1004.
110. Kalra, V., et al., *Controlling nanoparticle location via confined assembly in electrospun block copolymer nanofibers.* Small, 2008. **4**(11): p. 2067-73.
111. Yu, B., et al., *Confinement-induced novel morphologies of block copolymers.* Phys Rev Lett, 2006. **96**(13): p. 138306.
112. Yu, B., et al., *Confinement-induced morphologies of cylinder-forming asymmetric diblock copolymers.* Macromolecules, 2008. **41**(11): p. 4042-4054.
113. Lu, Y., et al., *Coaxial electrospun fibers: applications in drug delivery and tissue engineering.* Wiley Interdiscip Rev Nanomed Nanobiotechnol, 2016. **8**(5): p. 654-77.
114. Ji, L. and X. Zhang, *Electrospun carbon nanofibers containing silicon particles as an energy-storage medium.* Carbon, 2009. **47**(14): p. 3219-3226.
115. Li, D., Y. Wang, and Y. Xia, *Electrospinning of polymeric and ceramic nanofibers as uniaxially aligned arrays.* Nano letters, 2003. **3**(8): p. 1167-1171.
116. Zhang, H., et al., *Electrospun core–shell silicon/carbon fibers with an internal honeycomb-like conductive carbon framework as an anode for lithium ion batteries.* Journal of Materials Chemistry A, 2015. **3**(13): p. 7112-7120.
117. Yu, D.G., et al., *Solid dispersions in the form of electrospun core-sheath nanofibers.* Int J Nanomedicine, 2011. **6**: p. 3271-80.
118. Lin, X., et al., *Enhanced electric displacement induces large energy density in polymer nanocomposites containing core–shell structured BaTiO 3@ TiO 2 nanofibers.* Journal of Materials Chemistry A, 2016. **4**(6): p. 2314-2320.
119. Pan, Z., J. Zhai, and B. Shen, *Multilayer hierarchical interfaces with high energy density in polymer nanocomposites composed of BaTiO 3@ TiO*

2@ Al 2 O 3 nanofibers. Journal of Materials Chemistry A, 2017. **5**(29): p. 15217-15226.

120. Esmaeili, A. and M. Haseli, *Electrospinning of thermoplastic carboxymethyl cellulose/poly (ethylene oxide) nanofibers for use in drug-release systems.* Materials Science and Engineering: C, 2017. **77**: p. 1117-1127.
121. Zhu, J., et al., *Aqueous-Based Coaxial Electrospinning of Genetically Engineered Silk Elastin Core-Shell Nanofibers.* Materials (Basel), 2016. **9**(4): p. 221.
122. Lee, B.-S., et al., *Fabrication of Si core/C shell nanofibers and their electrochemical performances as a lithium-ion battery anode.* Journal of Power Sources, 2012. **206**: p. 267-273.
123. Zhao, Y., X. Cao, and L. Jiang, *Bio-mimic multichannel microtubes by a facile method.* J Am Chem Soc, 2007. **129**(4): p. 764-5.
124. Yu, D.-G., et al., *High-quality Janus nanofibers prepared using three-fluid electrospinning.* Chemical Communications, 2017. **53**(33): p. 4542-4545.
125. Xue, J., et al., *Electrospinning and electrospun nanofibers: methods, materials, and applications.* Chemical reviews, 2019. **119**(8): p. 5298-5415.
126. Peng, S., et al., *Electrospun carbon nanofibers and their hybrid composites as advanced materials for energy conversion and storage.* Nano Energy, 2016. **22**: p. 361-395.
127. Deng, L., et al., *Carbon nanofibres produced from electrospun cellulose nanofibres.* Carbon, 2013. **58**: p. 66-75.
128. Yang, Y., et al., *Highly porous electrospun polyvinylidene fluoride (PVDF)-based carbon fiber.* Carbon, 2011. **49**(11): p. 3395-3403.
129. Park, S.H., et al., *Preparations of pitch-based CF/ACF webs by electrospinning.* Carbon (New York, NY), 2003. **41**(13): p. 2655-2657.
130. Li, X. and L. Zhi, *Graphene hybridization for energy storage applications.* Chemical Society Reviews, 2018. **47**(9): p. 3189-3216.
131. Mai, L., et al., *Electrospun ultralong hierarchical vanadium oxide nanowires with high performance for lithium ion batteries.* Nano letters, 2010. **10**(11): p. 4750-4755.
132. Liu, X., et al., *Flexible all-fiber electrospun supercapacitor.* Journal of Power Sources, 2018. **384**: p. 264-269.

133. Wu, H., et al., *Electrospun metal nanofiber webs as high-performance transparent electrode.* Nano letters, 2010. **10**(10): p. 4242-4248.
134. Shui, J. and J.C. Li, *Platinum nanowires produced by electrospinning.* Nano letters, 2009. **9**(4): p. 1307-1314.
135. Chen, H.-T., et al., *UV-induced synthesis of silver nanofiber networks as transparent electrodes.* Journal of Materials Chemistry C, 2016. **4**(32): p. 7675-7682.
136. Jeong, S., et al., *High efficiency, transparent, reusable, and active PM2. 5 filters by hierarchical Ag nanowire percolation network*. Nano letters, 2017. **17**(7): p. 4339-4346.
137. Wen, Q., et al., *Flexible inorganic nanofibrous membranes with hierarchical porosity for efficient water purification.* Chemical Science, 2013. **4**(12): p. 4378-4382.
138. Wang, C., et al., *Silk nanofibers as high efficient and lightweight air filter.* Nano Research, 2016. **9**(9): p. 2590-2597.
139. Zhang, Y.S. and Y. Xia, *Multiple facets for extracellular matrix mimicking in regenerative medicine.* Nanomedicine, 2015. **10**(5): p. 689-692.
140. Aamodt, J.M. and D.W. Grainger, *Extracellular matrix-based biomaterial scaffolds and the host response.* Biomaterials, 2016. **86**: p. 68-82.
141. Sun, L., et al., *Enhanced wound healing in diabetic rats by nanofibrous scaffolds mimicking the basketweave pattern of collagen fibrils in native skin.* Biomaterials science, 2018. **6**(2): p. 340-349.
142. Sill, T.J. and H.A. Von Recum, *Electrospinning: applications in drug delivery and tissue engineering.* Biomaterials, 2008. **29**(13): p. 1989-2006.
143. Cui, W., Y. Zhou, and J. Chang, *Electrospun nanofibrous materials for tissue engineering and drug delivery.* Science and technology of advanced materials, 2010. **11**(1): p. 014108.
144. Hwang, T.H., et al., *Electrospun core–shell fibers for robust silicon nanoparticle-based lithium ion battery anodes.* Nano letters, 2012. **12**(2): p. 802-807.
145. Jiang, S., et al., *Electrospun nanofiber reinforced composites: A review.* Polymer Chemistry, 2018. **9**(20): p. 2685-2720.
146. Jung, J.-W., et al., *Electrospun nanofibers as a platform for advanced*

secondary batteries: a comprehensive review. Journal of materials chemistry A, 2016. **4**(3): p. 703-750.

147. Du, P., et al., *TiO2/Nb2O5 core–sheath nanofibers film: Co-electrospinning fabrication and its application in dye-sensitized solar cells.* Electrochemistry communications, 2012. **25**: p. 46-49.
148. Yang, C., et al., *Electrospun pH-sensitive core–shell polymer nanocomposites fabricated using a tri-axial process.* Acta biomaterialia, 2016. **35**: p. 77-86.
149. Muthiah, P., S.H. Hsu, and W. Sigmund, *Coaxially electrospun PVDF-Teflon AF and Teflon AF-PVDF core-sheath nanofiber mats with superhydrophobic properties.* Langmuir, 2010. **26**(15): p. 12483-7.
150. Bedford, N.M., et al., *Nanofiber-Based Bulk-Heterojunction Organic Solar Cells Using Coaxial Electrospinning.* Advanced Energy Materials, 2012. **2**(9): p. 1136-1144.
151. Chen, H., et al., *Nanowire-in-microtube structured core/shell fibers via multifluidic coaxial electrospinning.* Langmuir, 2010. **26**(13): p. 11291-6.
152. Sezer, U.A., et al., *A design achieved by coaxial electrospinning of polysulfone and sulfonated polysulfone as a core-shell structure to optimize mechanical strength and hemocompatibility.* Surfaces and Interfaces, 2018. **10**: p. 176-187.
153. Lin, M.F., et al., *Preparation and properties of thermoresponsive and conductive composite fibers with core-sheath structure.* Journal of Polymer Science Part A: Polymer Chemistry, 2016. **54**(9): p. 1299-1307.
154. An, S., et al., *Highly flexible transparent self-healing composite based on electrospun core-shell nanofibers produced by coaxial electrospinning for anti-corrosion and electrical insulation.* Nanoscale, 2015. **7**(42): p. 17778-85.
155. Qiu, Y., et al., *Preparation of nitrogen-doped carbon submicrotubes by coaxial electrospinning and their electrocatalytic activity for oxygen reduction reaction in acid media.* Electrochimica Acta, 2013. **96**: p. 225-229.
156. Han, D. and A.J. Steckl, *Superhydrophobic and oleophobic fibers by coaxial electrospinning.* Langmuir, 2009. **25**(16): p. 9454-62.

157. Huang, Y.-X., et al., *Coaxially electrospun super-amphiphobic silica-based membrane for anti-surfactant-wetting membrane distillation.* Journal of Membrane Science, 2017. **531**: p. 122-128.
158. Du, P., et al., *A photovoltaic smart textile and a photocatalytic functional textile based on co-electrospun TiO2/MgO core–sheath nanorods: novel textiles of integrating energy and environmental science with textile research.* Textile Research Journal, 2013. **83**(16): p. 1690-1702.
159. Hwang, T.H., et al., *Electrospun core-shell fibers for robust silicon nanoparticle-based lithium ion battery anodes.* Nano Lett, 2012. **12**(2): p. 802-7.
160. Zhang, J., S.-W. Choi, and S.S. Kim, *Micro- and nano-scale hollow TiO2 fibers by coaxial electrospinning: Preparation and gas sensing.* Journal of Solid State Chemistry, 2011. **184**(11): p. 3008-3013.
161. Chang, W., et al., *Fabrication of nanostructured hollow TiO2 nanofibers with enhanced photocatalytic activity by coaxial electrospinning.* Materials Research Bulletin, 2013. **48**(7): p. 2661-2668.
162. Du, P., et al., *Coaxial electrospun TiO2/ZnO core–sheath nanofibers film: Novel structure for photoanode of dye-sensitized solar cells.* Electrochimica Acta, 2012. **78**: p. 392-397.
163. Bui, H.T., et al., *Carbon nanofiber@platinum by a coaxial electrospinning and their improved electrochemical performance as a Li−O2 battery cathode.* Carbon, 2018. **130**: p. 94-104.
164. Huang, B., et al., *Enhanced gas-sensing performance of ZnO@In2O3 core@shell nanofibers prepared by coaxial electrospinning.* Sensors and Actuators B: Chemical, 2018. **255**: p. 2248-2257.
165. Li, F., et al., *Coaxial electrospinning heterojunction SnO2/Au-doped In2O3 core-shell nanofibers for acetone gas sensor.* Sensors and Actuators B: Chemical, 2017. **252**: p. 822-830.
166. Kim, M., et al., *Flexible lateral organic solar cells with core–shell structured organic nanofibers.* Nano Energy, 2015. **18**: p. 97-108.
167. Lee, B.S., et al., *Facile conductive bridges formed between silicon nanoparticles inside hollow carbon nanofibers.* Nanoscale, 2013. **5**(11): p. 4790-6.

168. Shao, H., et al., *Electrospun Flexible Coaxial Nanoribbons Endowed With Tuned and Simultaneous Fluorescent Color-Electricity-Magnetism Trifunctionality.* Sci Rep, 2015. **5**(1): p. 14052.
169. Ma, Q., et al., *Electrospinning fabrication of high-performance magnetic@photoluminescent bifunctional coaxial nanocables.* Chemical Engineering Journal, 2013. **222**: p. 16-22.
170. Pan, Z., et al., *Significantly improved dielectric properties and energy density of polymer nanocomposites via small loaded of BaTiO3 nanotubes.* Composites Science and Technology, 2017. **147**: p. 30-38.
171. Malherbe, I., R.D. Sanderson, and E. Smit, *Reversibly thermochromic micro-fibres by coaxial electrospinning.* Polymer, 2010. **51**(22): p. 5037-5043.
172. Coimbra, P., et al., *Coaxial electrospun PCL/Gelatin-MA fibers as scaffolds for vascular tissue engineering.* Colloids Surf B Biointerfaces, 2017. **159**: p. 7-15.
173. Surucu, S. and H. Turkoglu Sasmazel, *Development of core-shell coaxially electrospun composite PCL/chitosan scaffolds.* Int J Biol Macromol, 2016. **92**: p. 321-328.
174. Zhang, J.-F., et al., *Electrospun Core−Shell Structure Nanofibers from Homogeneous Solution of Poly(ethylene oxide)/Chitosan.* Macromolecules, 2009. **42**(14): p. 5278-5284.
175. Alharbi, H.F., et al., *Fabrication of core-shell structured nanofibers of poly (lactic acid) and poly (vinyl alcohol) by coaxial electrospinning for tissue engineering.* European Polymer Journal, 2018. **98**: p. 483-491.
176. Li, L., et al., *Electrospun hollow nanofibers for advanced secondary batteries.* Nano Energy, 2017. **39**: p. 111-139.
177. Niu, S., et al., *Fabrication of magnetic nanofibers via surface-initiated RAFT polymerization and coaxial electrospinning.* Reactive and Functional Polymers, 2013. **73**(11): p. 1447-1454.
178. Liu, W., et al., *Preliminary study on development of PVDF nanofiber based energy harvesting device for an artery microrobot.* Microelectronic Engineering, 2011. **88**(8): p. 2251-2254.
179. Xia, X., et al., *The effects of electrospinning parameters on coaxial Sn/C nanofibers: Morphology and lithium storage performance.* Electrochimica

Acta, 2014. **121**: p. 345-351.

180. Cui, W., Y. Zhou, and J. Chang, *Electrospun nanofibrous materials for tissue engineering and drug delivery.* Sci Technol Adv Mater, 2010. **11**(1): p. 014108.
181. Hu, X., et al., *Electrospinning of polymeric nanofibers for drug delivery applications.* J Control Release, 2014. **185**: p. 12-21.
182. Liu, H., et al., *Electrospinning of nanofibers for tissue engineering applications. J Nanomater 2013: 1–11*. 2013.
183. Lee, K.Y., et al., *Electrospinning of polysaccharides for regenerative medicine.* Adv Drug Deliv Rev, 2009. **61**(12): p. 1020-32.
184. Khalf, A. and S.V. Madihally, *Recent advances in multiaxial electrospinning for drug delivery.* Eur J Pharm Biopharm, 2017. **112**: p. 1-17.
185. Repanas, A., S. Andriopoulou, and B. Glasmacher, *The significance of electrospinning as a method to create fibrous scaffolds for biomedical engineering and drug delivery applications.* Journal of Drug Delivery Science and Technology, 2016. **31**: p. 137-146.
186. Yoon, J., et al., *Fabrication of a Highly Stretchable, Wrinkle-Free Electrode with Switchable Transparency Using a Free-Standing Silver Nanofiber Network and Shape Memory Polymer Substrate.* Macromolecular Rapid Communications, 2020: p. 2000129.
187. Han, D., et al., *Long-term antimicrobial effect of nisin released from electrospun triaxial fiber membranes.* Acta Biomater, 2017. **53**: p. 242-249.
188. Jiang, H., L. Wang, and K. Zhu, *Coaxial electrospinning for encapsulation and controlled release of fragile water-soluble bioactive agents.* J Control Release, 2014. **193**: p. 296-303.
189. Huang, W., A. Rollett, and D.L. Kaplan, *Silk-elastin-like protein biomaterials for the controlled delivery of therapeutics.* Expert Opin Drug Deliv, 2015. **12**(5): p. 779-91.
190. Han, D., et al., *Stimuli-responsive self-immolative polymer nanofiber membranes formed by coaxial electrospinning.* ACS applied materials & interfaces, 2017. **9**(13): p. 11858-11865.
191. Geng, X., O.H. Kwon, and J. Jang, *Electrospinning of chitosan dissolved in concentrated acetic acid solution.* Biomaterials, 2005. **26**(27): p. 5427-32.

192. Khodkar, F. and N. Golshan Ebrahimi, *Preparation and properties of antibacterial, biocompatible core–shell fibers produced by coaxial electrospinning.* Journal of Applied Polymer Science, 2017. **134**(25).
193. Altman, G.H., et al., *Silk-based biomaterials.* Biomaterials, 2003. **24**(3): p. 401-16.
194. Soares, R.M., et al., *A novel globular protein electrospun fiber mat with the addition of polysilsesquioxane.* Int J Biol Macromol, 2011. **49**(4): p. 480-6.
195. Zhang, Y., et al., *Recent development of polymer nanofibers for biomedical and biotechnological applications.* J Mater Sci Mater Med, 2005. **16**(10): p. 933-46.
196. Yan, J., et al., *Electrospun acid–base pair solid dispersions of quercetin.* RSC Advances, 2014. **4**(102): p. 58265-58271.
197. Yang, G.-Z., et al., *Nanosized sustained-release drug depots fabricated using modified tri-axial electrospinning.* Acta biomaterialia, 2017. **53**: p. 233-241.
198. Kiatyongchai, T., S. Wongsasulak, and T. Yoovidhya, *Coaxial electrospinning and release characteristics of cellulose acetate–gelatin blend encapsulating a model drug.* Journal of Applied Polymer Science, 2014. **131**(8).
199. Li, X.-Y., et al., *Fast disintegrating quercetin-loaded drug delivery systems fabricated using coaxial electrospinning.* International journal of molecular sciences, 2013. **14**(11): p. 21647-21659.
200. Han, D. and A.J. Steckl, *Triaxial Electrospun Nanofiber Membranes for Controlled Dual Release of Functional Molecules.* ACS Applied Materials & Interfaces, 2013. **5**(16): p. 8241-8245.
201. Dumont, C.M., J. Park, and L.D. Shea, *Controlled release strategies for modulating immune responses to promote tissue regeneration.* J Control Release, 2015. **219**: p. 155-166.
202. Zelzer, M., et al., *Enzyme responsive materials: design strategies and future developments.* Biomaterials Science, 2013. **1**(1): p. 11-39.
203. Mickova, A., et al., *Core/shell nanofibers with embedded liposomes as a drug delivery system.* Biomacromolecules, 2012. **13**(4): p. 952-962.

204. Ma, W., et al., *Electrospun fibers for oil–water separation. RSC Adv., 6 (16), 12868–12884*. 2016.
205. Wang, X., et al., *Electrospun nanofibrous materials: a versatile medium for effective oil/water separation.* Materials today, 2016. **19**(7): p. 403-414.
206. Thavasi, V., G. Singh, and S. Ramakrishna, *Electrospun nanofibers in energy and environmental applications.* Energy & Environmental Science, 2008. **1**(2): p. 205-221.
207. Lin, J., et al., *Co-axial electrospun polystyrene/polyurethane fibres for oil collection from water surface.* Nanoscale, 2013. **5**(7): p. 2745-55.
208. Wen, H.-F., et al., *Electrospun zein nanoribbons for treatment of lead-contained wastewater.* Chemical Engineering Journal, 2016. **290**: p. 263-272.
209. Zou, H., et al., *Electrospun poly (2-aminothiazole)/cellulose acetate fiber membrane for removing Hg (II) from water.* Journal of Applied Polymer Science, 2017. **134**(21).
210. He, H., et al., *Thermoelectric–photoelectric composite nanocables induced a larger efficiency in dye-sensitized solar cells.* Journal of Materials Chemistry A, 2016. **4**(24): p. 9362-9369.
211. Rezaei, B., et al., *Fabrication of thermal intelligent core/shell nanofibers by the solution coaxial electrospinning process.* Advances in Polymer Technology, 2016. **35**(1).
212. Yang, Y., et al., *A shield ring enhanced equilateral hexagon distributed multi-needle electrospinning spinneret.* IEEE Transactions on Dielectrics and Electrical Insulation, 2010. **17**(5): p. 1592-1601.
213. Mohamed, H., *El-Newehy, Salem S. Al-Deyab, El-Refaie Kenawy, Ahmed Abdel-Megeed, Nanospider technology for the production of nylon-6 nanofibers for biomedical applications.* Journal of Nanomaterials, 2011. **15**.
214. Lu, W., et al., *The Preparation of Chitosan Oligosaccharide/Alginate Sodium/Gelatin Nanofibers by Spiral-Electrospinning.* J Nanosci Nanotechnol, 2016. **16**(3): p. 2360-4.
215. Lu, W., et al., *Gelatin nanofibers prepared by spiral-electrospinning and cross-linked by vapor and liquid-phase glutaraldehyde.* Materials Letters,

2015. **140**: p. 1-4.
216. Lim, C.T., *Nanofiber technology: current status and emerging developments.* Progress in Polymer Science, 2017. **70**: p. 1-17.
217. Bhardwaj, N. and S.C. Kundu, *Electrospinning: a fascinating fiber fabrication technique.* Biotechnol Adv, 2010. **28**(3): p. 325-47.
218. Tan, E.P., S.Y. Ng, and C.T. Lim, *Tensile testing of a single ultrafine polymeric fiber.* Biomaterials, 2005. **26**(13): p. 1453-6.
219. Sinha-Ray, S., A. Yarin, and B. Pourdeyhimi, *Meltblown fiber mats and their tensile strength.* Polymer, 2014. **55**(16): p. 4241-4247.
220. Yoon, J., et al., *Recent progress in coaxial electrospinning: New parameters, various structures, and wide applications.* Advanced Materials, 2018. **30**(42): p. 1704765.
221. Li, D., et al., *Nanofibers of conjugated polymers prepared by electrospinning with a two-capillary spinneret.* Advanced Materials, 2004. **16**(22): p. 2062-2066.
222. Kirecci, A., Ü. Özkoç, and H.İ. İçoğlu, *Determination of optimal production parameters for polyacrylonitrile nanofibers.* Journal of applied polymer science, 2012. **124**(6): p. 4961-4968.
223. Wang, X., et al., *Electrospun nanofibrous membranes for highly sensitive optical sensors.* Nano letters, 2002. **2**(11): p. 1273-1275.
224. Joshi, P., et al., *Electrospun carbon nanofibers as low-cost counter electrode for dye-sensitized solar cells.* ACS applied materials & interfaces, 2010. **2**(12): p. 3572-3577.
225. Venugopal, J. and S. Ramakrishna, *Applications of polymer nanofibers in biomedicine and biotechnology.* Appl Biochem Biotechnol, 2005. **125**(3): p. 147-58.
226. Huang, Z.-M., et al., *A review on polymer nanofibers by electrospinning and their applications in nanocomposites.* Composites science and technology, 2003. **63**(15): p. 2223-2253.
227. Zhang, L., et al., *A review: carbon nanofibers from electrospun polyacrylonitrile and their applications.* Journal of Materials Science, 2014. **49**(2): p. 463-480.
228. Babel, A., et al., *Electrospun nanofibers of blends of conjugated polymers:*

morphology, optical properties, and field-effect transistors. 2005. **38**(11): p. 4705-4711.

229. Cooley, J.F., *Apparatus for electrically dispersing fluids*. 1902, Google Patents.
230. Ramakrishna, S., *An introduction to electrospinning and nanofibers*. 2005: World Scientific.
231. Rohlfs, W., et al., *Two-phase electrohydrodynamic simulations using a volume-of-fluid approach: A comment.* Journal of Computational Physics, 2012. **231**(12): p. 4454-4463.
232. Yarin, A.L., S. Koombhongse, and D.H. Reneker, *Taylor cone and jetting from liquid droplets in electrospinning of nanofibers.* Journal of applied physics, 2001. **90**(9): p. 4836-4846.
233. Lauricella, M., et al., *Different regimes of the uniaxial elongation of electrically charged viscoelastic jets due to dissipative air drag.* Mechanics Research Communications, 2015. **69**: p. 97-102.
234. Deshawar, D. and P. Chokshi, *Stability analysis of an electrospinning jet of polymeric fluids.* Polymer, 2017. **131**: p. 34-49.
235. Zhou, Z., et al., *Needleless emulsion electrospinning for scalable fabrication of core–shell nanofibers.* Journal of Applied Polymer Science, 2014. **131**(20).
236. Xu, H., M. Yamamoto, and H. Yamane, *Melt electrospinning: Electrodynamics and spinnability.* Polymer, 2017. **132**: p. 206-215.
237. Yarin, A., W. Kataphinan, and D.H. Reneker, *Branching in electrospinning of nanofibers.* Journal of applied physics, 2005. **98**(6): p. 064501.
238. Lian, H. and Z. Meng, *Melt electrospinning vs. solution electrospinning: A comparative study of drug-loaded poly (ε-caprolactone) fibres.* Materials Science and Engineering: C, 2017. **74**: p. 117-123.
239. Wu, X.-F., Y. Salkovskiy, and Y.A. Dzenis, *Modeling of solvent evaporation from polymer jets in electrospinning.* Applied Physics Letters, 2011. **98**(22): p. 223108.
240. Zhou, H., T.B. Green, and Y.L. Joo, *The thermal effects on electrospinning of polylactic acid melts.* Polymer, 2006. **47**(21): p. 7497-7505.
241. Dalton, P.D., et al., *Patterned melt electrospun substrates for tissue*

engineering. Biomed Mater, 2008. **3**(3): p. 034109.

242. Kong, C., et al., *Effects of the spin line temperature profile and melt index of poly (propylene) on melt-electrospinning.* Polymer Engineering & Science, 2009. **49**(2): p. 391-396.

243. Persano, L., et al., *Industrial upscaling of electrospinning and applications of polymer nanofibers: a review.* Macromolecular Materials and Engineering, 2013. **298**(5): p. 504-520.

244. Rein, D., et al., *Application of gentle annular gas veil for electrospinning of polymer solutions and melts.* Polymer Engineering & Science, 2009. **49**(4): p. 774-782.

245. Zhmayev, E., D. Cho, and Y.L. Joo, *Nanofibers from gas-assisted polymer melt electrospinning.* Polymer, 2010. **51**(18): p. 4140-4144.

246. Drabek, J., M. Zatloukal, and M. Martyn, *Effect of molecular weight on secondary Newtonian plateau at high shear rates for linear isotactic melt blown polypropylenes.* Journal of Non-Newtonian Fluid Mechanics, 2018. **251**: p. 107-118.

247. Lee, B.-S., et al., *New electrospinning nozzle to reduce jet instability and its application to manufacture of multi-layered nanofibers.* Scientific reports, 2014. **4**: p. 6758.

248. Joulaian, M., et al., *A new algorithm for simulating flows of conducting fluids in the presence of electric fields.* Computer Physics Communications, 2012. **183**(11): p. 2405-2412.

249. Xie, S. and Y. Zeng, *Effects of electric field on multineedle electrospinning: experiment and simulation study.* Industrial & engineering chemistry research, 2012. **51**(14): p. 5336-5345.

250. Theron, S., et al., *Multiple jets in electrospinning: experiment and modeling.* Polymer, 2005. **46**(9): p. 2889-2899.

251. Yue, P., et al., *A diffuse-interface method for simulating two-phase flows of complex fluids.* Journal of Fluid Mechanics, 2004. **515**: p. 293-317.

252. Olsson, E. and G. Kreiss, *A conservative level set method for two phase flow.* Journal of computational physics, 2005. **210**(1): p. 225-246.

253. Zhmayev, E., D. Cho, and Y. Lak Joo, *Electrohydrodynamic quenching in polymer melt electrospinning.* Physics of fluids, 2011. **23**(7): p. 073102.

254. Kim, G., Y.-S. Cho, and W.D. Kim, *Stability analysis for multi-jets electrospinning process modified with a cylindrical electrode.* European polymer journal, 2006. **42**(9): p. 2031-2038.
255. Yang, Y., et al., *Effect of electric field distribution uniformity on electrospinning.* Journal of applied physics, 2008. **103**(10): p. 104307.
256. Jin, F.-L., X. Li, and S.-J. Park, *Synthesis and application of epoxy resins: A review.* Journal of Industrial and Engineering Chemistry, 2015. **29**: p. 1-11.
257. Sussman, M., et al., *An improved level set method for incompressible two-phase flows.* Computers & Fluids, 1998. **27**(5-6): p. 663-680.
258. Hysing, S., *Mixed element FEM level set method for numerical simulation of immiscible fluids.* Journal of Computational Physics, 2012. **231**(6): p. 2449-2465.
259. Godinho, M., et al., *Self-winding of helices in plant tendrils and cellulose liquid crystal fibers.* 2010. **6**(23): p. 5965-5970.
260. Shaevitz, J.W., J.Y. Lee, and D.A. Fletcher, *Spiroplasma Swim by a Processive Change in Body Helicity.* Cell, 2005. **122**(6): p. 941-945.
261. Mozziconacci, J. and C. Lavelle, *Chromatin Fiber: 30 years of models.* Computational biology: New research, 2009: p. 147-163.
262. Zhao, T., Y. Zheng, and Y. Zeng, *Design of a novel co-electrospinning system with flat spinneret for producing helical nanofibers.* 2019. **57**(22): p. 1496-1505.
263. Fleischer, S., et al., *Spring-like fibers for cardiac tissue engineering.* Biomaterials, 2013. **34**(34): p. 8599-8606.
264. Wu, H., Y. Zheng, and Y. Zeng, *Fabrication of helical nanofibers via co-electrospinning.* Industrial & Engineering Chemistry Research, 2015. **54**(3): p. 987-993.
265. Silva, P., F.V. de Abreu, and M. Godinho, *Shaping helical electrospun filaments: a review.* Soft matter, 2017. **13**(38): p. 6678-6688.
266. Taylor, G., *Instability of jets, threads, and sheets of viscous fluid*, in *Applied mechanics*. 1969, Springer. p. 382-388.
267. Tchavdarov, B., A.L. Yarin, and S. Radev, *Buckling of thin liquid jets.* Journal of Fluid Mechanics, 1993. **253**: p. 593-615.
268. Jawed, M.K., et al., *Coiling of elastic rods on rigid substrates.* Proceedings

of the National Academy of Sciences, 2014. **111**(41): p. 14663-14668.

269. Han, T., D.H. Reneker, and A.L. Yarin, *Buckling of jets in electrospinning.* Polymer, 2007. **48**(20): p. 6064-6076.

270. Chang, G., et al., *Morphology control of nanohelix by electrospinning.* Applied Physics Letters, 2012. **101**(26): p. 263505.

271. Gu, B.K., et al., *Direct fabrication of twisted nanofibers by electrospinning.* Applied Physics Letters, 2007. **90**(26): p. 263902.

272. Chang, G. and J. Shen, *Fabrication of Microropes via Bi-electrospinning with a Rotating Needle Collector.* Macromolecular rapid communications, 2010. **31**(24): p. 2151-2154.

273. Zhang, X., J. Chen, and Y. Zeng, *Construction of helical nanofibers from cellulose acetate and a flexible component.* Cellulose, 2019. **26**(9): p. 5187-5199.

274. Wu, H., S. Zhao, and L. Han, *Fabrication of CA/TPU Helical Nanofibers and its Mechanism Analysis.* Nanoscale research letters, 2018. **13**(1): p. 104.

275. Liu, C.-X. and J.-W. Choi, *Improved dispersion of carbon nanotubes in polymers at high concentrations.* Nanomaterials, 2012. **2**(4): p. 329-347.

276. Liu, G., et al., *Electrospun starch nanofibers: Recent advances, challenges, and strategies for potential pharmaceutical applications.* Journal of Controlled Release, 2017. **252**: p. 95-107.

277. Reneker, D.H., et al., *Bending instability of electrically charged liquid jets of polymer solutions in electrospinning.* Journal of Applied physics, 2000. **87**(9): p. 4531-4547.

278. Yarin, A.L., S. Koombhongse, and D.H.J.J.o.a.p. Reneker, *Bending instability in electrospinning of nanofibers.* 2001. **89**(5): p. 3018-3026.

279. Thompson, C.J., et al., *Effects of parameters on nanofiber diameter determined from electrospinning model.* Polymer, 2007. **48**(23): p. 6913-6922.

280. Yu, D., et al., *A modified coaxial electrospinning for preparing fibers from a high concentration polymer solution.* Express Polymer Letters, 2011. **5**(8).

281. Collins, G., et al., *Charge generation, charge transport, and residual charge in the electrospinning of polymers: a review of issues and complications.* Journal of Applied Physics, 2012. **111**(4): p. 044701.

282. Hutmacher, D.W. and P.D. Dalton, *Melt electrospinning.* Chemistry–An Asian Journal, 2011. **6**(1): p. 44-56.
283. Golecki, H.M., et al., *Effect of solvent evaporation on fiber morphology in rotary jet spinning.* Langmuir, 2014. **30**(44): p. 13369-13374.
284. Tomar, G., et al., *Two-phase electrohydrodynamic simulations using a volume-of-fluid approach.* Journal of Computational Physics, 2007. **227**(2): p. 1267-1285.
285. Carroll, C.P. and Y.L. Joo, *Discretized modeling of electrically driven viscoelastic jets in the initial stage of electrospinning.* Journal of Applied Physics, 2011. **109**(9): p. 094315.
286. Atten, P., B. Malraison, and M. Zahn, *Electrohydrodynamic plumes in point-plane geometry.* IEEE transactions on dielectrics and electrical insulation, 1997. **4**(6): p. 710-718.
287. Feng, J., *The stretching of an electrified non-Newtonian jet: A model for electrospinning.* Physics of fluids, 2002. **14**(11): p. 3912-3926.
288. Ershov, B., et al., *Silver atoms and clusters in aqueous solution: absorption spectra and the particle growth in the absence of stabilizing Ag+ ions.* The Journal of Physical Chemistry, 1993. **97**(18): p. 4589-4594.
289. Eisa, W.H., et al., *In situ approach induced growth of highly monodispersed Ag nanoparticles within free standing PVA/PVP films.* Spectrochimica Acta Part A: Molecular and Biomolecular Spectroscopy, 2012. **95**: p. 341-346.
290. Zhou, H., T.B. Green, and Y.L.J.P. Joo, *The thermal effects on electrospinning of polylactic acid melts.* 2006. **47**(21): p. 7497-7505.
291. Carroll, C.P. and Y.L. Joo, *Axisymmetric instabilities of electrically driven viscoelastic jets.* Journal of Non-Newtonian Fluid Mechanics, 2008. **153**(2): p. 130-148.
292. Yu, D.G., et al., *Improving Polymer Nanofiber Quality Using a Modified Co-axial Electrospinning Process.* Macromolecular Rapid Communications, 2011. **32**(9-10): p. 744-750.
293. Huang, S., et al., *Flexible electronics: stretchable electrodes and their future.* Advanced Functional Materials, 2019. **29**(6): p. 1805924.
294. Chu, B., et al., *Bring on the bodyNET.* Nature, 2017. **549**(7672): p. 328-330.

295. Bao, Z. and X. Chen, *Flexible and stretchable devices.* Advanced Materials, 2016. **28**(22): p. 4177-4179.
296. Kang, S.-K., et al., *Advanced materials and devices for bioresorbable electronics.* Accounts of chemical research, 2018. **51**(5): p. 988-998.
297. Hammock, M.L., et al., *25th anniversary article: the evolution of electronic skin (e-skin): a brief history, design considerations, and recent progress.* Advanced materials, 2013. **25**(42): p. 5997-6038.
298. Besse, N., et al., *Flexible active skin: large reconfigurable arrays of individually addressed shape memory polymer actuators.* Advanced Materials Technologies, 2017. **2**(10): p. 1700102.
299. Lin, S., et al., *Roll-to-Roll Production of Transparent Silver-Nanofiber-Network Electrodes for Flexible Electrochromic Smart Windows.* Advanced Materials, 2017. **29**(41): p. 1703238.
300. Shengbo, S., et al., *Highly sensitive wearable strain sensor based on silver nanowires and nanoparticles.* Nanotechnology, 2018. **29**(25): p. 255202.
301. Jun, K., J. Kim, and I.K. Oh, *An electroactive and transparent haptic interface utilizing soft elastomer actuators with silver nanowire electrodes.* Small, 2018. **14**(35): p. 1801603.
302. Lin, S., et al., *Roll-to-Roll Production of Transparent Silver-Nanofiber-Network Electrodes for Flexible Electrochromic Smart Windows.* Adv Mater, 2017. **29**(41): p. 1703238.
303. Wu, H., et al., *A transparent electrode based on a metal nanotrough network.* Nature nanotechnology, 2013. **8**(6): p. 421.
304. Lee, J.-Y., et al., *Solution-processed metal nanowire mesh transparent electrodes.* Nano letters, 2008. **8**(2): p. 689-692.
305. Akter, T. and W.S. Kim, *Reversibly stretchable transparent conductive coatings of spray-deposited silver nanowires.* ACS applied materials & interfaces, 2012. **4**(4): p. 1855-1859.
306. Choi, D.Y., et al., *Annealing-free, flexible silver nanowire–polymer composite electrodes via a continuous two-step spray-coating method.* Nanoscale, 2013. **5**(3): p. 977-983.
307. Nam, S., et al., *Ultrasmooth, extremely deformable and shape recoverable Ag nanowire embedded transparent electrode.* Scientific reports, 2014.

4(1): p. 1-7.

308. Kang, S., et al., *Capillary printing of highly aligned silver nanowire transparent electrodes for high-performance optoelectronic devices.* Nano letters, 2015. **15**(12): p. 7933-7942.
309. Lu, H., et al., *Locally welded silver nano-network transparent electrodes with high operational stability by a simple alcohol-based chemical approach.* Advanced Functional Materials, 2015. **25**(27): p. 4211-4218.
310. Ok, K.-H., et al., *Ultra-thin and smooth transparent electrode for flexible and leakage-free organic light-emitting diodes.* Scientific reports, 2015. **5**: p. 9464.
311. Han, D., et al., *A facile method to prepare transparent and stretchable epidermal thin film heaters.* Composites Science and Technology, 2018. **168**: p. 460-466.
312. Kang, S., et al., *Capillary Printing of Highly Aligned Silver Nanowire Transparent Electrodes for High-Performance Optoelectronic Devices.* Nano Lett, 2015. **15**(12): p. 7933-42.
313. Garnett, E.C., et al., *Self-limited plasmonic welding of silver nanowire junctions.* Nature materials, 2012. **11**(3): p. 241-249.
314. Bellew, A.T., et al., *Resistance of single Ag nanowire junctions and their role in the conductivity of nanowire networks.* ACS nano, 2015. **9**(11): p. 11422-11429.
315. Jagota, M. and N. Tansu, *Conductivity of nanowire arrays under random and ordered orientation configurations.* Scientific reports, 2015. **5**: p. 10219.
316. Liu, Y., et al., *Capillary-force-induced cold welding in silver-nanowire-based flexible transparent electrodes.* Nano letters, 2017. **17**(2): p. 1090-1096.
317. He, S., et al., *Conductivity of two-dimensional disordered nanowire networks: Dependence on length-ratio of conducting paths to all nanowires.* Journal of Applied Physics, 2018. **124**(5): p. 054302.
318. Nirmalraj, P.N., et al., *Manipulating connectivity and electrical conductivity in metallic nanowire networks.* Nano letters, 2012. **12**(11): p. 5966-5971.
319. Lee, J., et al., *Very long Ag nanowire synthesis and its application in a*

highly transparent, conductive and flexible metal electrode touch panel. Nanoscale, 2012. **4**(20): p. 6408-6414.

320. Jang, J., et al., *Rapid production of large-area, transparent and stretchable electrodes using metal nanofibers as wirelessly operated wearable heaters.* NPG Asia Materials, 2017. **9**(9): p. e432-e432.
321. Akter, T. and W.S. Kim, *Reversibly stretchable transparent conductive coatings of spray-deposited silver nanowires.* ACS Appl Mater Interfaces, 2012. **4**(4): p. 1855-9.
322. Guo, C.F., et al., *Enhancing the scratch resistance by introducing chemical bonding in highly stretchable and transparent electrodes.* Nano letters, 2016. **16**(1): p. 594-600.
323. Huang, S., et al., *A Highly Stretchable and Fatigue-Free Transparent Electrode Based on an In-Plane Buckled Au Nanotrough Network.* Advanced Electronic Materials, 2017. **3**(3): p. 1600534.
324. Lee, C.-J., et al., *Crack-induced Ag nanowire networks for transparent, stretchable, and highly sensitive strain sensors.* Scientific reports, 2017. **7**(1): p. 1-8.
325. Nam, S., et al., *Ultrasmooth, extremely deformable and shape recoverable Ag nanowire embedded transparent electrode.* Sci Rep, 2014. **4**(1): p. 4788.
326. Lee, C.J., et al., *Crack-induced Ag nanowire networks for transparent, stretchable, and highly sensitive strain sensors.* Sci Rep, 2017. **7**(1): p. 7959.
327. Guo, C.F., et al., *Enhancing the Scratch Resistance by Introducing Chemical Bonding in Highly Stretchable and Transparent Electrodes.* Nano Lett, 2016. **16**(1): p. 594-600.
328. Johnston, I., et al., *Mechanical characterization of bulk Sylgard 184 for microfluidics and microengineering.* Journal of Micromechanics and Microengineering, 2014. **24**(3): p. 035017.
329. Lendlein, A. and S. Kelch, *Shape-memory polymers.* Angewandte Chemie International Edition, 2002. **41**(12): p. 2034-2057.
330. Hong, S.B., et al., *Optical and shape memory properties of semicrystalline poly (cyclooctene) upon cold-drawing.* Journal of Polymer Science Part B: Polymer Physics, 2017. **55**(21): p. 1595-1607.
331. Liu, C., et al., *Chemically cross-linked polycyclooctene: synthesis,*

characterization, and shape memory behavior. Macromolecules, 2002. **35**(27): p. 9868-9874.

332. Rosa, R.M., et al., *Simultaneous photo-induced cross-linking and silver nanoparticle formation in a PVP electrospun wound dressing.* Materials Letters, 2017. **207**: p. 145-148.
333. Rosu, D., L. Rosu, and C.N. Cascaval, *IR-change and yellowing of polyurethane as a result of UV irradiation.* Polymer Degradation and Stability, 2009. **94**(4): p. 591-596.
334. Mutiso, R.M., et al., *Integrating simulations and experiments to predict sheet resistance and optical transmittance in nanowire films for transparent conductors.* ACS nano, 2013. **7**(9): p. 7654-7663.
335. Sarkar, B., D.K. Satapathy, and M. Jaiswal, *Wrinkle and crack-dependent charge transport in a uniaxially strained conducting polymer film on a flexible substrate.* Soft Matter, 2017. **13**(32): p. 5437-5444.
336. Hu, Q., et al., *Manufacturing and 3D printing of continuous carbon fiber prepreg filament.* Journal of materials science, 2018. **53**(3): p. 1887-1898.
337. Ryu, S.Y., et al., *Lateral buckling mechanics in silicon nanowires on elastomeric substrates.* Nano letters, 2009. **9**(9): p. 3214-3219.
338. Bradshaw, R., F. Fisher, and L.C. Brinson, *Fiber waviness in nanotube-reinforced polymer composites—II: modeling via numerical approximation of the dilute strain concentration tensor.* Composites Science and Technology, 2003. **63**(11): p. 1705-1722.
339. Ryu, S.Y., et al., *Lateral buckling mechanics in silicon nanowires on elastomeric substrates.* Nano Lett, 2009. **9**(9): p. 3214-9.
340. Zhu, F., C. Park, and G. Jin Yun, *An extended Mori-Tanaka micromechanics model for wavy CNT nanocomposites with interface damage.* Mechanics of Advanced Materials and Structures, 2019: p. 1-13.
341. Lacour, S.P., et al., *Mechanisms of reversible stretchability of thin metal films on elastomeric substrates.* Applied Physics Letters, 2006. **88**(20): p. 204103.

Korean abstract

본 연구의 목적은 전기방사 공정에서의 새로운 공정 변수들을 이용하여 은나노섬유를 제작하고 이를 활용하여 투명·신축 전극을 제작하는 것이다. 이를 위한 일련의 연구들이 다음의 순서로 진행되었다.

Gas-assisted 용융 전기방사 공정에 대한 multi-physics 모델링을 개발하였으며 이를 통하여 공정 변수들의 역할을 파악하였다. 단일 노즐을 이용한 공정에서 젯의 표면에 인가되는 응력을 수치해석을 통하여 분석함으로써 젯의 인장에 있어 점성 전단 응력이 주요하게 작용함을 밝혀냈다. 젯은 점성 전단 응력이 특정 값에 도달하였을 때에 안정적으로 형성되었으며, 젯의 인장률 또한 급격히 증가하였다. 이때의 응력을 안정적인 방사성을 판단하는 임계 점성 전단 응력이라 정의하였다. 단일 노즐 공정뿐만 아니라 멀티 노즐 공정을 모델링하였으며 이로부터 안정적인 방사성을 판단할 수 있는 방사성 다이어그램을 제시하였다.

다음으로는 섬유의 구조를 헬리컬 구조로 제작하는 공정을 디자인하였다. 우선, 젯의 초기 곡률과 젯의 위치에 따른 고화가 섬유의 구조에 미치는 영향을 조사하였다. 전기 방사된 섬유의 구조는 용매의 증기압이 증가함에 따라 발생하는 빠른 고화로 인하여 직선형태에서 헬리컬 구조로 변화하였다. 이는 금속 이온이 과량으로 첨가된 전도성 용액에 대해서도 유사한 결과를 보였다. 이에 대한 시뮬레이션 결과는 전하 밀도의 증가가 강한 전기장을 발생시켰으며, 이로 인하여 젯의 급격한 인장 및 고화가 발생하였음을 보여주며, 그러한 이유로 헬리컬

구조가 형성되었음 나타냈다. 이를 이용하여 헬리컬 구조의 섬유가 형성되는 메커니즘을 제시하였다.

마지막으로 전기방사를 이용해 제작한 은나노섬유를 이용하여 투명·신축 전극을 제작하였다. 전극은 형상기억 고분자인 crosslinked polycyclooctene 을 기판으로 활용하였다. 제작한 전극은 잔류 변형이 없고 투명도를 제어할 수 있는 특성을 보였다. 큰 인장에도 잔류 변형을 보이지 않는 형상기억고분자 기판의 특성으로 인해 면내 굽힘 구조의 은나노섬유가 효율적으로 제작되었다. 이러한 특성으로 제작한 전극은 3,000 회의 굽힘 평가와 900 회의 인장평가에도 전도성을 유지할 수 있었다. 또한 제작한 전극은 전기적 자극을 통하여 온도, 투명도, 강성 및 형상기억 특성을 제어할 수 있다는 특징을 보였다. 제작한 전극을 활용하여 광학적 그리고 기계적 특성을 제어할 수 있는 새로운 형태의 스마트 전극을 시연 하였다.

핵심어: 전기방사공정, 전산모사, 공정변수, 은나노섬유, 투명·신축 전극

학번: 2014-22539

감사의 글

학위 논문을 마무리 하기까지 6년이라는 시간을 보내며 주변에 계신 많은 분들께 도움을 받았습니다. 연구와 관련한 도움만이 아니라 생활과 삶에 대해 조언을 해주신 분들, 그리고 옆에서 부대끼며 행동과 생각을 배울 수 있게 해주신 많은 분들께 감사함을 느낍니다. 논문을 마무리 하는 마지막 과정으로써 그 분들께 조금이나마 감사의 마음을 전달 할 수 있게 되어 기쁩니다.

어린 시절부터 지금까지 언제나 저를 믿어 주시며, 무엇을 하던 간에 아무런 질문이나 나무람 없이 저의 선택을 지지해 주시는 부모님께 감사드립니다. 두 분은 세상에서 가장 존경하는 분들입니다. 부모님의 사랑 덕에 비단 대학원 생활뿐만 아니라 살아왔던 모든 순간들에 마음이 힘들거나 지친 적이 없었습니다. 학위를 마무리 짓는 일은 보람차기는 하나 제 삶에 있는 많은 경유지 중 하나라고 생각합니다. 다만, 이 과정을 핑계로 감사의 인사를 쑥스럽지 않게 드릴 수 있게 되어 기쁩니다. 그리고 바쁘다는 이유로 많은 시간을 같이 보내지 못한 누나들과 매형 그리고 윤성이, 우리 사랑하는 가족분들께도 언제나 마음을 따듯하게 해주셔서 감사하다고 말씀드리고 싶습니다.

그간 저의 연구와 생활을 지도해주신 유웅열 교수님께 감사드립니다. 연구실에 들어오게 된 첫날부터 많은 신경을 써 주셨던 것 항상 기억하고 있습니다. 여느 대학원생들이 지도교수님께 느낄 감사와 더불어 특별하게 감사드리고 싶은 것은 저를 믿어주시고 격려 해주신 일들입니다. 교수님께서는 부족한 저의 의견이나 생각도 귀담아 들어 주셨고 대화의 자리를 많이 만들어 주셨습니다. 학생들과의 관계를 단순한 스승과 제자의 관계가 아니라 동등한 연구자로서 함께 일을 할 수 있는 관계가 되길 기대하신다는 말씀은 제가 스스로를 특별하게 여길 수 있는 마음을 갖게

했고, 발전하고자 하는 태도를 갖게 하는 큰 동기부여가 되었습니다. 학술적으로나 인격적으로나 존경하는 교수님께 감사드립니다. 그리고 바쁘신 중에도 졸업심사를 해주신 안철희 교수님, 이명규 교수님, 조대환 상무님, 그리고 이병선 교수님께 감사의 인사를 드리고 싶습니다.

6년간 함께 연구실 생활을 해왔던 선후배 분들과 졸업한 동기 재호형님께도 감사 인사 드리고 싶습니다. 서로가 서로를 대하는 모습들이나 연구에 임하는 자세 그리고 각자의 책임감과 성실성을 보고 배울 수 있어 고마웠습니다. 그리고 남아 있는 저의 동기와 후배분들께도 감사드리며 논문을 전달하며 따로 인사 드리겠습니다.

연구실 밖에서도 도움주신 분들께 감사드립니다. 실험을 할 수 있는 환경을 제공해 주시고 귀중한 조언 해주신 육지호 교수님, 과제를 진행하며 많은 조언과 가르침 주시는 교수님들께도 감사드립니다. 특히 선정윤 교수님과 김욱성 교수님께서 해주신 많은 조언들이 연구를 진행하는 데에 큰 도움이 되었습니다. 그리고 실험에 필요한 장비들을 훌륭하게 제작해 주시는 영진정밀 사장님께도 감사드립니다.

얼굴은 자주 못보더라도 저를 응원해준 친구들 덕분에 힘낼 수 있어 고맙다 전하고 싶습니다. 특히 오랜 시간 함께 해준 형제 같은 친구들인 민이 진우에게 감사드립니다. 바쁘거나 힘들어도 항상 이해해 주고 응원해준 덕에 즐겁게 지낼 수 있었습니다.

이외에도 작은 지면에 미쳐 인사 드리지 못한 많은 분들께도 감사드립니다.

2020년 7월

윤지현